UNIVERSIDADE DE LISBOA
FACULDADE DE CIÊNCIAS
DEPARTAMENTO DE FÍSICA

On the hunt for Post-Starburst galaxies

Carlota Maria Pinto da Luz

Mestrado em Física
Especialização em Astrofísica e Cosmologia

Dissertação orientada por:
Doutor Ciro Pappalardo e Doutor Israel Matute

2024

Acknowledgments

Firstly, I would like to thank my supervisor, Doctor Ciro Pappalardo, and co-supervisor, Doctor Israel Matute, for the guidance on my first scientific research project and the patience for the countless hours of meetings.

To Ana, Bia and Diogo for all the laughs and memories during this period and for always being supportive in all my decisions. I wouldn't be able to achieve this without them.

To Inês, Alex, Henrique, Gabriel and Daniel for the lunches at Cantina Velha and the unforgettable support in these two years. A special thanks to Inês for hearing my struggles and being present whenever I most needed.

To Lara for all the support, care and trust and for sharing the struggles during the thesis.

To Arren and to Sheeb for making me laugh, distract me during stressful days and putting up with me every single day. For an amazing friendship that I will forever cherish.

Lastly, to my parents and my sister for believing in me and in my dreams and for supporting me throughout the whole process, providing me with all I needed.

Abstract

We investigate in detail the various evolutionary phases of galaxies — active star-forming, quiescent, and green valley. We specifically focus on post-starburst (PSB) systems, which are galaxies that, according to Maltby et al. [2018], "have experienced a recent burst of star formation followed by a rapid quenching on the timescale of tens of Myrs".

We base our work on a sample with 248,307 sources at $0.5 < z < 3.5$ from the COSMOS2020 dataset where we use UVJ color-color diagrams (divided into 0.5 redshift bins and then into 1 Gyr bins) to analyze and classify the galaxies into star-forming, quiescent and green valley galaxies, observing the dichotomy between them. We find that the sample is predominantly composed of star-forming galaxies ($\sim 92\%$).

With `CIGALE` simulations, we reproduce the COSMOS data and analyze a sample representative of passive galaxies with $12,084$ sources with the simulator. We classify PSB as galaxies that have a quenching timescale lower than 0.7 Gyr. Our results indicate that while the absolute number of passive galaxies decreases with redshift, the percentage of PSB systems increases, reaching $\sim 31\%$ at $z \sim 2.5$ and $\sim 2\%$ at $z \sim 1.0$, which aligns with previous studies. We conclude that models with just star formation history (without AGNs or mergers) can predict a small fraction of PSB galaxies, $\sim 3\%$. Lastly, we also find evidence that the speed of transition from star-forming to passive galaxies depends on redshift: a slow quenching at lower redshifts and a fast quenching at higher redshifts, increasing in stellar mass. After the peak of star formation and quiescence, quenching mechanisms tend to become more secular, leading to slower quenching timescales and a lower fraction of PSB galaxies. Before the peak, quenching mechanisms are dominated by faster processes, resulting in shorter timescales and a higher fraction of PSB systems.

Keywords: Galaxies Evolution, Post-Starburst, Passive Galaxies, Star Formation, Spectral Energy Distribution Fitting

Resumo

Observações demonstram que as galáxias têm sofrido mudanças drásticas ao longo de milhares de milhões de anos, deste modo, a formação e evolução destas tem sido um tópico recorrente entre investigadores da área da astronomia. De uma forma simples, galáxias são sistemas dinâmicos e gravitacionalmente ligados de estrelas, gás, poeira e matéria escura.

A formação estelar desempenha um papel fundamental na evolução das galáxias ao longo da história do universo. Esta influencia não só a luminosidade e a aparência das galáxias, como também afeta a sua composição química e estrutura a longo prazo. Consequentemente, no contexto da evolução de galáxias, é importante categorizá-las com base na sua taxa de formação estelar à qual pode variar desde sistemas passivos com pouca ou nenhuma formação estelar, até galáxias com formação estelar ativa.

Um dos parâmetros que ajuda a classificar galáxias de acordo com a sua idade e a sua atividade de formação estelar é a cor. No contexto da astrofísica, cor é a diferença de magnitude entre dois filtros e as magnitudes são uma medida do brilho ou luminosidade de um objeto celestial. Deste modo, magnitudes mais elevadas correspondem a objetos mais fracos e magnitudes mais baixas correspondem a objetos mais brilhantes.

As galáxias passivas, que cessaram a sua formação estelar há muito tempo, são dominadas por estrelas mais velhas e mais frias, como as gigantes vermelhas e as estrelas de baixa massa. Estas estrelas emitem pouca radiação azul e ultravioleta, conferindo às galáxias passivas a sua característica cor vermelha. Assim, o vermelho surge da ausência de estrelas azuis jovens e quentes que são normalmente encontradas em regiões de formação estelar ativa.

Em contraste, as galáxias com formação estelar continuam a produzir novas estrelas de uma forma contínua, embora muitas vezes reduzida, impulsionada por um fornecimento constante de gás. Estas galáxias tendem a exibir uma cor azulada devido à formação contínua de estrelas jovens e massivas que são excecionalmente brilhantes e emitem quantidades significativas de radiação azul e radiação ultravioleta. Embora a vida útil destas estrelas seja relativamente curta, a sua intensa luminosidade domina a luz vermelha das estrelas mais velhas. À medida que a taxa de formação estelar diminui ao longo do tempo, as galáxias mudam gradualmente para cores mais vermelhas — a população de estrelas azuis e massivas diminui e a luz das estrelas mais antigas e mais vermelhas começa a dominar.

As galáxias em formação estelar ativa fazem a transição para galáxias passivas quando esgotam o seu combustível para formar estrelas ou se a sua formação estelar é subitamente suprimida. As galáxias que se encontram neste período temporário designam-se de galáxias “green valley”. Este estado refere-se a uma fase de transição entre as duas principais populações de galáxias: as galáxias azuis, formadoras de estrelas, e as galáxias vermelhas, passivas. As galáxias no ”green valley” são um tema de investigação muito interessante, pois fornecem informações sobre os mecanismos que conduzem à cessação da formação estelar, um processo conhecido como “quenching” ou atenuação.

Observações sugerem que as taxas de formação estelar aumentaram de forma constante durante as primeiras épocas do universo, pelo menos até ao ponto em que as observações são atualmente possíveis. Isto implica que as galáxias durante épocas anteriores experimentaram fases vigorosas de formação estelar. No entanto, ao longo dos últimos milhares de milhões de anos, o gás disponível para a formação estelar tem vindo a tornar-se cada vez mais limitado. Perto de $z \sim 2$, o universo atingiu o pico da atividade de formação estelar, após o qual entrou num declínio lento, acabando por atingir os níveis baixos observados hoje (Madau and Dickinson [2014]).

Embora se consigam prever os fatores que causam este declínio na formação estelar, a escala de tempo precisa deste processo permanece incerta. O declínio poderá resultar de um processo secular, que levará vários milhares de milhões de anos, ou, alternativamente, pode envolver um mecanismo abrupto seguido pela evolução passiva da última geração de estrelas. Neste último cenário, as galáxias poderão entrar numa fase "post-starburst" (PSB), caracterizada pela coexistência de populações estelares antigas e jovens, isto é, galáxias caracterizadas por um resíduo de formação estelar entre populações antigas.

Para determinar qual o processo que caracteriza a atenuação de uma galáxia, é essencial estudar sistemas que foram recentemente atenuados na sua formação estelar, e os PSB fornecem um exemplo importante. De acordo com Maltby et al. [2018], os PSB são caracterizados como sistemas em que uma grande explosão de formação estelar foi rapidamente atenuada nas últimas centenas de milhões de anos. Portanto, as galáxias PSB são subprodutos de atenuação rápida.

Ao longo desta tese, investigou-se em detalhe as várias fases evolutivas das galáxias — formação estelar ativa, passiva e "green valley", focando-se particularmente nos sistemas PSB. Esta baseou-se no mais recente catálogo do levantamento COSMOS, COSMOS2020 (Weaver et al. [2022b]). O catálogo foi limpo cuidadosamente, removendo valores discrepantes e aplicando análises χ^2 para garantir a fiabilidade da amostra. Este processo resultou num conjunto de dados composto por 248,307 objetos dentro de $0.5 < z < 3.5$, com um limite de magnitude da banda H de 27, um sinal-ruído superior a 3 o que deu uma completude de massa acima dos 75%.

Usando diagramas cor-cor com filtros UVJ divididos em sub-diagramas de intervalos de $z = 0.5$ e baseando-se no estudo feito por Williams et al. [2009] conseguiu-se definir três regiões: a região passiva para as galáxias vermelhas que cessaram a formação estelar, outra para galáxias com formação estelar contínua e uma região ambígua, com uma espessura definida pelos erros fotométricos das cores $U - V$ e $V - J$. Esta última região contém uma mistura de galáxias passiva, em formação estelar ativa e na fase de transição.

Verificou-se uma dicotomia entre as diferentes galáxias da amostra nos vários gráficos UVJ, a qual é predominantemente composta por galáxias com formação estelar ativa, $\sim 92\%$, com $\sim 5\%$ de galáxias passivas e com $\sim 5\%$ de galáxias "ambíguas". Como o desvio para o vermelho não é uma medida linear do tempo devido à expansão do universo, repetiu-se esta análise dividindo a amostra em intervalos de 1 Gyr de $0.5 < z < 2.64$. Esta abordagem complementar revelou um aumento mais gradual da fração de galáxias dentro da região passiva ao longo do tempo.

Exploram-se também outros intervalos — 1.5, 0.5, 0.4, 0.3, 0.2 e 0.1 Gyrs — para investigar o comportamento do desvio padrão do número de galáxias nas três regiões. A análise mostrou que o intervalo de 1.0 Gyr teve o menor desvio padrão, enquanto o intervalo de 0.1 Gyr teve o máximo. No entanto, esta análise não foi suficience para determinar a escala de tempo típica para as transições das galáxias ou para obter conhecimentos mais profundos sobre os sistemas PSB.

Reproduziram-se e analisaram-se sintéticamente os dados da amostra do COSMOS usando o código `CIGALE` na sua capacidade de simulador (Boquien et al. [2019]; Burgarella et al. [2005]; Noll et al. [2009]). Focou-se em obter uma amostra representativa das galáxias passivas, definidas como a parte

mais densa da região passiva no diagrama UVJ da amostra do COSMOS. Este subconjunto incluiu 12,084 objectos, representando aproximadamente 74% das galáxias passivas e cerca de 5% da amostra total do COSMOS, com uma idade média de 5.82 Gyrs (observado a $z = 0.98$). Utilizando esta região, selecionaram-se objectos da amostra sintética do `CIGALE` com base nas idades das galáxias. Embora vários objetos sintéticos tivessem a mesma idade, estes provinham de diferentes combinações de parâmetros. Deste modo, selecionou-se uma combinação aleatória por correspondência, produzindo uma "amostra principal" sintética de 12,084 objetos que refletiam a distribuição passiva do COSMOS.

Da mesma forma, dividiu-se a amostra principal em intervalos de $z = 0.5$ e de 1 Gyr. Com base em estudos anteriores, classificaram-se as PSB como galáxias que tinham uma escala de tempo para a atenuação da formação estelar inferior a 0.7 Gyr, de acordo com a literatura (e.g. Wild et al. [2009], Poggianti et al. [2009], Belli et al. [2019], Wild et al. [2020]). Os resultados indicaram que enquanto o número absoluto de galáxias passivas diminuia com o desvio para o vermelho, a percentagem de sistemas PSB aumenta, atingindo $\sim 31\%$ a $z \sim 2.5$ e $\sim 2\%$ a $z \sim 1.0$. Estes resultados concordam com os de Belli et al. [2019]. Além disso, observou-se que a mediana e o desvio padrão das escalas de tempo da atenuação da formação estelar diminuem com o desvio para o vermelho, indicando que as galáxias atenuam mais rapidamente a desvios para o vermelho mais elevados — uma tendência consistente com o aumento da fracção de galáxias PSB e um ténue aumento da massa estelar.

Concluiu-se que os modelos simples escolhidos conseguem prever uma pequena fracção de galáxias PSB, 2.82% da amostra principal. Por último, notou-se também que a velocidade de transição da fase de galáxias de formação estelar para galáxias passivas depende do desvio para o vermelho: uma atenuação rápida a desvios mais elevados e uma atenuação lenta a desvios mais baixos.

Palavras Chave: Evolução de Galáxias, Formação Estelar, "Post-Starburst", Galáxias Passivas, Códigos de Síntese Espetral

Contents

List of Figures

List of Tables

Nomenclature

Abbreviations

ACS	Advanced Camera for Surveys
AGN	Active Galactic Nuclei
AMG	Ambiguous Galaxies
BPT	Baldwin-Philips-Tenlevich
CIGALE	Code Investigating GALaxy Emission
CGS	Centimeter–Gram–Second system of units
COSMOS	Cosmic Evolution Survey
ESA	European Space Agency
FIR	Far-Infrared
FUV	Far-Ultraviolet
Gyr	Gigayear
HCS	Hyper Suprime-Cam
HST	Hubble Space Telescope
IGM	Intergalactic Medium
IMF	Initial Mass Function
IR	Infrared
ISM	Interstellar Medium
Jy	Jansky
LIR	Infrared Luminosity
LwAge	Light-weighted Age
MIR	Mid-Infrared
MLv	Mass-to-light ratio in the V-band
Mpc	Megaparsec
Myr	Megayear
NIR	Near-Infrared
Pan-STARRS	Panoramic Survey Telescope and Rapid Response System
PCA	Principal Component Analysis
PSB	Post-Starburst
QS	Quiescent
QSG	Quiescent Galaxies

SDSS	Sloan Digital Sky Survey
SED	Spectral Energy Distribution
SF	Star Forming
SFG	Star-Forming Galaxies
SFH	Star Formation History
SFR	Star Formation Rate
sSFR	Specific Star Formation Rate
SMBH	Supermassive Black Hole
SN	Supernovae
SNR	Signal-to-noise Ratio
SSP	Simple Stellar Population
STD	Standard Deviation
UV	Ultraviolet
WFC	Wide Field Channel

Symbols

χ^2	Chi-square
χ^2_{red}	Reduced chi-square
A_V	Extinction in the V-band
M_*	Stellar mass
$\text{M}_\odot$	Mass of the sun
$\text{M}_\odot\ \text{yr}^{-1}$	Solar mass per year
$\text{M}_\odot/\text{L}_\odot$	Solar mass per solar luminosity
z	Redshift
λ	Wavelength
F_λ	Flux per wavelength
F_ν	Flux per frequency
f_λ	Flux per wavelength through a transmission filter
f_ν	Flux density
T	Transmission filter
τ	peak of star-formation in Myr

Chapter 1

Introduction

When we look at the vast night sky we can see many astronomical objects such as planets, stars, and even galaxies. The formation and evolution of galaxies have always been a recurring topic of research among astronomers. But what exactly is a galaxy, and why are these structures so crucial to our understanding of the universe?

In simple terms, a galaxy is a dynamic, gravitationally bound system composed of stars, gas, dust, and dark matter (Mo et al. [2010]). Our solar system, including Earth —the planet we call home—, is located within a galaxy known as the Milky Way. The Milky Way itself is part of an assemblage of galaxies called the Local Galactic Group or just the Local Group (see Figure 1.1) and is the second largest astronomical object of the group right after the Andromeda Galaxy (M31). The group has over 50 galaxies and spans a region of approximately 3 Mpc (Redd [2018]). The Local Group is situated within the Virgo Supercluster, which is, in turn, part of the even more massive Laniakea Supercluster —a structure that encompasses numerous galaxy clusters and groups spanning over 160 Mpc (Tully et al. [2014]).

The universe extends far beyond the Laniakea Supercluster, and as vast as it is, no two galaxies are identical. Galaxies vary in size, morphology, composition, mass, and even color —characteristics shaped by internal and external processes. However, when we observe an individual galaxy, we cannot know its exact state, for example, a million years ago —whether it looked the same or was entirely different. This is a challenge for astronomers, as the evolutionary timescales of galaxies far exceed the human lifespan, making it impossible to directly observe their transformation over time.

Despite this limitation, we can still study the galaxies when the universe was younger if we observe them at larger distances. Thanks to the finite speed of light, $c = 299,792,458$ m s^{-1} (Froome et al. [1971]), observing distant galaxies allows us to look back in time and examine the universe as it was billions of years ago. While this approach does not reveal the individual histories of nearby galaxies, it enables astronomers to statistically infer their past states as part of a population. Therefore, this makes galaxies prime candidates for studying and answering the enigmas of our universe, including its formation, evolution, and the processes that have shaped it into what we observe today

1.1 Galaxy Components

Galaxies can generally be simplified into three main components: the bulge (which may host a supermassive black hole), the disk, and the halo. However, not all galaxies possess all three components, as we will explore further in Section 1.2.

Bulges, spherical or ellipsoidal structures located at the center of a galaxy, are typically composed of older stars and contain little to no gas or dust, resulting in very low or absent star formation. Unlike

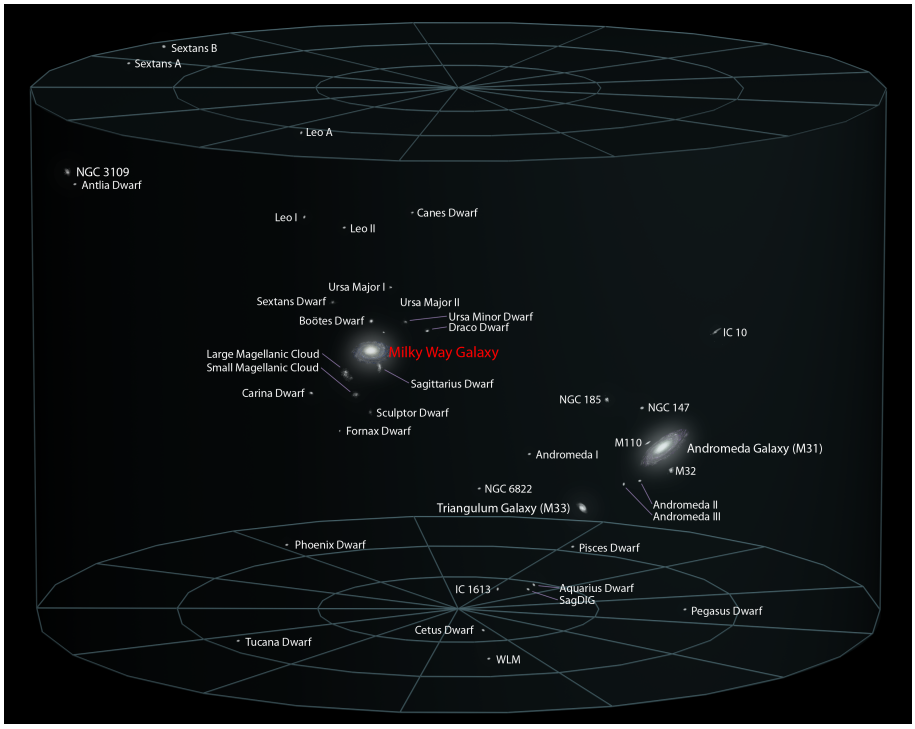

Figure 1.1: The Local Galactic Group illustration by Colvin [2018], showing the estimated size and locations of the different galaxies inside the group, including the Milky Way.

disks, which rely on rotation for stability, bulges maintain their equilibrium through velocity dispersion —random stellar motions in multiple directions. This behavior is analogous to the movement of molecules in a hot gas, where random motions generate pressure that counteracts gravity, keeping the bulge dynamically stable.

The shape of a bulge is often ellipsoidal, with varying degrees of flattening and oblateness. A perfectly spherical bulge has no flattening or oblateness, but when these characteristics are present, the bulge can appear elongated or flattened, resembling a squashed sphere (Murdin [2001]). The specific morphology of a bulge is determined by the degree of its flattening and oblateness, as well as the internal motions of its stars. While some bulges can be slightly flattened and may resemble small, thick disks, their stability and structure fundamentally differ from the rotational dynamics of galactic disks.

In many cases, the disk of a galaxy surrounds the central ellipsoidal bulge and consists of a mix of old and young stars, along with gas and dust. It is often a hub of active star formation, making it one of the most dynamic regions of the galaxy. The disk may feature spiral arms or rings, often containing well-defined HII regions—clouds of ionized hydrogen where new stars are born. This ongoing star formation imparts a generally bluer color to the disk compared to the bulge, which is dominated by older, redder stars. The stability of the disk is primarily maintained through its rotation, which generates a centrifugal force that counterbalances the inward pull of gravity (Murdin [2001]). This rotational motion not only ensures the equilibrium of the disk but also plays an important role in shaping distinct structures, such as the spiral arms.

At the center of the bulge lies the nucleus, a region containing a large concentration of mass within a relatively small volume, where not even light can escape from its gravitational pull (Bambi [2019]; Fraknoi et al. [2016]). This object is called a supermassive black hole and the term 'supermassive' comes from its extraordinary mass, which ranges from $\sim 10^5 - 10^{10}$ $M_\odot$, far exceeding the mass of typical stellar black holes, $\sim 3 - 100$ $M_\odot$ (Bambi [2019]). While stellar black holes form from the collapse of

massive stars, the origins of SMBHs remain an open area of research. One hypothesis suggests they may form through the merging of smaller black holes.

Statistical and observational evidence (Kormendy and Ho [2013]) indicates that SMBHs are present in nearly all large and intermediate-sized galaxies with prominent bulge components. These black holes may or may not be surrounded by an accretion disk—a swirling structure of hot gas and material spiraling into the black hole—which emits radiation detectable across a broad range of wavelengths, from infrared to X-rays. Furthermore, SMBHs play a crucial role in the dynamics of their host galaxies, contributing to the velocity dispersion of stars within a small fraction of the size of the bulge (Mo et al. [2010]).

Lastly, the galactic halo is an extended spheroidal component of galaxies that involves both the bulge and, when present, the disk. As we will refer to in Section 1.2, not all galaxies have disks; some consist solely of a bulge component. In such cases, distinguishing the halo becomes more challenging, as the transition between the bulge and the halo is less distinct compared to the more pronounced transition between the disk and the halo. Regardless of these variations, the galactic halo is primarily composed of gas, dust, stars, stellar clusters (referred to as the stellar halo), and dark matter (forming the dark matter halo; Maoz [2016]; Fraknoi et al. [2016]).

The stellar halo population consists of old stars and globular clusters. These clusters are dense systems of stars bound together by gravity, all formed from the same molecular cloud at approximately the same time. Globular clusters, along with the halo stars, tend to be old and relatively metal-poor. The stars in the halo are thought to have formed from hot, metal-enriched material ejected by supernova explosions, which later cooled and coalesced into these early stellar populations (Maoz [2016]).

It has been discovered that the total mass of galaxies extends far beyond their visible components, such as stars, gas, and dust (Maoz [2016]). This ”extra” mass is also responsible for bounding the galaxy components together, preventing the collapse of the galaxy. We now understand that this invisible mass is dark matter that does not emit, absorb, or reflect light and thus cannot be observed directly with telescopes. Instead, we can only detect it indirectly from its effects on the orbits of celestial objects (Fraknoi et al. [2016]). Consequently, the galactic halo is as extended as the dark matter halo.

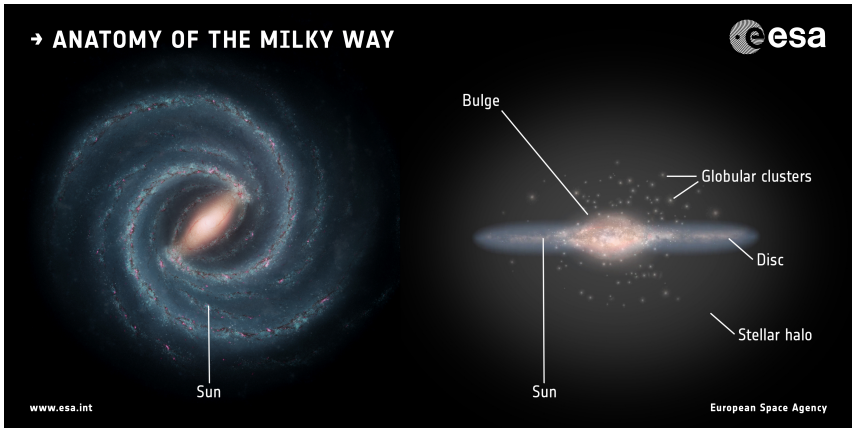

Figure 1.2: Artist impression of the Milky Way, face-on view on the left and edge-on view on the right side. Image credits left: NASA/JPL-Caltech; right: ESA; layout: ESA/ATG medialab.

Although mapping the Milky Way is challenging because we are inside it, our home galaxy remains the best example for visualizing these galactic components. Figure 1.2 illustrates an impression of the Milky Way, showing a face-on view on the left and an edge-on view on the right. The face-on view reveals the bulge’s elongated, bar-like structure, which contains billions of old, red stars (Fraknoi et al. [2016]). In the galactic center resides the SMBH Sagittarius A*. The spiral arms, which host our solar

system, extend outward from the ends of this peanut-shaped bulge. These arms are regions of active star formation and are rich in gas and dust. The edge-on view highlights the flattened structure of the disk, which, in the Milky Way, consists of two components: a thin disk hosts young, blue stars and regions of gas and dust which is embedded in a thicker, more diffuse disk populated with older stars (Fraknoi et al. [2016]). Both the bulge and the disk are embedded within the visible stellar halo and the much larger, invisible dark matter halo, which together form the galactic halo.

1.2 Galaxy Morphology

Looking back to Figure 1.1, we can see the different shapes and sizes of the galaxies within the Local Group. For instance, due to our position in the Local Group, the Andromeda Galaxy seems to appear more elongated compared to the Milky Way and these two are completely different from the rounder shape of M32, one of the satellite galaxies of Andromeda.

One of the first classification schemes was introduced by Hubble [1926] and is illustrated in Figure 1.3. Hubble classified galaxies into four main types of morphology: elliptical, lenticular, spiral, and irregular. This classification is based on the presence (or absence) and shape of two galactic structures: the bulge and disk.

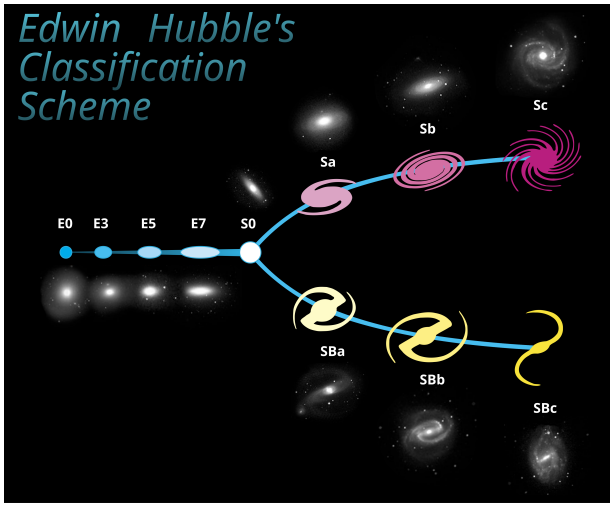

Figure 1.3: Classification Scheme of Edwin Hubble, also known as the Hubble tuning fork diagram. The illustration was made by Cosmogoblin [2022]. The scheme shows three out of the four main types of galaxy morphology by Hubble [1926]. Ellipticals are represented with En, where $n = 1, 2, ..., 7$ indicates the ellipticity of the galaxy. Lenticulars by S0, indicate the transition between the two branches. Lastly, spirals, where S is for normal spirals and SB is for barred spirals. The lowercase letters, a, b, and c, indicate early, intermediate, and late, respectively. Irregular galaxies are not shown in this illustration.

Elliptical galaxies lack disks and are structurally simple, consisting solely of a bulge component. Consequently, they contain little to no gas or dust and exhibit red colors, characteristic of older and metal-rich stellar populations (Mo et al. [2010]; Fraknoi et al. [2016]). The brighter an elliptical galaxy, the redder it is. Hubble classified them with En, where $n = 1, 2, ..., 7$ indicates the ellipticity of the galaxy. The ellipticity is calculated using $10(a-b)/a$, where a and b are the lengths of the semi-major and semi-minor axes of the galaxy, respectively (Hubble [1926]; Mo et al. [2010]). Thus, E0 galaxies appear as perfectly round spheres while E7 galaxies appear more elongated. Figure 1.4 shows two examples of elliptical galaxies on the top: NGC 4378 classified as E1 and NGC 3377 classified as E6.

In contrast, spiral galaxies have both a bulge, a disk, and sometimes a bar. Their disks contain young stars, HII regions, and dust columns, making them dynamic sites of active star formation. This means these regions often host massive, short-lived OB-type stars with low metallicity, which contribute to their bluer appearance (Fraknoi et al. [2016]).

The color-morphology relation in galaxies is not always as straightforward as it might seem. For instance, galaxies with thick, dense columns of dust can absorb shorter (blue) wavelengths of light and reemit this radiation at longer (red) wavelengths, causing a spiral galaxy to appear redder than it intrinsically is.

Spiral galaxies are divided into two main branches: normal spirals and barred spirals. Normal spirals (classified as S) have spiral arms that extend directly from the bulge, while barred spirals (classified as SB) feature a central bar structure across the bulge, with the spiral arms originating from the ends of the bar. Both types are further categorized into three subtypes —a, b, and c— based on the following criteria (Hubble [1926]; Mo et al. [2010]; Fraknoi et al. [2016]):

- the fraction of light being emitted by the bulge;
- the tightness of the curvature of the spiral arms;
- the degree to which the spiral arms resolve into stars, HII regions, and dust columns.

Hubble also referred to these subtypes as early (a), intermediate (b), and late (c) spirals (Hubble [1926]), implying an evolutionary sequence (Murdin [2001]; see Figure 1.3). These parameters are interrelated: for example, normal spiral galaxies classified as Sa typically have a very prominent, luminous bulge, tightly curved spiral arms, and faint HII regions. In contrast, Sc galaxies generally exhibit loose spiral arms, a relatively faint bulge, and bright HII regions (Hubble [1926]; Mo et al. [2010]). Figure 1.4 illustrates four examples of spiral galaxies (the 3 in the middle and the first at the bottom): NGC 175 (SBa), NGC 6814 (Sb), NGC 4565 (Sb, edge-on), NGC 5364 (Sc). Notably, both the Milky Way and the Andromeda Galaxy are barred spiral galaxies classified as SBb (Fraknoi et al. [2016]).

Lenticular galaxies exhibit a morphology that lies between ellipticals and spiral galaxies. They feature a prominent bulge, lack spiral arms, and have a thin, faint disk. These galaxies are classified as S0, while those with a central bar are designated as SB0 (Mo et al. [2010]). Figure 1.4 includes an example of a lenticular galaxy, NGC 5866 (S0), shown at the top right.

Hubble also identified galaxies that did not fit into any of the established categories and classified them as irregular galaxies (Irr). These galaxies lack a clear spiral structure and a pronounced bulge at their center. Instead, they display scattered HII regions, faint and fragmented spiral features, and no clear symmetry (Mo et al. [2010]; Fraknoi et al. [2016]). Figure 1.4 shows two examples of irregular galaxies at the bottom: Ho II, and NGC 520.

In the literature, ellipticals and lenticular galaxies are often referred to as early-type galaxies, while spirals and irregular galaxies are classified as late-type galaxies. This terminology originates from the historical belief that elliptical galaxies could evolve into spirals, with irregulars sharing more traits with spirals than with ellipticals. While this evolutionary sequence has since been disproven, the terminology still holds nowadays (Mo et al. [2010]; Murdin [2001]).

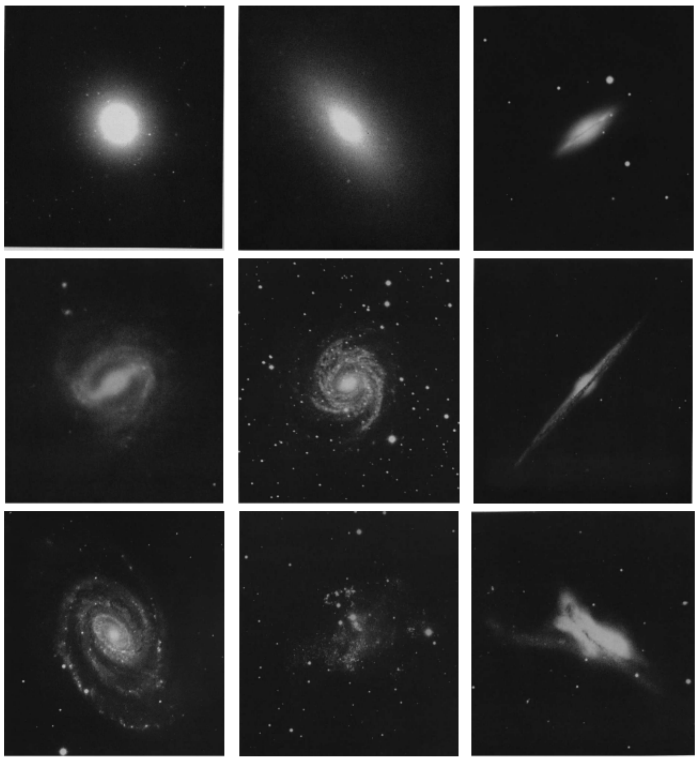

Figure 1.4: Examples of galaxies with different morphologies. From left to right and top to bottom: NGC 4278 (E1), NGC 3377 (E6), NGC 5866 (SO), NGC 175 (SBa), NGC 6814 (Sb), NGC 4565 (Sb, edge on), NGC 5364 (Sc), Ho II (Irr), NGC 520 (Irr). Composite image taken from Mo et al. [2010].

1.3 Galaxy Properties

Galaxies are far from being static astronomical objects and have undergone significant changes over billions of years. Studying their formation and evolution, even if isolated, is essential to understanding the universe we observe today and comparing it to the universe 13.8 billion years ago. We explored the morphology of galaxies in Section 1.2 and even gave a few insights about their different properties. In this section, we will study in more detail those properties, with a particular focus on the role of star formation in galaxy evolution.

Star formation has played a fundamental role in shaping galaxies throughout cosmic history. It influences not only the luminosity and appearance of galaxies but also affects their chemical composition and long-term structure. Consequently, in the context of galaxy evolution, it is important to categorize galaxies based on their SFR. These categories range from passive systems with little to no star formation, to actively star-forming galaxies, and extreme cases known as starbursts. The relationship between these categories becomes evident when considering the processes at work in elliptical, lenticular, and spiral galaxies, as well as the variations in SFR across cosmic time.

Elliptical and lenticular galaxies are typically classified as passive galaxies. Their stellar populations consist predominantly of old stars, indicating that star formation ceased long ago. After an initial period of star formation early in their histories, these galaxies exhausted or ejected most of the cold gas necessary for further star formation. Without the raw material needed to form new stars, these galaxies have entered a phase of passive evolution (Murdin [2001]).

Color is an important parameter that can indicate the age of a galaxy and its star formation activity. It is the difference in magnitude between two filters and magnitudes are a measure of the brightness of

an object. Higher magnitudes correspond to fainter objects and lower magnitudes correspond to brighter objects.

Passive galaxies, having ceased star formation long ago, are dominated by older, cooler stars such as red giants and low-mass stars. These stars emit no blue and ultraviolet light, giving passive galaxies their characteristic red color. Thus, the red arises from the absence of young, hot, blue stars that are typically found in actively star-forming regions. Similarly, the bulges of spiral galaxies, which share characteristics with elliptical galaxies, also appear reddish due to their older stellar populations and low star formation activity.

Metallicity is the abundance of elements heavier than hydrogen and helium and it is a byproduct of stellar nucleosynthesis, where successive generations of stars create and disperse heavier and heavier elements into the ISM. As a result, galaxies hosting older stellar populations typically exhibit relatively high metallicities, reflecting the cumulative enrichment of their gas over time. However, this is simply a concept as there is a degeneracy between the age of stellar populations and the metallicity because of the dust. Galaxies can appear old, but be metal-poor due to the presence of dust which makes the galaxy redder in color, characteristic of older galaxies.

In contrast, star-forming galaxies continue to produce new stars, although at varying rates. These galaxies sustain ongoing, though often reduced, star formation driven by a steady supply of gas. Despite this, the current rate of star formation in spirals is generally lower than it was in the past (as we will explore in more detail later). Over billions of years, spirals have consumed much of their available gas, and their overall star formation efficiency has declined.

Star-forming galaxies, particularly the disks of spirals, exhibit a blue color due to the ongoing formation of young, massive stars. These stars are exceptionally bright and emit significant amounts of blue and ultraviolet light. Although their lifespans are relatively short, their intense luminosity dominates the red light from older stars. As the star formation rate decreases over time, galaxies gradually shift toward redder colors, as the population of massive blue stars diminishes and the light from older, redder stars begins to dominate —blue massive stars have shorter lifespans than red smaller stars.

As star-forming galaxies continue producing stars over billions of years, their metallicity increases. This is driven by the ongoing cycle of star formation, stellar evolution, and supernova explosions, which enrich the interstellar gas with heavier elements and are then incorporated into successive generations of stars. Consequently, younger stars in spiral disks typically have higher metallicities than the ones formed a generation before, reflecting the cumulative chemical enrichment over time of the ISM. However, this enrichment is not uniform across the galaxy. Metallicity decreases with increasing galactic radius (Mo et al. [2010]), forming a gradient. The inner regions, which have experienced more sustained and rapid star formation, tend to be more metal-rich than the outer regions, where star formation has been less frequent and less efficient. Another phenomenon that can happen is that galaxies can accrete pristine gas from their surrounding which, in turn, dilutes their metallicity.

At the extreme end of the star-forming spectrum are starburst galaxies, which undergo periods of intense and rapid star formation, far exceeding that of typical star-forming galaxies (Mo et al. [2010]; Fraknoi et al. [2016]). These bursts can be triggered by events such as galaxy mergers, which compress large amounts of gas and ignite dramatic increases in star formation (Murdin [2001]; Fraknoi et al. [2016]). During a starburst, the galaxy produces as many massive, hot, blue stars in just a few million years as a normal galaxy might form over billions of years. However, these phases are typically short-lived, as the galaxies rapidly consume their gas reservoirs. Once the starburst subsides, and the massive stars quickly evolve into supernovae, the galaxy transitions toward a redder color and a more quiescent or passive state. In some cases, if further star formation is suppressed, the galaxy may come to resemble

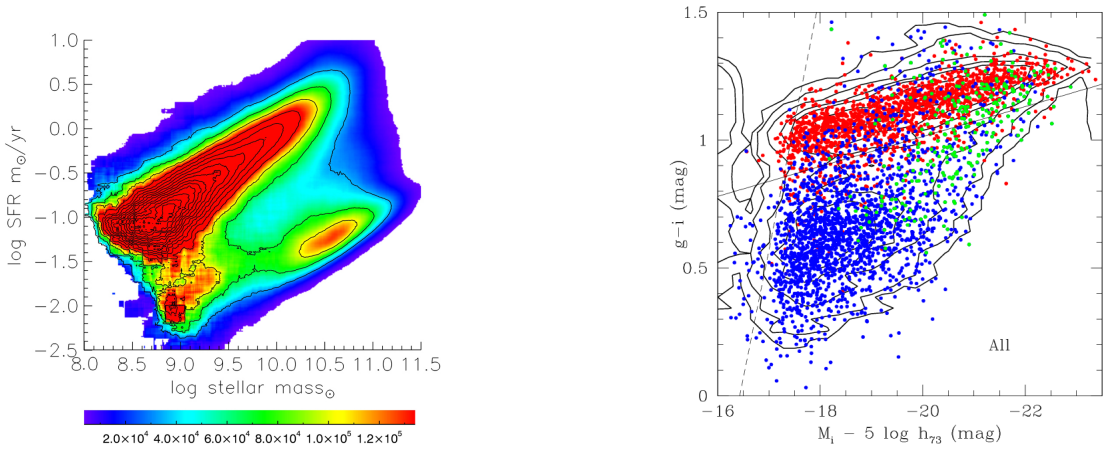

Figure 1.5: *Left:* Star-formation versus stellar mass relation for local galaxies in the SDSS database for $0.020 < z < 0.085$. The colorbar indicates the number density. Two prominent clouds are shown in red, one for star-forming galaxies (top) and one for the quenched ones (bottom right). The bottom left, the green valley, is populated by a mixture of galaxies with low SFRs and low stellar mass. *Right:* $g—i$ color versus i-band absolute magnitude. Red points are early-type galaxies (dwarf E-E-S0); blue points are disk galaxies (Sbc-Irr); green are bulge galaxies (Sa-Sb). The continuum line represents the separation between the two categories and the dashed line represents the effect of the limiting magnitude of SDSS. Images and captions from Renzini and Peng [2015] and Gavazzi et al. [2010], respectively.

an elliptical or lenticular galaxy, characterized by older stellar populations and limited star formation activity.

We have briefly mentioned that star-forming galaxies transition to quiescent galaxies when they exhaust their fuel to form stars or if their star formation is suddenly suppressed. Galaxies in this temporary state are said to be in the ”green valley” (Renzini and Peng [2015]). The green valley refers to a transitional phase between the two main populations of galaxies: the blue, star-forming galaxies, and the red, passive galaxies. The term originates from the color-magnitude diagram where galaxies are plotted according to their brightness (magnitude) and color (difference of magnitudes between two filters; see right side of Figure 1.5). In such diagrams, actively star-forming galaxies —dominated by young, hot, blue stars — populate the “blue cloud,” while older, redder, and passive galaxies lie within the “red sequence.” The green valley occupies the region between these two populations, representing galaxies in the process of quenching their star formation (Gavazzi et al. [2010]).

A similar distinction is visible in plots of SFR as a function of stellar mass (see the left side of Figure 1.5). In these plots (Renzini and Peng [2015]), the large cloud at the top represents star-forming galaxies, which exhibit relatively high SFRs and low stellar masses as they are still evolving. The small cloud at the bottom right represents passive galaxies, which show lower SFRs but higher stellar masses, having already evolved. The remaining population, a smaller cloud in the middle, corresponds to green valley galaxies—those with low SFRs and low stellar masses, transitioning or nearing the end of their transition to the passive phase.

Galaxies in the green valley are a very interesting topic of research, as they provide insight into the mechanisms driving the cessation of star formation, a process referred to as “quenching.” Several mechanisms can cause quenching. For example, in spiral galaxies, star formation may decline or cease altogether due to the depletion of cold gas, which is the raw material needed for forming new stars. This depletion can occur naturally over time as the gas is gradually consumed by star formation, or it can be ejected by external events such as galaxy mergers, supernovae explosions, or feedback from accreting

SMBHs, AGNs. These phenomena can heat or eject gas from the galaxy, making it unavailable for further star formation.

Many green valley galaxies exhibit bulge-dominated structures with features such as dust lanes, faint rings, and disturbed outer profiles (Salim [2015]), resembling S0 galaxies. This morphological transformation is likely connected to the processes driving the quenching of star formation. For instance, a major galaxy merger can induce both a burst of star formation and its subsequent shutdown, eventually creating a more spheroidal, bulge-dominated system.

As mentioned before, the presence of young, blue stars, which have relatively short lifespans, plays a critical role in the color evolution of galaxies. As star formation declines, these massive, short-lived stars quickly burn out, leaving behind a population dominated by long-lived, redder stars such as red giants and low-mass stars. Without the ongoing formation of new, massive stars to replenish the supply of hot, blue light, the overall color of a galaxy shifts toward the red end of the spectrum. This phenomenon explains why green valley galaxies appear intermediate in color—they retain some ongoing star formation, but at a declining rate, while the population of older, red stars becomes more prominent.

It is important to recognize that not all green valley galaxies are necessarily transitioning toward a passive state, nor are all reddish galaxies truly passive. Some green valley galaxies may oscillate between periods of star formation and quiescence (Salim [2015]), driven by episodic events such as gas inflows, SN explosions, or mergers, which can temporarily reignite star formation. Similarly, some galaxies may appear red and passive not because they have ceased star formation but due to the presence of large dust columns. Dust absorbs the UV radiation emitted by hot, massive stars and reemits it at longer wavelengths, resulting in a redder observed color.

Interestingly, the SFH of the universe provides a broader perspective on these trends. When examining the global star formation rate density (the amount of solar mass produced per unit time and per unit volume at a given redshift), it becomes evident that the SFR was significantly higher in the past than it is today (Madau and Dickinson [2014]; Mo et al. [2010]). Figure 1.6 presents the SFH of the universe using FUV+IR observations.

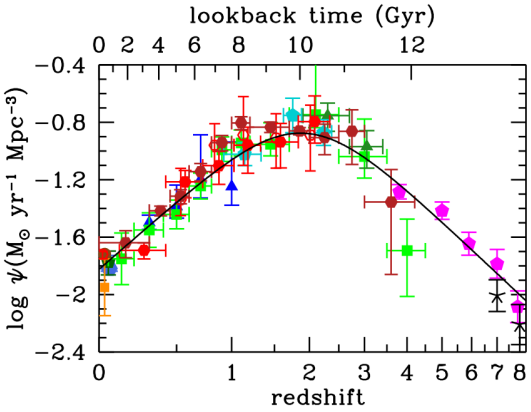

Figure 1.6: The history of cosmic star formation from FUV+IR rest-frame measurements as a function of redshift and lookback time, and its best-fitting function. The different colors and shapes of the points were taken from different papers, see Table 1 from Madau and Dickinson [2014]. Image taken from Madau and Dickinson [2014].

The data suggest that star formation rates rose steadily during the early epochs of the universe, at least up to the point where observations are currently possible. This implies that galaxies during earlier times experienced vigorous star formation phases. However, over the past several billion years, the available gas for star formation has become increasingly limited. Around redshift $z \sim 2$, the universe reached

the peak of cosmic star formation activity, after which the star formation process entered a slow decline, eventually reaching the low levels observed today.

Although we might be able to predict the factors causing this decline in star formation, the precise timescale of this process remains uncertain. The decline could result from a secular process, taking several billion years and producing a smooth trend. Alternatively, it might involve an abrupt mechanism followed by the passive evolution of the last generation of stars. In the latter scenario, galaxies could enter a ”post-starburst” phase, characterized by the coexistence of old and young stellar populations.

1.4 Post-Starburst Galaxies

Both photometry and spectroscopy of quiescent galaxies, spanning both high and low redshifts, have confirmed the presence of two distinct quenching mechanisms characterized by fast and slow timescales (e.g. Belli et al. [2019]; Wild et al. [2020]; Maltby et al. [2018]; Moutard et al. [2018])

To determine which process characterizes the quenching of a galaxy, it is essential to study systems that have been recently quenched, and PSB galaxies provide a key example. According to Maltby et al. [2018], PSBs are characterized as systems ”in which a major burst of star formation was rapidly quenched within the last few hundred Myr”. Therefore, PSB galaxies are the byproducts of fast-quenching timescales.

There are several ways to identify PSB galaxies. For instance, Whitaker et al. [2012] and Belli et al. [2019] used NIR photometric observations to identify ”young red-sequence” galaxies using UVJ color-color diagrams (explained in detail in Chapter 3). Similarly, Moutard et al. [2018] searched for young, low-mass galaxies in the NUVrK color diagram. On the other hand, Wild et al. [2014] introduced a new method using PCA-based analysis of rest-frame, broadband galaxy SEDs obtained from multi-wavelength photometry. This new approach was later confirmed with spectroscopy by Maltby et al. [2016].

Spectroscopically, it has been found that PSB galaxies display an excess of A and F-type (older) stars relative to OB-type stars (younger) which is confirmed by the lack of nebular emission lines (e.g. Goto et al. [2003]; Wild et al. [2007]; Wild et al. [2024]). The deficit of the OB-type stellar population and the enhancement of the A and F-type stellar population provide direct evidence of a recent and abrupt stop in star formation. As a consequence, PSB galaxies are characterized by strong Balmer absorption lines (indicative of A-type stars) and a lack of strong emission lines (indicative of the lack of OB-type stars; Wild et al. [2009]; Maltby et al. [2018]; Wild et al. [2024]).

Wild et al. [2009] defined a maximum timescale for PSB galaxies as being less than 650 Myr, with even shorter timescales of <350 Myr for galaxies with low gas mass. This conclusion aligns with the findings of Poggianti et al. [2009], who suggested a quenching timescale significantly lower than 1 Gyr.

In a more detailed study, Belli et al. [2019] examined PSB galaxies, defining their timescales to fall between 300 and 800 Myr. They also investigated the number density and percentage of PSB galaxies relative to passive galaxies, varying the threshold between 600 Myr and 1 Gyr. According to Belli et al. [2019], PSB systems ”have a roughly constant number density over the entire redshift range”, but their percentage when compared to the overall population of quiescent galaxies increases with redshift. This increasing proportion of PSB galaxies compared to ”normal” passive galaxies has also been corroborated by other studies, including Wild et al. [2009], Wild et al. [2016], Rowlands et al. [2018], and Forrest et al. [2018].

The trigger mechanisms for fast quenching vary with redshift. At high redshift, fast quenching is often associated with environmental factors and/or gas-rich mergers (e.g., Whitaker et al. [2012]; Wild et al. [2014]; Wild et al. [2016]; Belli et al. [2019]; Maltby et al. [2018]). At low redshift, mechanisms

such as stripping and/or minor mergers appear to dominate (e.g., Whitaker et al. [2012]; Maltby et al. [2018]).

1.5 Goals and Structure of the Thesis

The main goal of this work is to study the importance of PSB galaxies in the history of the universe, investigate their relative percentage at both high and low redshift, compute the quenching timescale for these systems using a different dataset from those employed in previous studies, and ultimately compare our findings with results from the existing literature.

Since the signatures of the different phases —active star-forming, green valley, and passive— are imprinted in the light emitted by galaxies, the methodology for this study is based on photometric observations taken at different wavelengths. By observing large samples of galaxies at different wavelengths and measuring their flux as a proxy of star formation activity and stellar population characteristics, we can establish selection criteria to classify galaxies into their respective phases. This data will then be employed to construct and analyze synthetic models, enabling us to achieve our goals.

The structure of this work is as follows:

- Chapter 2 focuses on the preparation and basic analysis of our sample, derived from the extensive photometric dataset of COSMOS2020 (Weaver et al. [2022b]). Here, we clean the data and examine its properties.
- Chapter 3 applies UVJ color-color diagrams to the selected sample, analyzing the galaxies in bins of redshift and cosmic time to identify trends and transitions.
- Chapter 4 involves the construction and analysis of a synthetic sample using `CIGALE` (Boquien et al. [2019]; Burgarella et al. [2005]; Noll et al. [2009]), reproducing the COSMOS2020 dataset.
- Chapter 5 identifies and characterizes PSB galaxies across different redshifts and time bins, providing a discussion and a comparison to other results in the literature.
- Chapter 6 presents the conclusion, summarizing the key insights from this work.

We assume a ΛCDM cosmology with $\Omega_M = 0.3$, $\Omega_\Lambda = 0.7$, and $H_0 = 70\,\mathrm{km\,s^{-1}\,Mpc^{-1}}$ throughout this work. All magnitudes will be given in the AB system (Oke and Gunn [1983]).

Chapter 2

Sample Selection

Astronomical surveys are a great tool for present-day astrophysics. They can be described as systematic observations of celestial objects and phenomena over large areas of the sky. They are often built using various telescopes and instruments worldwide to map the distribution of stars, galaxies, and other astronomical objects, as well as studying their properties and evolution. Astronomical surveys also aim to obtain comprehensive and statistically significant data sets that can be used to study various aspects of the universe, uncover rare or unexpected phenomena, identify new objects, and map the distribution of matter on different scales by observing large areas of the sky. They also provide valuable data for testing theoretical cosmology, galaxy, and stellar formation and evolution models. Thus, it is easy to understand that mapping the sky at different wavelengths plays a crucial role in advancing our understanding of the universe by providing astronomers with data sets that can be used to address a wide range of scientific questions that are still left to be answered.

Astronomical surveys use two primary observational techniques: photometric and spectroscopic measurements. Photometric surveys measure the brightness of celestial objects across different wavelengths of the electromagnetic spectrum; they provide information about the properties of stars and galaxies, including their environment, such as their colors, luminosities, and energy distributions. On the other hand, spectroscopic surveys analyze the spectra of celestial objects, splitting their light into its component wavelengths. Spectroscopy allows us to determine the chemical composition, temperature, and velocity of astronomical objects. The use of both photometric and spectroscopic surveys is essential in advancing our understanding of the universe, as they complement each other since they cannot provide all the necessary and important information alone. Other than the different observational techniques, there are several types of astronomical surveys. For instance, sky surveys aim to map the entire celestial sphere, or significant portions of it, across different wavelengths, from radio to gamma rays. Examples include the SDSS (York et al. [2000]; latest data release in Almeida et al. [2023]) and the Pan-STARRS survey (Chambers et al. [2016]).

Stellar surveys focus more on studying stars within our galaxy and nearby stellar populations. They aim to characterize the properties of stars, such as their brightness, color, temperature, composition, age, and evolutionary state. The Gaia mission by the ESA is an example of a stellar survey (Prusti et al. [2016]).

Finally, galaxy surveys are dedicated to studying the distribution and properties of galaxies in the universe. They are very similar to sky surveys, but galaxy surveys tend to select a smaller region of the sky. They provide valuable information on the large-scale structure of the cosmos, galaxy formation and evolution, and the nature of dark matter and dark energy. Cosmic surveys employ a variety of techniques, such as galaxy redshift surveys, gravitational lensing studies, and observations of the cosmic microwave

background radiation, to probe different aspects of the large-scale structure of the universe. Moreover, galaxy surveys also provide insights into the connection between galaxies and their environments, the role of dark matter in shaping cosmic structures, and the nature of galaxy clusters and superclusters. By analyzing the data collected from these surveys, astronomers can reconstruct the history of cosmic expansion, constrain cosmological parameters, and test theories of galaxy formation and evolution.

COSMOS (Scoville et al. [2007a]) is the first astronomical survey ever done with the HST to probe the formation and evolution of galaxies, AGNs, and dark matter as a function of cosmic time and to understand the large-scale structure in the universe. It is a deep, wide area, multi-wavelength survey tracing celestial bodies over a period corresponding to $\sim 75\%$ of the age of the Universe (Scoville et al. [2007a]; Scoville et al. [2007b]). The COSMOS survey began in 2003, imaging a field area of approximately 2 square degrees with the HST ACS WFC (Scoville et al. [2007a]; Scoville et al. [2007b]; Koekemoer et al. [2007]; Weaver et al. [2022b]). It is centered at (J2000) RA +150.11916667 (10:00:28.600) and DEC +2.20583333 (+02:12:21.00), see Figure 2.1 for a schematic of the COSMOS field in the sky.

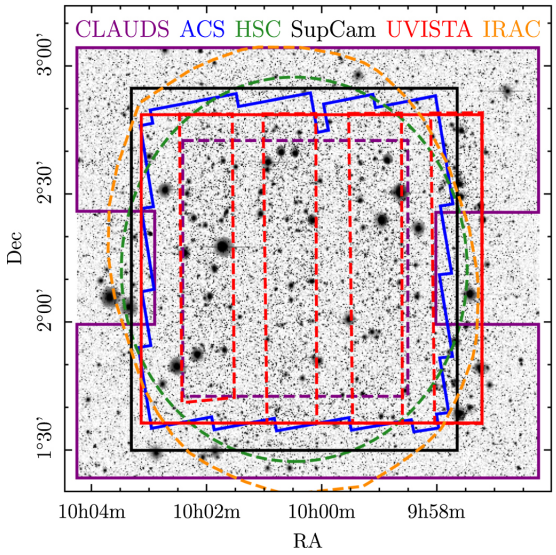

Figure 2.1: Schematic of the COSMOS field in the sky with the observations of each instrument. The solid lines represent survey limits, and the dashed lines indicate the deepest regions of the images. Image and caption taken from Weaver et al. [2022b].

Its data uses not only the HST (0.83 microns) but also the Galaxy Evolution Explorer (0.15-0.23 microns), the Spitzer Space Telescope (3.57-8.00 microns), and the ground-based Visible and Infrared Survey Telescope for Astronomy (1.02-1.19 microns), Canadian-France-Hawaii Telescope (0.37-0.39 microns) and Subaru Telescope (0.48-0.82 microns; Weaver et al. [2022b]). Since the survey is carried out in multiple wavelengths, allowing astronomers to study different aspects of galaxies and the universe, COSMOS provides a comprehensive view of the cosmos, enabling us to address a wide range of scientific questions.

Therefore, we base our work on data from the COSMOS survey and in particular from the latest multiwavelength catalog presented in Weaver et al. [2022b], COSMOS2020. The catalog contains 1,720,700 sources within an area of approximately 2 square degrees represented in the COSMOS field schematic in Figure 2.1, however, to ensure a complete representative sample of the universe, we need to clean and refine our data.

Firstly, we initiated the cleaning process by filtering out bad data with `FLAG_COMBINED` = 0, which cleans and flags the data inside UltraVISTA, Subaru HSC, and Subaru Suprime-Cam limits, see Figure

2.1. While the COSMOS2020 survey primarily focuses on galaxy evolution, it contains a variety of other celestial objects, including stars, AGNs, and potential fake detections. To address this and to polish the sample at its maximum, we took advantage of the two fitting algorithms used in COSMOS2020, photometric redshift codes `LePhare` (Arnouts et al. [2002]) and `EAZY` (Brammer et al. [2008]). Both methods use specific tailored galaxy templates to reproduce the observed photometry. Through the best template fit of such methods, relevant physical parameters are retrieved which will then be used in the rest of thesis (e.g. photometric redshift, stellar mass, star formation rate, mass-to-light ratio in the V-band, light-weighted age in the V-band, extinction in the V-band, infrared luminosity; Weaver et al. [2022b]). We will use both of these codes to achieve a complete and clean final sample. These steps are very important as they will minimize the errors in our calculations and conclusions; they remove data such as outliers or bad-fitting data, assuring our sample has well-controlled biases. Thus, we took advantage of `LePhare` code provided by the catalog, which employs both galaxy and stellar templates for photometric fitting Weaver et al. [2022b]. Specifically, we retained only those sources classified as galaxies by `LePhare` (`lp_type` = 0).

Furthermore, we encountered outliers in the SFR and restframe fluxes for the $UBVJ$ bands (see Chapter 3) with the `EAZY` template code for computing the photometric redshift, akin to `LePhare`. Notably, some sources exhibited unphysical SFRs and others had missing restframe flux data, so we excluded those as well.

Additionally, the COSMOS2020 catalog incorporates a selection criterion based on HST ACS morphology, categorizing objects into galaxy (1), star (2), and fake detection (3) classes. Since not all COSMOS2020 sources have undergone HST observation, we selected the objects whose selection was not equal to 2 or 3.

Following these steps, our dataset is reduced to 666,474 sources. However, despite these efforts, our sample remains far from having well-controlled biases and so requires further refinement to truly reflect, as much as possible, the characteristics of the universe traced by the observations.

Surveys, like COSMOS, are magnitude-limited, this means there is a minimum magnitude, or minimum flux, that the survey can detect —they are observed with the instrument detectors of telescopes which, per se, have a minimum number of photons they can detect. The flux (F) of an object is the amount of energy received per unit area per unit of time and is related to luminosity (L), the total power emitted by the object, by,

$$F = \frac{L}{4\pi D_L^2}, \tag{2.1}$$

where D_L is the luminosity distance of the observer to the object. Since galaxy luminosity is also related to the stellar mass of the object (Fraknoi et al. [2016]), this implies that if surveys are magnitude-limited then they must also be mass-limited —i.e. there is a minimum mass that the survey can detect, M_{min}. Therefore, mass completeness in galaxy surveys refers to the ability of the survey to detect and catalog galaxies above a certain mass threshold and below a certain magnitude. This means that we can potentially observe any kind of galaxy that falls within this criteria with our survey.

Different galaxies have different masses, and they emit light across various wavelengths, but they can also emit the same flux, depending on the age of their stellar populations and their distance. Observational challenges arise due to factors such as instrumental limitations, background noise, and sensitivity thresholds. Some telescopes or detectors may be more sensitive to certain mass ranges, leading to incomplete observations. An instrument with high sensitivity can detect fainter and lower-mass galaxies, providing a more complete picture of the galaxy population. On the other hand, less sensitive instruments may miss lower-mass galaxies. Thus, we set mass thresholds to define the completeness limits of a survey.

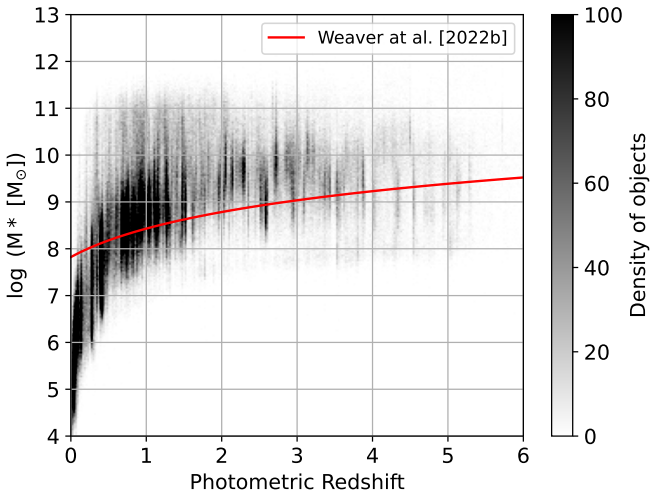

Figure 2.2: Mass completeness represented by the stellar mass versus photometric redshift plot, both from the EAZY template code. The plot is colored according to the density of sources, represented by the colorbar on the right side of the figure. The red line illustrates the mass completeness line, Eq. 2.2, given by Weaver et al. [2022b].

For example, a survey might be considered 90% mass complete for galaxies with masses above a certain threshold. This threshold is the minimum mass at which the survey reliably detects and catalogs those galaxies. If a survey is considered 20% complete then most of the galaxies are below the mass threshold and the survey is considered incomplete. It is important to note that biases introduced by incomplete surveys need to be carefully accounted for when deriving the properties of the galaxies.

Using the method from Pozzetti et al. [2010], M_{min} can be derived from the limiting stellar mass of each galaxy, M_{lim}. In other words M_{lim} is the mass a galaxy would have, at its redshift, if its apparent magnitude were equal to the limiting magnitude, m_{lim}, of the survey, $\log(M_{lim}) = \log(M) + 0.4(m + m_{lim})$. M_{min} is then defined when we constrain M_{lim} below a certain magnitude.

For COSMOS2020, the mass completeness line, or M_{lim} in bins of redshift, is given by Weaver et al. [2022b],

$$M_{lim}(z) = -1.51 \times 10^6(1+z) + 6.81 \times 10^7(1+z)^2, \tag{2.2}$$

for $z < 6$, as shown in Figure 2.2.

We analyzed the sources positioned above the delineated threshold, M_{lim}, as illustrated by the red line — the mass completeness line — in Figure 2.2. This figure shows the density plot of the stellar mass (`ez_mass`) versus the photometric redshift (`ez_z_phot`) of the sample until redshift 6.0. When mentioning photometric redshift the one used will always be the EAZY one, `ez_z_phot`. The mass threshold can serve as a criterion for establishing completeness within our dataset.

COSMOS calculates photometric redshifts (e.g. `ez_z_phot`) using template-fitting methods. EAZY and LePhare codes compare observed photometry across multiple filters to synthetic SED models that represent different galaxy types at various redshifts. The SED models are redshifted and interpolated with the filter transmission curves to compute synthetic photometry at each redshift. By minimizing a goodness-of-fit metric, such as χ^2, COSMOS identifies the redshift and template that best matches the observed data.

Figure 2.3 illustrates a 3D diagram of the H-band magnitude from 29 to 23 with a step of 2 magnitudes versus several 0.5 redshift bins from 0 to 6.0. The H-band used was `UVISTA_H_MAG_AUTO`, total flux provided by `SExtractor` using UltraVISTA and defined as the flux contained within the band-independent Kron radius (Weaver et al. [2022b]; Kron [1980]). This analysis is important as the H-band is a proxy

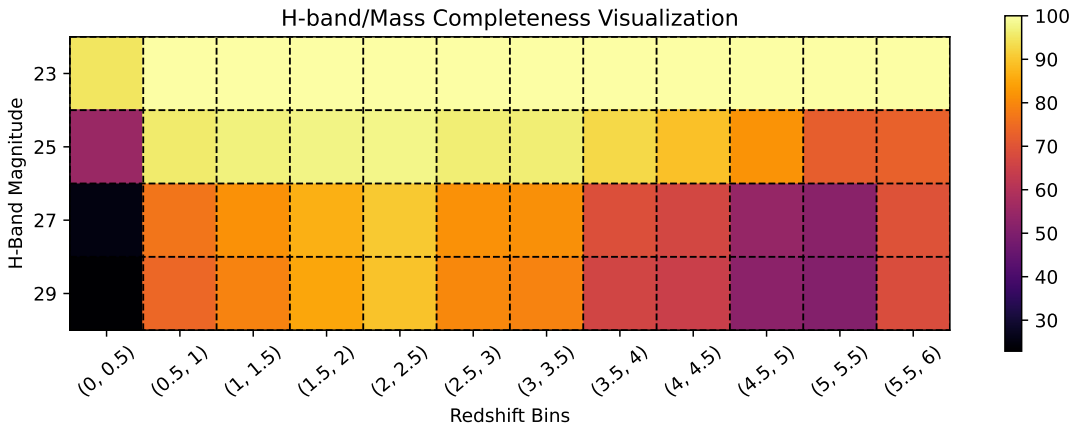

Figure 2.3: H-band magnitude versus redshift bins diagram colored according to the percentage of the sample above the completeness line in Figure 2.2. The colorbar on the right side of the figure represents this percentage.

for stellar mass (Dai et al. [2021]) and gives an insight into the mass completeness of our sample. The H-band is located in the NIR bands where old and cold stars emit radiation. These stars make up the bulk of the old population and due to their long lifespans, they make most of the stellar mass of the galaxy.

The diagram is colored according to the percentage of sources with a certain H-band magnitude and in a certain redshift bin above the mass completeness line in Figure 2.2. For example, only $\sim 20\%$ of the sources with an H-band magnitude of 29 in the redshift bin $(0, 0.5)$ are above the mass completeness line. From this example, we can easily conclude that the sample is not representative of the Universe at those ranges since we only have a completeness of 20%. Therefore, we selected the sources, above the mass threshold, between redshifts 0.5 and 3.5 with an H-band magnitude lower than 27. This selection gives a completeness higher than 75%, as depicted in Figure 2.3.

Next, we imposed a SNR (`UVISTA_H_FLUX_APER2` divided by `UVISTA_H_FLUXERR_APER2` which are fluxes and its errors measured in 2" diameter apertures extracted with `SExtractor` Weaver et al. [2022b]) higher than 3 on the sources we selected above, reducing the sample to 250,669 objects.

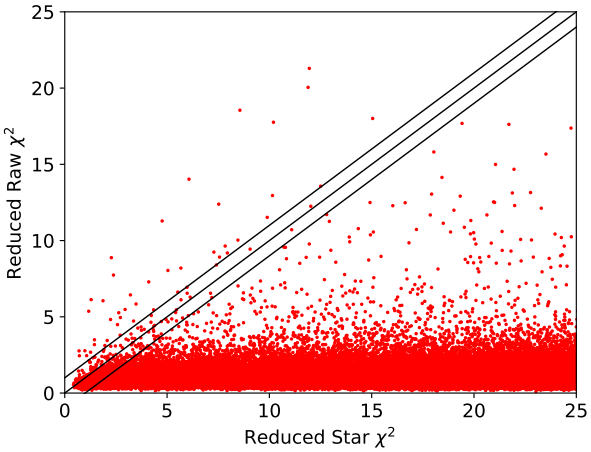

Figure 2.4: Scatter plot of the reduced χ^2 of the stellar and galaxy template of the `EAZY` template code. The three black lines represent $y = x + 1$, $y = x$, and $y = x - 1$, respectively (Lampton et al. [1976]).

Finally, we did a χ^2 analysis which is a statistical tool that measures the goodness-of-fit metric where all the χ^2 come from best-fitting the photometric data to, in our case, the `EAZY` SED fitting tool. This

analysis lets us pick the good solutions, in simpler words, whether an object is best fitted on a stellar or a galaxy template.

Figure 2.4 shows the plot of the reduced raw χ^2 (i.e., χ^2 divided by the degrees of freedom) of the galaxy versus the reduced χ^2 of the best stellar template. Since the catalog does not have reduced χ^2 ($\chi^2_{\rm red}$), the values of `ez_raw_chi2` (galaxy) and `ez_star_min_chi2` (star) were divided by the degrees of freedom (d-1), where d is the number of photometric filters, `ez_nusefilt`. Next, we defined three lines, $y = x$, $y = x+1$, and $y = x-1$ according to Lampton et al. [1976] for a $\chi^2_{\rm red}$ with $p = 1$ degrees of freedom and 68 percent confidence. If an object lies above $y = x+1$, then the stellar template describes the object better than the galaxy one. If it lies in between $y = x+1$ and $y = x-1$, we are not sure which template is better. And if it lies below $y = x-1$ then the galaxy template is a better solution than the stellar one. Thus, we selected the galaxies that are below $y = x+1$ which are, most likely, best described by the galaxy template. Our final refined sample extracted from the COSMOS2020 catalog comprises **249,307 sources**.

2.1 Properties of the Selected Sample

Now that the sample is complete and representative of the universe, we shall focus on analyzing its properties. Figure 2.5 shows the distribution of the galaxy raw $\chi^2_{\rm red}$ (`ez_raw_chi2`) of the sample on the left. The number of sources with a high $\chi^2_{\rm red}$, e.g. higher than 4.0, is very low (1.77%) as most of the sample has a $\chi^2_{\rm red}$ value below 1.5 (82.13%). This tells us that the best solution for these sources is indeed the galaxy template. Specifically, the median χ^2 value stands at 0.84, with a standard deviation of 1.01, highlighting the overall quality and consistency of the data.

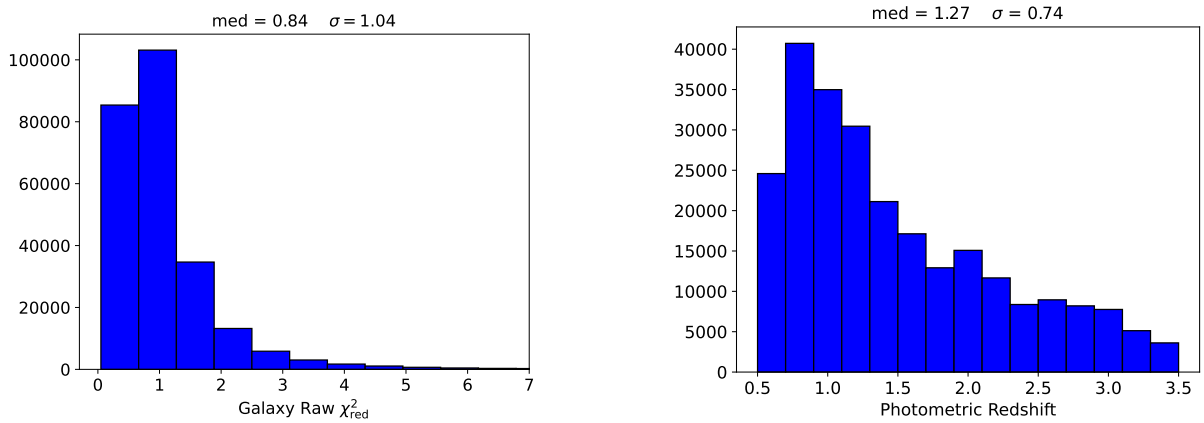

Figure 2.5: *Left:* Raw $\chi^2_{\rm red}$ distribution for the galaxy template using the `EAZY` fitting tool. *Right:* Photometric redshift distribution using the `ez_z_phot` from `EAZY`.

The distribution of photometric redshifts using the `EASY` template code, `ez_z_phot`, is illustrated on the right side of Figure 2.5. We observe two distinct families: one with redshifts below 1.5, corresponding to an age of the universe of 4.3 Gyr, representing about 60.74% of the total sample, and another with redshifts above 1.5, making up approximately 39.26% of the sample. As we move to higher redshifts, the number of sources decreases gradually because fainter objects become increasingly challenging to detect as we reach higher redshifts, resulting from a flux-limited survey.

The left side of Figure 2.6 shows the restframe AB magnitude distribution of the UVJ filters. The AB magnitudes (Oke and Gunn [1983]) were computed using the `EAZY` restframe fluxes, which correspond to the photometry of the best model in the UVJ restframe, with the following equation,

$$m_{\mathrm{AB}} = -2.5 \log_{10} \left(\frac{f_\nu}{3631\,\mathrm{Jy}} \right), \tag{2.3}$$

where f_ν is the spectral flux density in Jy units. From the graph, it is evident that filters with shorter wavelengths exhibit greater depth and luminosity. The U-band, in particular, shows higher luminosity, likely attributed to the presence of massive, young OB-type stars predominantly found in star-forming galaxies. These stars emit intense radiation due to their high temperatures. Furthermore, the U-band filter is less susceptible to detector temperature variations compared to the J-band in the infrared, which is why we can see fainter objects (higher magnitude) in the U-band. The J-band sensitivity to the detector temperature arises from its detection of infrared radiation, which is influenced by heat emissions. Even if detectors undergo cryogenic cooling, temperature fluctuations still occur, affecting the observed magnitudes. Independently of the detector used, old and low-mass type stars emit more in the J-band than in the U-band; these stars have a much lower temperature than the OB stars which makes them radiate at longer wavelengths. The drop in the number of sources at the faintest fluxes (higher AB magnitude), independently of the band filter, is due to incompleteness.

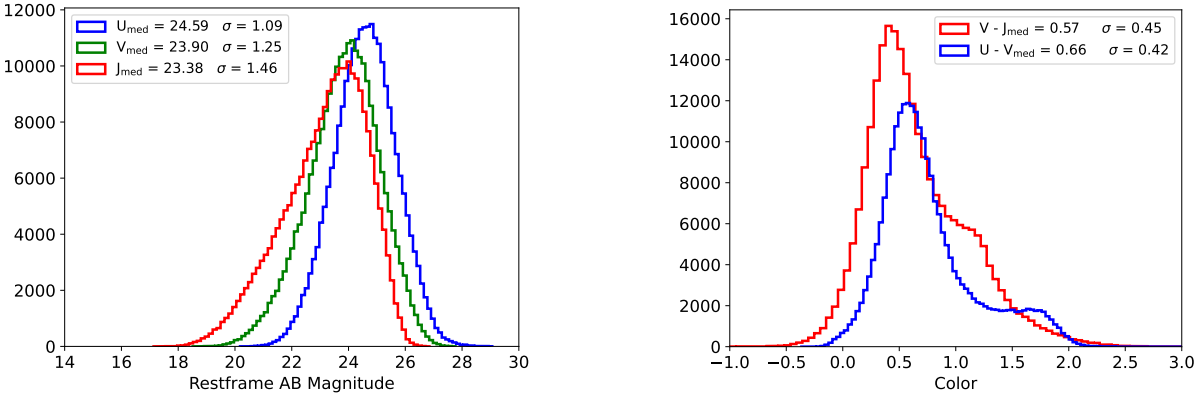

Figure 2.6: *Left:* AB magnitude distribution using the `EAZY` restframe fluxes U (blue), V (green), and J (red). *Right:* $U - V$ (blue) and $V - J$ (red) colors distribution

As mentioned in Chapter 1, color serves as a proxy for the temperature and age of the galaxies. A bluer object, indicated by a low value of $U - V$, typically represents higher temperature and younger age, whereas a redder color corresponds to higher $U - V$ values. Similarly, the $V - J$ color can provide insights into the presence of dust, with lower values suggesting a low concentration of dust and vice versa.

The right side of Figure 2.6 presents the color distribution of the sample for $U - V$ (in blue) and $V - J$ (in red). Regarding $U - V$, we see an evident bimodality, with the first peak representing blue or star-forming galaxies and the other indicating very red objects, possibly passive galaxies or heavily absorbed systems. Similarly, but less pronounced, the $V - J$ distribution displays a bimodal trend, with the first peak corresponding to dust-poor systems and another peak indicative of dusty environments.

Figure 2.7 illustrates the distribution of stellar mass, SFR, and sSFR within the sample, using the results by `EAZY` listed in the catalog (`ez_mass`, `ez_sfr` and `ez_sfr-ez_mass`, respectively). Galaxy masses span a range of $8.0 < \log(\mathrm{M}_* \,/\, [\mathrm{M}_\odot]) < 12.0$, with a typical mass of $\log(\mathrm{M}_* \,/\, [\mathrm{M}_\odot]) = 9.6$. The SFR typically falls between $-1.0 < \log(\mathrm{SFR} \,/\, [\mathrm{M}_\odot\ \mathrm{yr}^{-1}]) < 2.0$, although there is a tail towards lower SFR values, particularly below $\log(\mathrm{SFR} \,/\, [\mathrm{M}_\odot\ \mathrm{yr}^{-1}]) = -2.0$, indicative of passive galaxies. The sSFR, the ratio between SFR and the stellar mass of the galaxy, exhibits a typical value of $\log(\mathrm{sSFR} \,/\, [\mathrm{yr}^{-1}]) = -9.1$. Notably, around $\log(\mathrm{sSFR} \,/\, [\mathrm{yr}^{-1}]) = -8.0$, we encounter a limit imposed by SED fitting. This limit indicates that objects with SFRs exceeding $\log(\mathrm{SFR} \,/\, [\mathrm{M}_\odot\ \mathrm{yr}^{-1}]) = 0.5$ must possess stellar masses

of at least $\log(M_* / [M_\odot]) = 8.5$, implying they are more massive. Additionally, a small uptick is observed around $\log(\text{sSFR} / [\text{yr}^{-1}]) = -13.0$ which is attributed to the presence of massive passive galaxies.

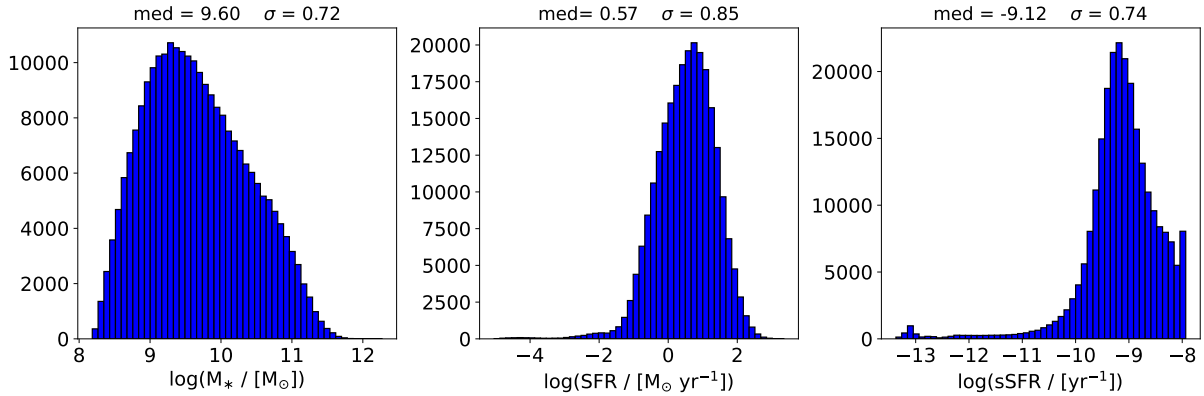

Figure 2.7: Log M_*, SFR and sSFR distribution using the `EAZY` fitting tool.

Figure 2.8 presents two distributions: on the left, the A_V in magnitudes, and on the right, the total LIR ranging from 8 to 1000 micrometers in solar luminosities, $L_\odot$. Both `ez_Av` and `ez_LIR` are from the `EAZY` template code. The code imposes a lower limit of 0.02 in the extinction plot, as negative extinctions lack physical meaning. The typical extinction value observed is 0.8 magnitudes. Conversely, in the LIR plot, we observe the distribution of dust, as it is predominantly emitted in the infrared spectrum. The median total infrared luminosity is $\log(\text{LIR} / [L_\odot]) = 10.5$.

In conclusion, these two plots tell us that COSMOS galaxies are not extremely extinct as most have an extinction lower than 1 mag. Additionally, they are not ultra luminous infrared galaxies that have $\log(\text{LIR} / [L_\odot]) > 11$. Therefore, the ore of our sample is characterized by starburst systems, regular star-forming, and passive galaxies, which are the ones we want to analyze.

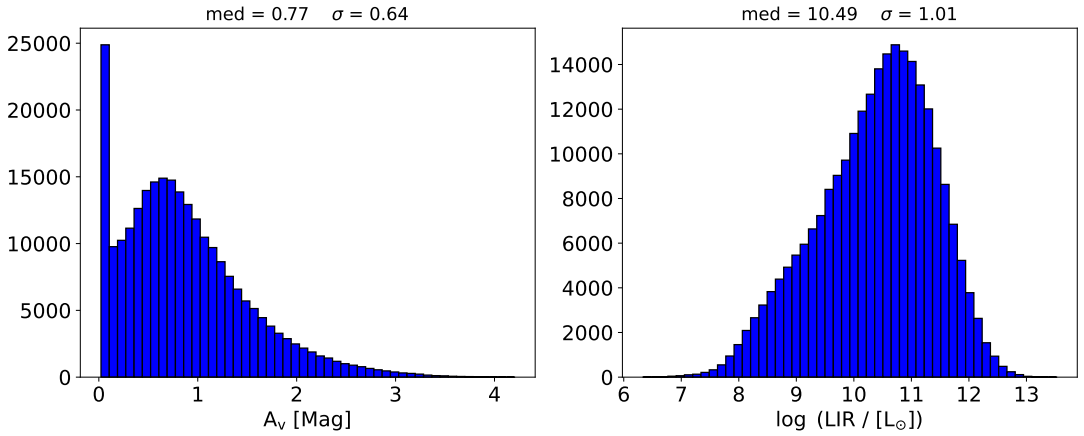

Figure 2.8: *Left:* Distribution of A_V using the `EAZY` template code. *Right:* Distribution of LIR using the `EAZY` template code.

This sample can also be characterized by two other quantities: the mass-to-light ratio and the light-weighted age. The mass-to-light ratio can tell us about what type of stars constitute the luminous population of the galaxies —either massive, young stars or old and low-mass stars, or even a mix of the two. By definition, the sun has a mass-to-light ratio equal to 1 $M_\odot/L_\odot$ (Fraknoi et al. [2016]). Elliptical galaxies tend to be very massive as they have a large abundance of evolved older stars that do not produce much

light, so these galaxies typically have a high mass-to-light ratio. On the contrary, star-forming galaxies have young stars that contribute a lot to the luminosity of the galaxies. While they are more massive, their abundance is not very high and so they typically have mass-to-light ratios lower than elliptical galaxies.

On the other hand, the light-weighted age gives us an estimate of the age of the stellar populations of the galaxies. A low value indicates that the galaxy is still producing stars, so its stellar population is young, while a higher value indicates the galaxy has stopped its star formation and is or has migrated to the passive region. Both these two quantities can correlate with each other: star-forming galaxies have low mass-to-light ratios and low light-weighted ages while passive galaxies have higher values.

Figure 2.9 displays these two distributions: on the left, the distribution of mass-to-light ratio in the V-band in $M_\odot/L_\odot$, and on the right, the distribution of light-weighted age in the V-band in Gyrs. We saw that the typical photometric redshift of the sample is 1.27 in Figure 2.5, which corresponds to ~ 5 Gyrs. Therefore, considering the definition of this parameter, if the median light-weighted age were equal to 5 Gyrs, the overall sample would have already migrated. The median age of stellar populations would be the age of the universe at that time, ~ 5 Gyrs. Because the median light-weighted age is 0.37 Gyrs —smaller than the 5 Gyrs—, it tells us that the galaxies are still forming stars. This can be confirmed by the left plot of Figure 2.9 where the median mass-to-light ratio is smaller than 1 $M_\odot/L_\odot$ which is characteristic of young stellar populations with very luminous stars.

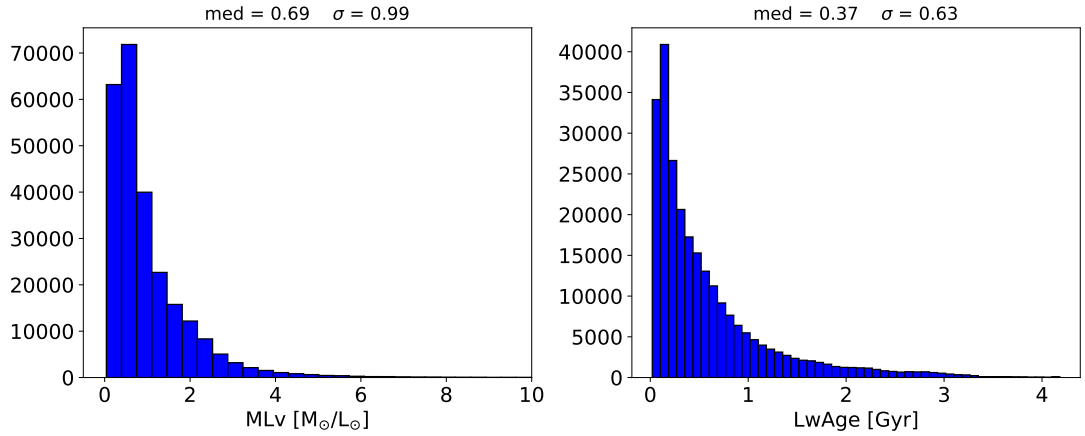

Figure 2.9: *Left:* Distribution of the mass-to-light ratio in the V-band using the `EAZY` template code. *Right:* Distribution of the light-weighted Age in the V-band using the `EAZY` template code.

Thus, from these two plots, our COSMOS sample mainly comprises SF galaxies. This will be studied in further detail in the next chapter, where we will analyze the sample using color-color diagrams.

Chapter 3

Methods

While studying the evolution of galaxies over the past 13 billion years, it is crucial to understand how the assembly of stellar mass behaves in both star-forming and quiescent galaxies. This can provide us information on how the different populations of galaxies we see today on our telescopes formed and interacted with each other and their medium. However, separating star-forming from quiescent galaxies can be quite challenging as there is no clear boundary between the two types.

In recent years, rest-frame color-color diagrams, particularly the UVJ diagram, have emerged as prominent tools for distinguishing between these two categories of galaxies (Williams et al. [2009]). Their popularity derives from the ability to delineate galaxy types within extensive photometric datasets, providing insights into the properties and evolutionary trajectories of galaxies. This diagram derives its name from the use of U, V, and J filters, representing different regions of the electromagnetic spectrum.

The U-band corresponds to ultraviolet wavelengths —the bluer part of the spectrum— with a central wavelength (median of the transmission curve) and width (full width of the transmission curve at half maximum) of 3709 and 518 Å, respectively. This band is more sensitive to massive, hot stars, which emit a lot of energetic UV radiation, making it a direct measurement of star formation.

The V-band corresponds to an intermediate band in the optical part of the spectrum with a central wavelength and width of 5487 and 954 Å, respectively. It can also tell us about the past and present star formation of a galaxy.

Lastly, the J-band extends into the NIR regime with a central wavelength and width of 12525 and 1718 Å, respectively. It represents the bulk of the old population and is a direct measurement of the mass of the galaxy as, in this regime, radiation from low-mass stars predominates. The values of the central wavelengths and widths were taken from Weaver et al. [2022b].

At its core, the UVJ color-color diagram serves as a diagnostic tool for classifying galaxies based on their observed colors in these filters. The distribution of galaxies within this diagram can provide information regarding their stellar populations, star formation histories, and the presence of interstellar dust. Galaxies with distinct properties occupy different regions of the UVJ diagram. For instance, galaxies with blue colors (low $U-V$) in the $U-V$ versus $V-J$ plane typically harbor young stellar populations characterized by intense star formation activity. In contrast, redder galaxies (high $U-V$) tend to exhibit older stellar populations, indicative of quiescent or passive systems characterized by a low or even absent star formation. Additionally, the position of galaxies in the UVJ diagram can also provide insights into the presence of interstellar dust, with dust-rich galaxies often displaying redder colors not only in $V-J$ (high $V-J$) but also in the $U-V$, tracing a diagonal in the diagram. This is demonstrated in Figure 3.1.

Thus, the UVJ diagram stands out as a powerful tool for categorizing galaxies due to its simplicity

and effectiveness. Unlike other alternative methods and diagrams, like color-magnitude or the spectral BPT diagrams, the simplicity of the UVJ diagram, with the use of 3 filters, makes it easily applicable to large photometric datasets like ours, enabling an efficient classification of galaxies based on their observed colors. In fact, by using UV, optical, and NIR wavelengths, the UVJ diagram can study the impact of dust and intense star formation on color measurements. This provides more accurate classifications of galaxy types, which is something other diagrams are not able to do on their own.

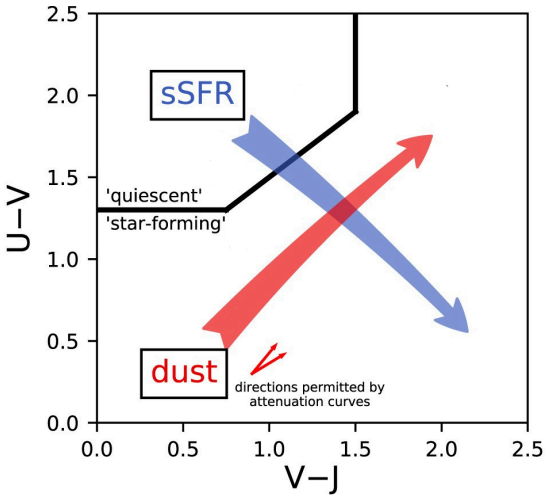

Figure 3.1: The UVJ diagram explained, adapted from Leja et al. [2019]. The blue and red arrows display the direction where sSFR and dust attenuation increase, respectively. The black lines separate between quiescent and star-forming galaxies.

Due to the large photometric-based dataset with 249,307 sources and the diverse number of advantages of the UVJ filters presented above, we are going to use the UVJ diagram to classify these galaxies into different types according to their color.

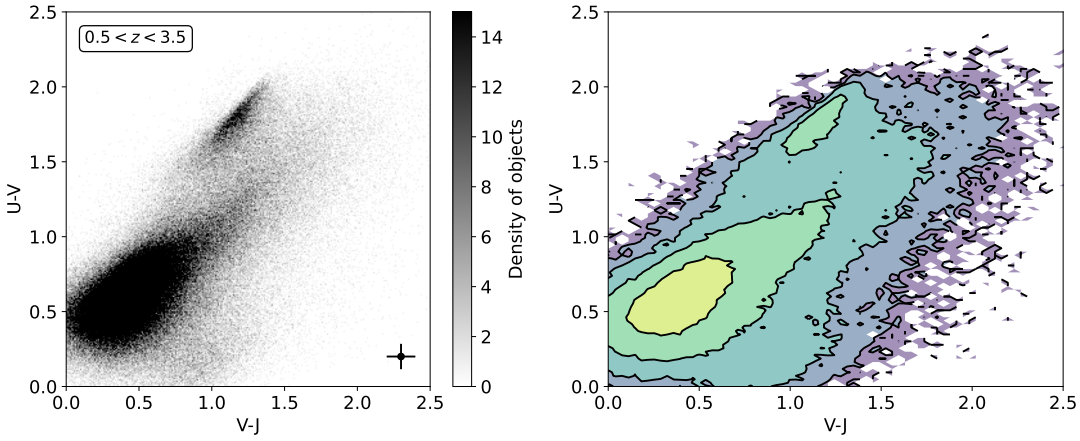

Figure 3.2: *Left:* The UVJ diagram colored according to the density of the total sample, which is reported by the colorbar. The typical photometric errors of the population are shown as a cross on the lower right side. *Right:* Contour of the sample in the UVJ diagram.

The color-color diagram of the sample is represented in Figure 3.2, its density on the left and the contour on the right. We can see that the sources are organized, approximately, into two clumps. The

redder ones correspond to the smaller group at the top and the bluer ones correspond to the bigger cloud at the lower left corner of the diagram. Thus, we can say that there is a clear bimodality in the sample between the red and blue sources, that is, between quiescent and star-forming galaxies. However, as shown in the figure, these clouds do not have clear boundaries —not all galaxies behave the same way and have the same constitution, and they can also be going through a quenching process, stopping their ongoing star formation and migrating to the red cloud.

Before classifying the galaxies into their respective category, we need to remember that the mean star formation rate in the Universe has evolved over cosmic time (Madau and Dickinson [2014]). Due to this aspect and for an easier tracking of such evolution, we divide the dataset into subsamples of $z = 0.5$ bins in Section 3.1 and into subsamples of different Gyr bins in Section 3.2, classifying the sources in those bins.

3.1 Subsamples Divided in 0.5 Redshift Bins

We divided the sample into different redshift bins, taking into account the work previously done by Williams et al. [2009] —our sample is divided with a range of 0.5, starting from $z = 0.5$ to $z = 3.5$. This is shown in Figure 3.3, where the plots are colored according to the density of the whole sample.

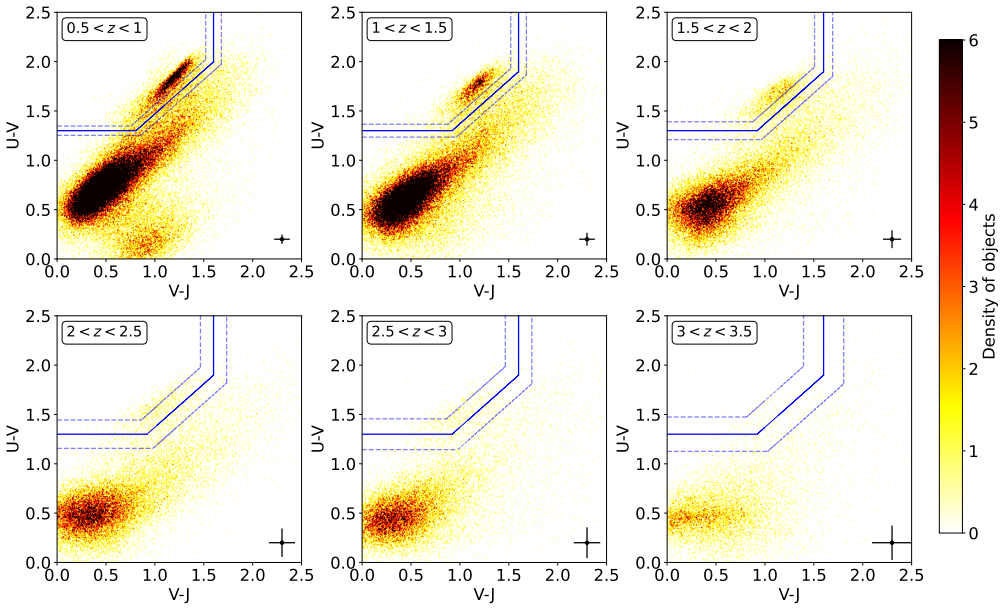

Figure 3.3: UVJ diagram divided into six 0.5 redshift bins and colored according to the density of the total sample, which is reported by the colorbar on the right side of the figure. The blue continuous line is taken from Williams et al. [2009], and the dashed lines are plotted according to the typical photometric errors of the population in each redshift bin and shown as a cross in the lower right side of each panel.

At high redshifts, i.e. $z > 2$, our sample is limited by the lack of sources and the presence of significant photometric errors —since the survey is flux-limited, faint sources cannot be detected, producing this limit. Most of the sources appear as very blue objects clustered in the lower left of the UVJ diagram. However, as we transition to lower redshifts, i.e. $z < 2$, the number of observed objects increases, and we notice a shift in their distribution: they begin to migrate upward towards the top-middle region of the diagram, known as the red cloud. This migration from the blue to the red region as redshift decreases results in the emergence of a bimodal distribution between red and blue galaxies, highlighting

the evolving nature of galaxy populations over cosmic time —we want to understand where and when this migration process occurs. Additionally, we also want to identify which galaxies within the sample are undergoing this transition and analyze their properties and how different they are from passive and star-forming galaxies.

Williams et al. [2009] empirically defined two regions to distinguish quiescent from star-forming galaxies. We adapted their selection criteria of the quiescent galaxies, corresponding to the continuous blue lines in Figure 3.3, which are

$$\begin{aligned} (U-V) &> 0.88 \times (V-J) + 0.59 \qquad [0.5 < z < 1.0] \\ (U-V) &> 0.88 \times (V-J) + 0.49 \qquad [1.0 < z < 3.5] \end{aligned} \tag{3.1}$$

for the diagonal lines. They also applied $U-V > 1.3$ and $V-J < 1.6$ to avoid contamination from unobscured and dusty star-forming galaxies in the quiescent region, respectively. Thus, in that study, sources lying inside the region in the upper left corner are defined as passive while everything that falls out of it is considered star-forming.

However, not all galaxies behave the same way and we can have galaxies that are neither star-forming nor passive and so we defined a third region called the ambiguous region. It is illustrated by the dashed blue lines in Figure 3.3 and has a thickness according to the errors of the photometric colors in each redshift bin. Our classification is as follows: galaxies above the ambiguous region are, most likely, passive, and below are star-forming. In the middle, we can have both quiescent and star-forming galaxies, but also galaxies that are migrating from star-forming to passive. The main reason for creating this new region is to have a clear distinction between red and blue galaxies and to not have contamination in the regions

Once those were defined, we computed the number of sources that lay in the different regions, represented by Table 3.1.

Table 3.1: Number and respective percentage of QSG, AMG and SFG of COSMOS2020 for each redshift bin and of the total sample. The mean standard deviation is also shown in each column.

z-Bin	QSG, σ = 2.66%	AMG, σ = 0.56%	SFG, σ = 2.71%	Total Galaxies
0.5 - 1.0	6166 (7.17%)	3260 (3.79%)	76540 (89.04%)	85966
1.0 - 1.5	3671 (5.61%)	1938 (2.96%)	59860 (91.43%)	65469
1.5 - 2.0	1459 (4.01%)	1420 (3.91%)	33461 (92.08%)	36340
2.0 - 2.5	322 (1.13%)	1226 (4.30%)	26959 (94.57%)	28507
2.5 - 3.0	139 (0.64%)	850 (3.90%)	20826 (95.47%)	21815
3.0 - 3.5	18 (0.16%)	305 (2.72%)	10887 (97.12%)	11210
0.5 - 3.5	11775 (4.72%)	8999 (3.61%)	228533 (91.67%)	249307

From Table 3.1, the percentage of AMG stays between 3 and 4%, over cosmic time, which can be misleading because it does not mean the migration rate is constant; not only is the typical photometric errors of the colors larger (so the region also gets larger), but the percentage of QSG changes drastically, from 0.16% to ∼7% in $0.5 < z < 3.5$ and from ∼1% to ∼4% in just one redshift bin, $2.0 < z < 2.5$ to $1.5 < z < 2.0$. We note that these redshift bins coincide with the peak of SF activity in the universe when it was 3-6 Gyr old (Madau and Dickinson [2014]). For the percentage of QSG to increase and for the AMG to maintain more or less stable, then the percentage of SFG must decrease as the redshift

decreases. So, according to the classification we imposed, the full sample has 4.72% of passive galaxies, 3.61% of ambiguous galaxies, and 91.67% of star-forming galaxies.

Tables 3.2, 3.3, 3.4 and 3.5 show the medians of the SFR, stellar mass, and sSFR for the quiescent, ambiguous, and star-forming galaxies in each redshift bin, as well as, for the total sample. These values are summarized in Figure 3.4 and Figure 3.5.

Table 3.2: Number and respective percentage, the mean log SFR, stellar mass, and sSFR of COSMOS2020 QSG for each redshift bin and for the whole sample. The typical standard deviation of these galaxies is also shown in the second column.

z-Bin	QSG	log (SFR/[$M_\odot$ yr^{-1}])			log (M_*/[$M_\odot$])			log (sSFR/[yr^{-1}])		
	σ =2.66%	16th	50th	84th	16th	50th	84th	16th	50th	84th
0.5 - 1.0	6166 (7.17%)	-1.58	-0.28	0.62	9.22	10.46	11.02	-12.14	-10.47	-9.74
1.0 - 1.5	3671 (5.61%)	-2.16	-0.04	1.03	10.21	10.75	11.14	-13.09	-10.67	-9.63
1.5 - 2.0	1459 (4.01%)	-1.72	0.52	1.52	10.47	10.90	11.22	-12.94	-10.36	-9.26
2.0 - 2.5	322 (1.13%)	-1.67	-0.47	1.50	10.64	10.99	11.30	-12.82	-11.49	-9.47
2.5 - 3.0	139 (0.64%)	-1.37	-0.21	1.61	10.75	11.01	11.24	-12.69	-11.23	-9.30
3.0 - 3.5	18 (0.16%)	-1.58	-0.28	1.70	10.50	10.99	11.13	-12.69	-11.30	-8.77
0.5 - 3.5	11775 (4.72%)	-1.81	-0.16	0.90	9.72	10.67	11.11	-12.48	-10.54	-9.64

Table 3.3: Number and respective percentage, the mean log SFR, stellar mass and sSFR of COSMOS2020 AMG for each redshift bin and for the whole sample. The typical standard deviation of these galaxies is also shown in the second column.

z-Bin	AMG	log (SFR/[$M_\odot$ yr^{-1}])			log (M_*/[$M_\odot$])			log (sSFR/[yr^{-1}])		
	σ =0.56%	16th	50th	84th	16th	50th	84th	16th	50th	84th
0.5 - 1.0	3260 (3.79%)	-0.84	0.14	0.77	9.10	10.04	10.84	-10.53	-9.93	-9.36
1.0 - 1.5	1938 (2.96%)	-0.40	0.65	1.37	9.76	10.49	11.01	-10.56	-9.83	-9.15
1.5 - 2.0	1420 (3.91%)	0.02	1.17	1.73	10.23	10.70	11.13	-10.58	-9.50	-8.90
2.0 - 2.5	1226 (4.30%)	-0.32	1.32	1.91	10.39	10.78	11.14	-11.00	-9.45	-8.85
2.5 - 3.0	850 (3.90%)	-0.39	1.35	1.98	10.43	10.82	11.14	-11.18	-9.50	-8.69
3.0 - 3.5	305 (2.72%)	-0.04	1.54	2.23	10.41	10.74	11.11	-10.86	-9.20	-8.37
0.5 - 3.5	8999 (3.61%)	-0.57	0.62	1.59	9.62	10.54	11.04	-10.63	-9.76	-9.04

In the figures 3.4 and 3.5, the bottom and the top vertical lines correspond to the 16th and 84th percentile of that group of galaxies, respectively. Here we can visually see that the stellar mass decreases as the redshift decreases, which is characteristic of a flux-limited sample. Regarding the SFR, all types of galaxies decrease their SFR gradually except for the quiescent galaxies, verified by the percentiles of the tables and shown in Figure 3.4. There is a slight increase in SFR between the redshift bins $1.5 < z < 2.0$ and $2.0 < z < 2.5$ for the quiescent, which can happen due to the flux-limited sample, however, the percentiles are quite large. The sSFR behaves approximately in the same way. We can also visually see the large errors of SFR and, as a consequence, of sSFR of QSG and the decrease of stellar mass in all types of galaxies. Here we can see that the AMG behave according to the QSG in terms of stellar mass and according to SFG in terms of SFR.

Table 3.4: Number and respective percentage, the mean log SFR, stellar mass and sSFR of COSMOS2020 SFG for each redshift bin and for the whole sample. The typical standard deviation of these galaxies is also shown in the second column.

z-Bin	SFG	log (SFR/[$M_\odot$ yr^{-1}])			log (M_*/[$M_\odot$])			log (sSFR/[yr^{-1}])		
	σ =2.71%	16th	50th	84th	16th	50th	84th	16th	50th	84th
0.5 - 1.0	76540 (89.04%)	-0.65	-0.05	0.66	8.63	9.14	10.02	-9.66	-9.29	-8.93
1.0 - 1.5	59860 (91.43%)	-0.10	0.51	1.11	8.91	9.48	10.31	-9.50	-9.11	-8.55
1.5 - 2.0	33461 (92.08%)	0.42	1.00	1.56	9.14	9.72	10.47	-9.24	-8.81	-8.27
2.0 - 2.5	26959 (94.57%)	0.38	1.01	1.63	9.35	9.87	10.48	-9.32	-8.92	-8.42
2.5 - 3.0	20826 (95.47%)	0.69	1.23	1.71	9.30	9.84	10.48	-9.31	-8.62	-8.03
3.0 - 3.5	10887 (97.12%)	0.68	1.27	1.73	9.42	9.93	10.53	-9.38	-8.71	-8.02
0.5 - 3.5	228533 (91.67%)	-0.25	0.59	1.34	8.89	9.54	10.34	-9.51	-9.08	-8.47

Table 3.5: Number, mean log SFR, stellar mass, and sSFR of COSMOS2020 galaxies for each redshift bin and for the whole sample.

z-Bin	Total	log (SFR/[$M_\odot$ yr^{-1}])			log (M_*/[$M_\odot$])			log (sSFR/[yr^{-1}])		
		16th	50th	84th	16th	50th	84th	16th	50th	84th
0.5 - 1.0	85966	-0.70	-0.05	0.66	8.66	9.21	10.24	-9.82	-9.34	-8.96
1.0 - 1.5	65469	-0.16	0.50	1.12	8.93	9.55	10.48	-9.61	-9.15	-8.59
1.5 - 2.0	36340	0.38	1.00	1.57	9.17	9.79	10.62	-9.33	-8.85	-8.30
2.0 - 2.5	28507	0.36	1.01	1.65	9.36	9.91	10.58	-9.37	-8.94	-8.44
2.5 - 3.0	21815	0.65	1.23	1.72	9.31	9.88	10.57	-9.36	-8.66	-8.05
3.0 - 3.5	11210	0.67	1.27	1.74	9.42	9.96	10.57	-9.40	-8.72	-8.03
0.5 - 3.5	249307	-0.31	0.57	1.34	8.91	9.60	10.47	-9.62	-9.12	-8.51

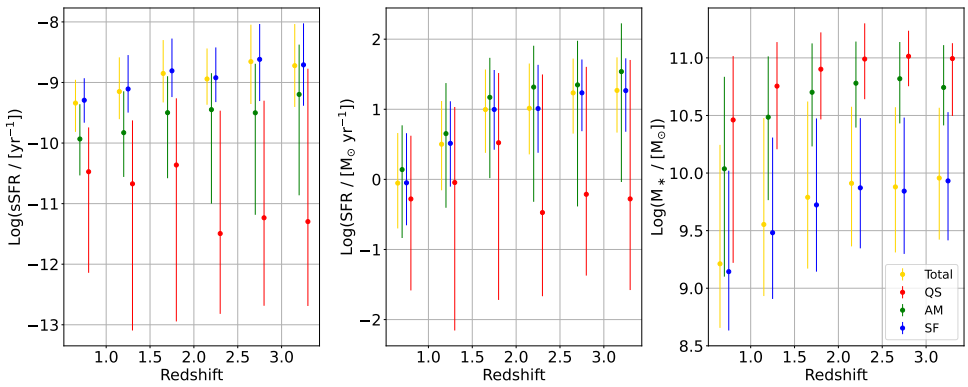

Figure 3.4: Mean log sSFR, SFR, and stellar mass for each type of galaxy. The points were shifted for better visualization and the typical errors correspond to the 16th and 84th percentile of each group of galaxies, respectively.

Figure 3.5 has an addition of a scatter plot for each type of galaxy to check how the medians behave according to the limits of these quantities. We investigated the ”steps” seen in the sSFR plot for QSG and concluded that they are from galaxies with low sSFR and high stellar mass. This figure also gives

us information about the spread of spurious data in our sample. The QSG have a higher spread of data in both SFR and stellar mass whereas the SFG are more compact, especially in terms of SFR. We can also see the mass completeness cut in the SF galaxies (and the total) that we did in Chapter 2.

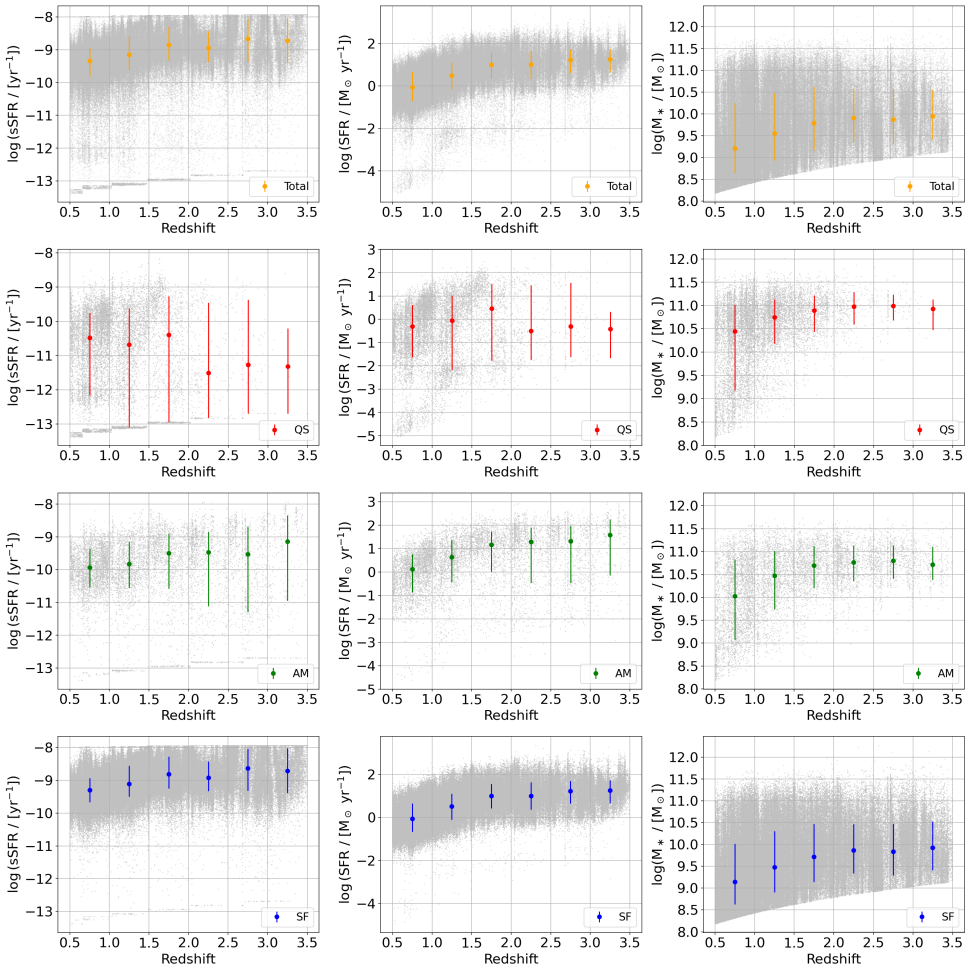

Figure 3.5: Mean log sSFR, SFR, and stellar mass for each type of galaxy. In grey is a scatter plot of each galaxy type. The typical errors correspond to the 16th and 84th percentile of each group of galaxies, respectively.

Given that the volume covered by the adopted redshift bins is not the same —volume does not scale linearly with redshift—, we decided to calculate and study the source density. Figure 3.6 shows the change of this source density as a function of redshift —number of sources divided by the volume in a redshift bin in Mpc^3— of the total sample and of each type of galaxy. By checking the literature, we can say that the number density of the sample is consistent with the one computed by Weaver et al. [2022a] (Figure 8) —their points are also plotted in Figure 3.6. At $1.5 < z < 2.0$, the number densities of ambiguous and passive galaxies become pretty similar and the passive one increases ~ 1 dex from that to $0.5 < z < 1.0$, while the ambiguous number density becomes 0.5 dex lower than the passive one. The number density of the passive galaxies increases more steeply than the ambiguous when we go to lower redshift. In other words, the number density of quiescent galaxies is higher at low redshift and lower at high redshift when compared to the number density of ambiguous galaxies.

The star-forming number density is compatible with Weaver et al. [2022a] taking into account that the star-forming galaxies of the sample are weighted by low-mass galaxies as we will see later in the 3D-UVJ diagram. The star-forming and ambiguous galaxies have a steeper end in the last redshift bin, $3.0 < z < 3.5$, which may be due to the magnitude limit of the survey and they are also more prone to

errors in high redshift. The magnitude limit of the survey does not seem to influence the number density of passive galaxies as these types of galaxies are more massive.

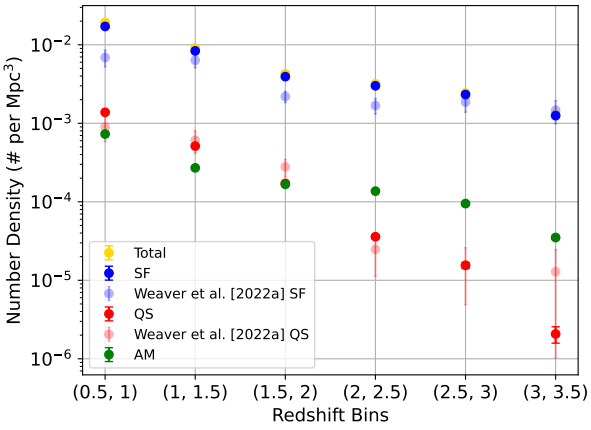

Figure 3.6: Number density for the different types of galaxies and for the total sample of COSMOS2020 as a function of redshift bins. The error bars are calculated by taking the square root of the number of galaxies in each bin.

3.1.1 Evolution of the Physical Properties of Galaxies at 0.5 < z < 3.5

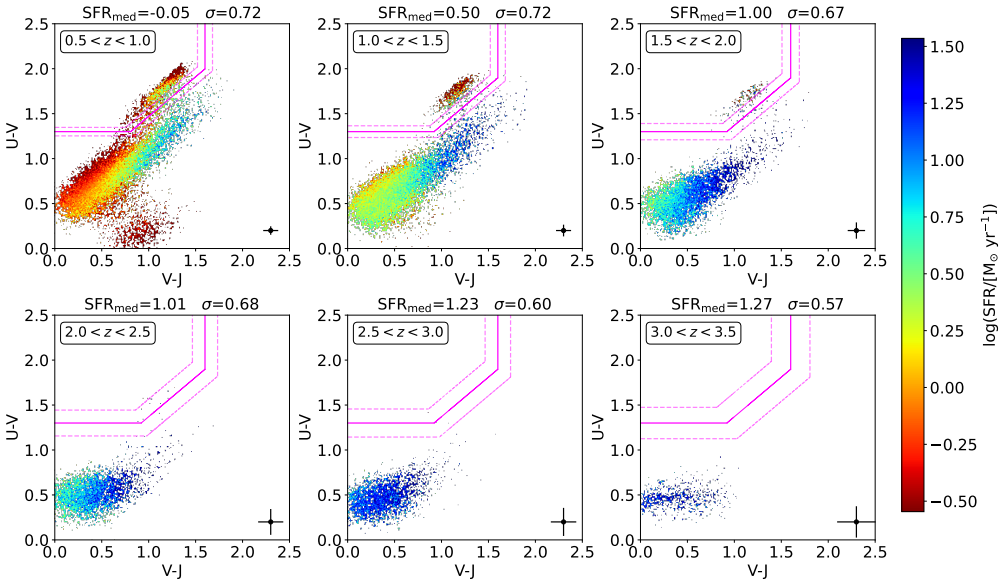

Figure 3.7: UVJ diagram divided into six 0.5 redshift bins and colored according to the SFR of the total sample, which is reported by the colorbar on the right side of the Figure. The pink continuous line is taken from Williams et al. [2009], and the dashed lines are plotted according to the typical photometric errors of the population in each redshift bin and shown as a cross on the lower right side of each panel.

Figure 3.7 illustrates the distribution of SFR across different redshift bins in the 3D-UVJ diagrams. As expected, lower redshift bins exhibit lower SFR values, while higher redshift bins display higher SFR values, consistent with the decline in the cosmic star formation rate until $z \sim 2$. However, the SFR introduces a bias in these plots. In the lowest redshift bin ($0.5 < z < 1.0$), some star-forming galaxies exhibit SFR values comparable to those of quiescent galaxies. This overlap can be misleading, as it becomes difficult to distinguish between star-forming and quiescent galaxies based solely on their SFR.

This issue arises because the SFR does not account for the stellar mass of a galaxy. For instance, two galaxies of different masses — one more massive and one less massive — could exhibit the same SFR in absolute terms. However, producing a given SFR, such as 5 $M_\odot$/yr, has different implications depending on the overall mass of the galaxy. In a star-forming galaxy — usually less massive —, such an SFR may be indicative of ongoing significant star formation, whereas in a quiescent galaxy — usually more massive —, it may represent a residual level of star formation that does not significantly impact its evolutionary state.

Figure 3.8 represents the SFR histogram for the three galaxy types in different redshift bins. We can see a clear distinction between the SFG (blue) and QSG (red), especially after $z = 1.0$. The SFR increases with redshift as we have seen before. The SFR of the AMG (green) stays approximately the same over cosmic time. Therefore, we can conclude that the SFR alone is not good enough to distinguish star-forming from passive galaxies; we need more parameters to classify and analyze the sample. So, to remove this bias, we need to normalize for the stellar mass.

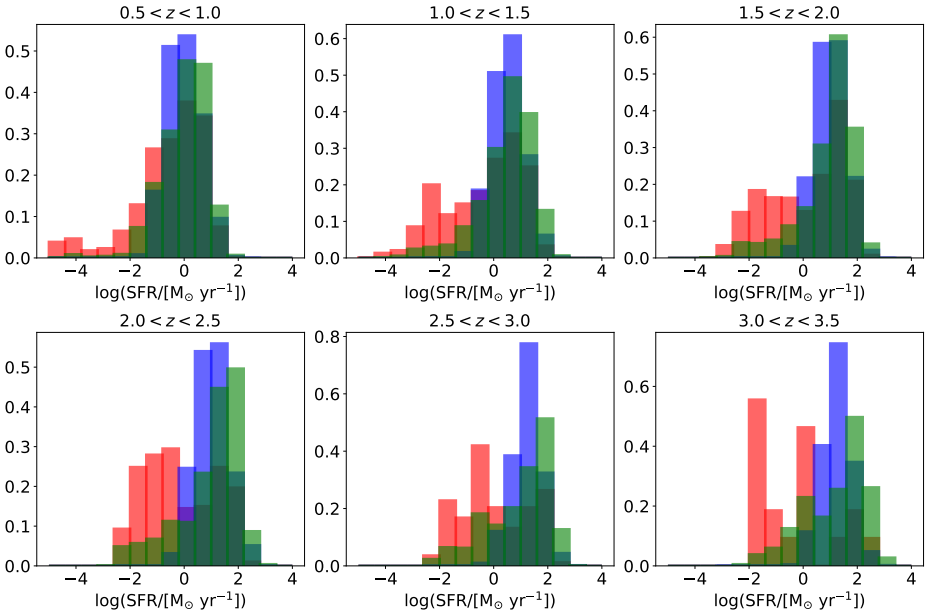

Figure 3.8: SFR histogram in each redshift bin for the different types of galaxies. Red corresponds to QSG, blue to SFG, and green to AMG. The y-axis corresponds to a probability density where each bin raw count is divided by the total number of counts and the bin width so that the area under the histogram is equal to 1.

The distribution of the total stellar mass of the galaxies in the UVJ is illustrated in Figure 3.9. As expected, the most massive galaxies are very red in $V - J$ ($V - J > 1$ approximately), indicating that the sample contains genuine passive galaxies and galaxies with dusty starbursts —filled with a large amount of dust that obscures the galaxy and makes them massive. The $U - V$ discriminates and is able to distinguish between these two families: the passive galaxies are redder in the $U - V$ while the dust-obscured systems are not as red, which puts them in the star-forming region. Blue objects in the lower left corner have a lower mass, as they might be younger systems that are still forming stars, making these galaxies less massive.

There is a cloud of faint, low-mass galaxies at $U - V \sim 0.2$ and $V - J \sim 0.9$ that can only be detected in the first redshift bin (low redshifts), thus why they do not appear in the others.

By analyzing the histogram of the stellar mass in Figure 3.10 we can see an accentuated bimodality between star-forming and quiescent galaxies. Star-forming galaxies, on one hand, have a lower stellar

mass than passive galaxies while ambiguous galaxies are located in the middle between these two types of galaxies. The ambiguous galaxies tend to go slightly towards the more massive galaxies when the redshift increases because the region is bigger at those redshifts.

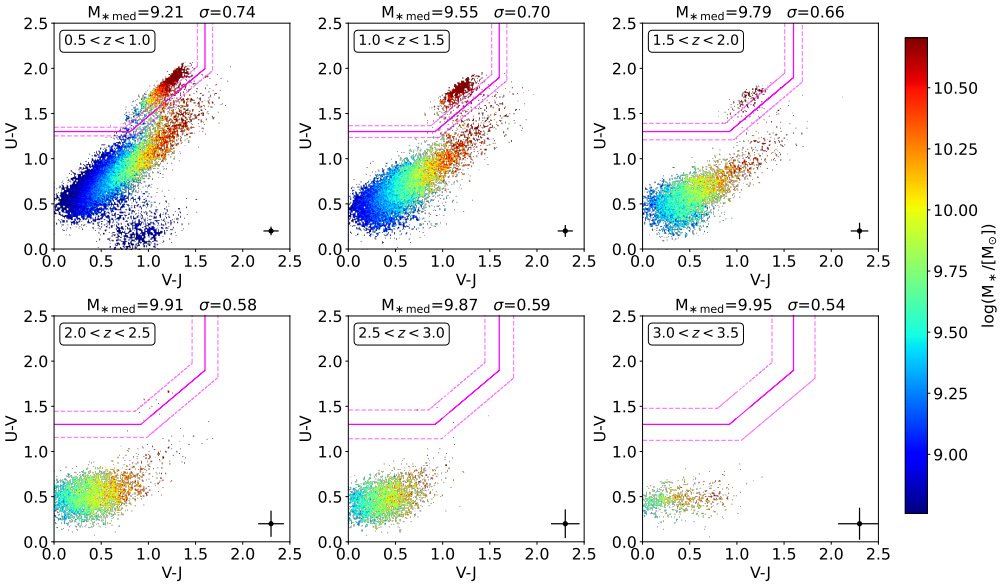

Figure 3.9: UVJ diagram divided into six 0.5 redshift bins and colored according to the stellar mass of the galaxies of the total sample, which is reported by the colorbar on the right side of the Figure. The pink continuous line is taken from Williams et al. [2009], and the dashed lines are plotted according to the typical photometric errors of the population in each redshift bin and shown as a cross on the lower right side of each panel.

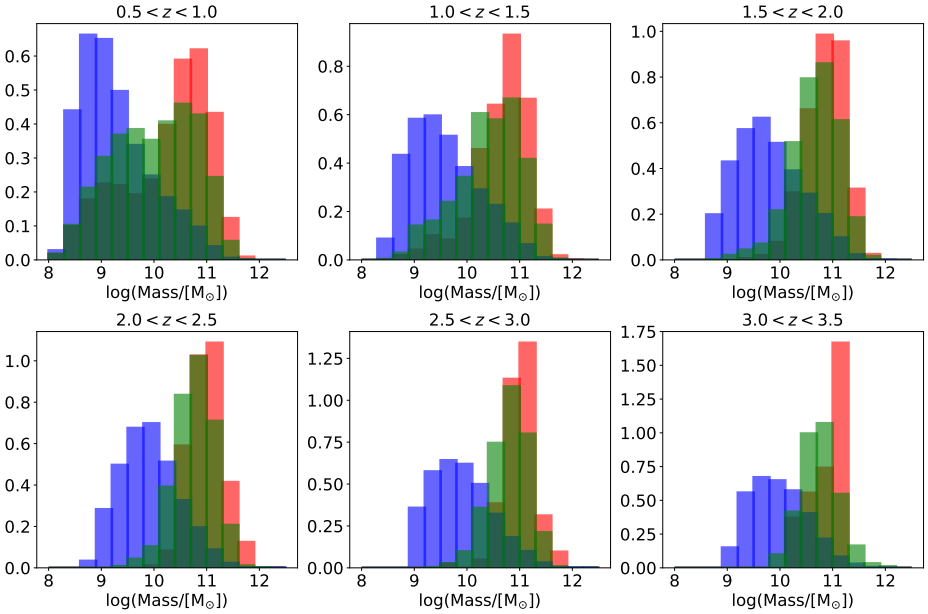

Figure 3.10: Stellar mass histogram in each redshift bin for the different types of galaxies. Red corresponds to QSG, blue to SFG, and green to AMG. The y-axis corresponds to a probability density where each bin raw count is divided by the total number of counts and the bin width so that the area under the histogram is equal to 1.

Now that we have seen the stellar mass and the SFR distribution in the UVJ diagram, we can now analyze the sSFR, which is the SFR divided by the stellar mass. This is illustrated in Figure 3.11. There

is a clear and accentuated dichotomy between these two types of galaxies: the passive galaxies with low sSFR, in red, and the star-forming galaxies with high sSFR, in blue. When the redshift increases so does the sSFR and vice versa. There are also star-forming galaxies that have a low sSFR along the diagonal where dust content in galaxies increases, i.e. from the lower left to the upper right in the UVJ diagram.

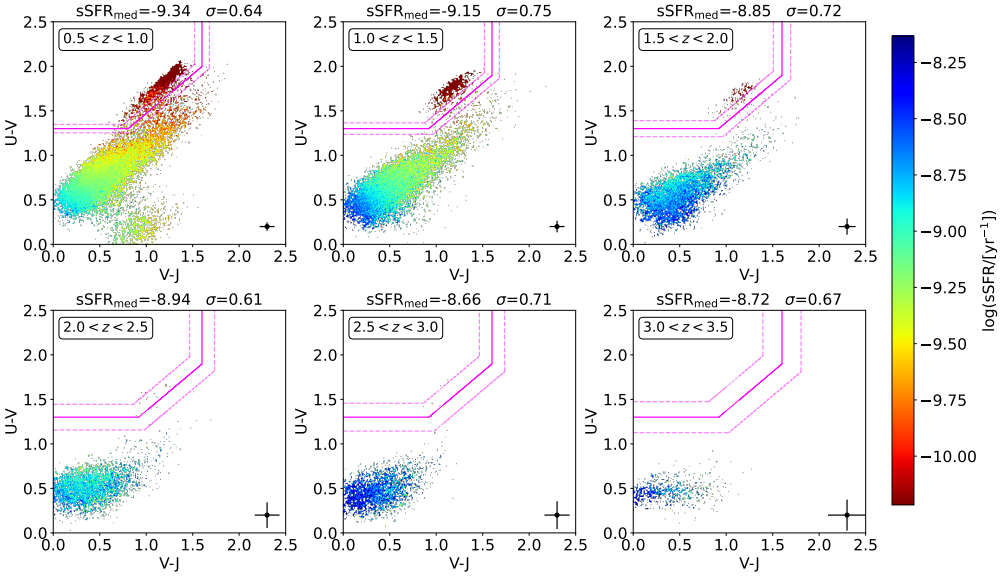

Figure 3.11: UVJ diagram divided into six 0.5 redshift bins and colored according to the sSFR of the total sample, which is reported by the colorbar on the right side of the Figure. The pink continuous line is taken from Williams et al. [2009], and the dashed lines are plotted according to the typical photometric errors of the population in each redshift bin and shown as a cross on the lower right side of each panel.

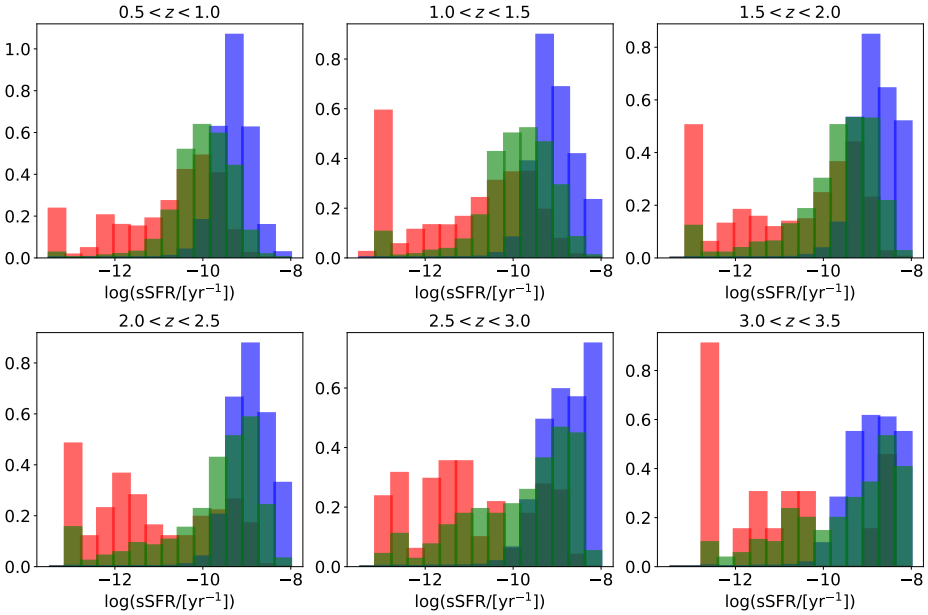

Figure 3.12: sSFR histogram in each redshift bin for the different types of galaxies. Red corresponds to passive galaxies, blue to star-forming galaxies, and green to ambiguous galaxies. The y-axis corresponds to a probability density where each bin raw count is divided by the total number of counts and the bin width so that the area under the histogram is equal to 1.

The sSFR histogram in Figure 3.12 shows the clear division between the QSG with a low sSFR and

the SFG with a high sSFR. The AMG shows a distribution over all values. When the redshift increases so does the minimum sSFR of each redshift bin; this happens because the survey is flux-limited and is not able to detect galaxies with low sSFR at high redshifts.

Analyzing both Figure 3.13 and 3.14 that show the mass-to-light ratio and the light-weighted age in the V-band, respectively, we can conclude that passive galaxies and dust-obscured systems have a high mass-to-light ratio and a high light-weighted age.

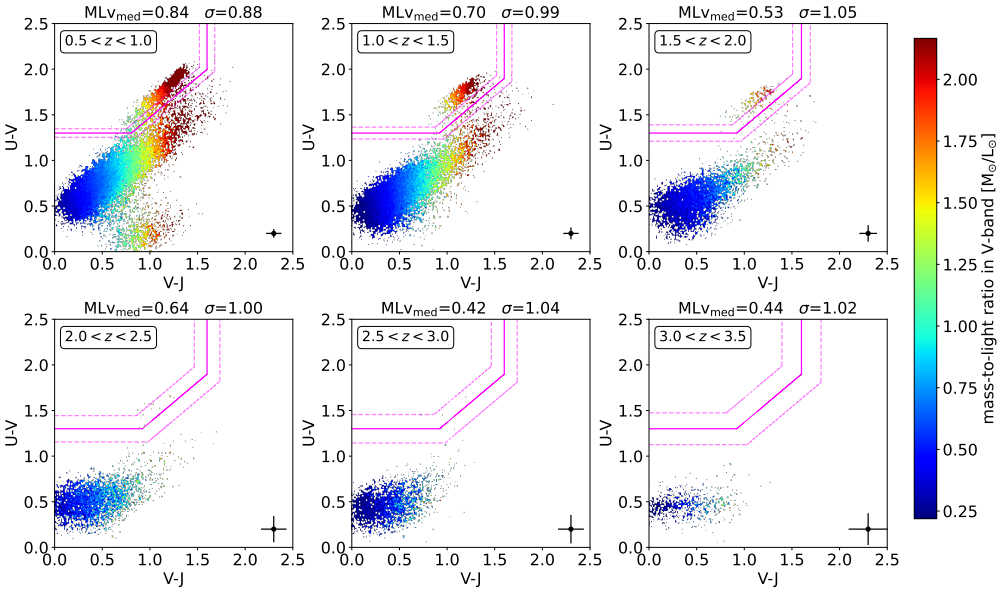

Figure 3.13: UVJ diagram divided into six 0.5 redshift bins and colored according to the mass-to-light ratio of the total sample, which is reported by the colorbar on the right side of the Figure. The pink continuous line is taken from Williams et al. [2009], and the dashed lines are plotted according to the typical photometric errors of the population in each redshift bin and shown as a cross on the lower right side of each panel.

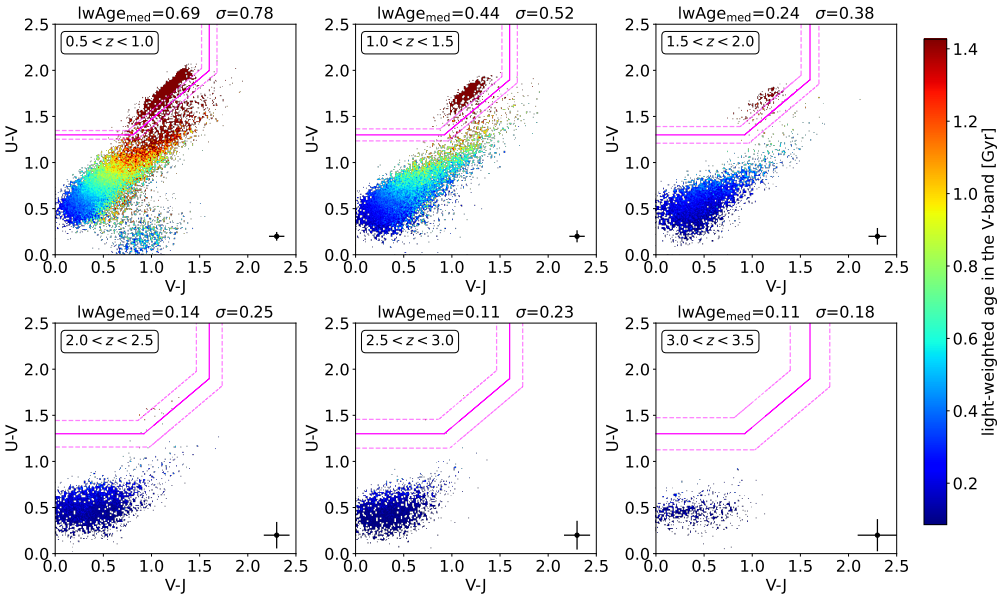

Figure 3.14: UVJ diagram divided into six 0.5 redshift bins and colored according to the light-weighted age of the total sample, which is reported by the colorbar on the right side of the Figure. The pink continuous line is taken from Williams et al. [2009], and the dashed lines are plotted according to the typical photometric errors of the population in each redshift bin and shown as a cross on the lower right side of each panel.

A high mass-to-light ratio and a high light-weighted age indicate that the galaxies are massive systems whose stellar populations are very old or obscured by dust, i.e. the galaxies have already evolved.

Star-forming galaxies located in the lower left corner of the UVJ diagram have a low mass-to-light ratio and a low light-weighted age; these galaxies have yet to evolve and so their stellar populations are constituted of very luminous and young stars. Since these are young galaxies (<2 Gyr old) they have low stellar masses.

These plots also show a slightly perpendicular pattern along the diagonal where dust content in galaxies increases. This pattern may be due to the SED fitting when the galaxies are put in their best-fit templates.

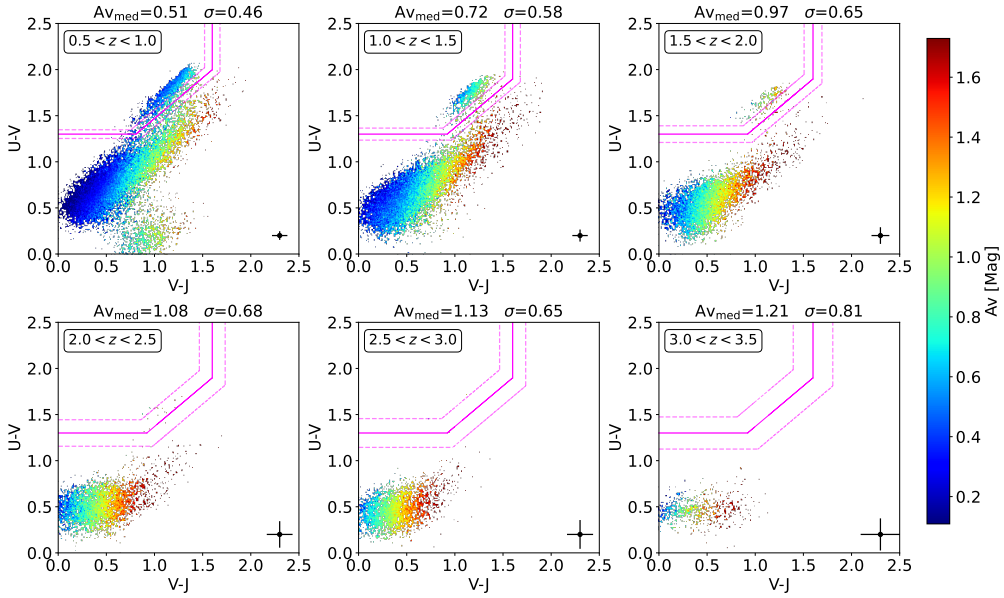

Figure 3.15: UVJ diagram divided into six 0.5 redshift bins and colored according to the A_V of the total sample, which is reported by the colorbar on the right side of the Figure. The pink continuous line is taken from Williams et al. [2009], and the dashed lines are plotted according to the typical photometric errors of the population in each redshift bin and shown as a cross on the lower right side of each panel.

Finally, let us analyze how A_V and LIR $(8 - 1000\mu m)$ is distributed in the UVJ diagram, Figure 3.15 and Figure 3.16, respectively. These two quantities correlate with each other since dust emits in the infrared and is what causes obscuration in a galaxy —or a galaxy to have high extinction. Therefore, both plots are very similar to each other.

Passive galaxies and very blue star-forming galaxies are not highly extinct, according to Figure 3.15. Thus, these galaxies have a relatively low LIR, Figure 3.16, namely the blue star-forming ones at low redshifts.

These plots also confirm that the infrared luminosity is a star formation tracer, which is already known (see Madau and Dickinson [2014]). This physical process consists of ionizing photons created by young stellar populations that are absorbed by the dust that heats up and re-emits in the infrared through black body radiation. It is more evident in the past because the further we go back in time the larger the fraction of galaxies having star formation happening under larger columns of dust. In rough terms, this dust is cleared by SN and AGN as time passes by.

Figure 3.17 shows the histograms of the LIR of the total sample (grey) and of the redshift bin (blue). The LIR of the total sample is weighted down by the large number of sources in the first redshift bins —its shape and intensity are mostly influenced by the first two redshift bins. Just like in the UVJ, Figure

3.16, it is now more clear that the mean LIR of the sample increases with the redshift.

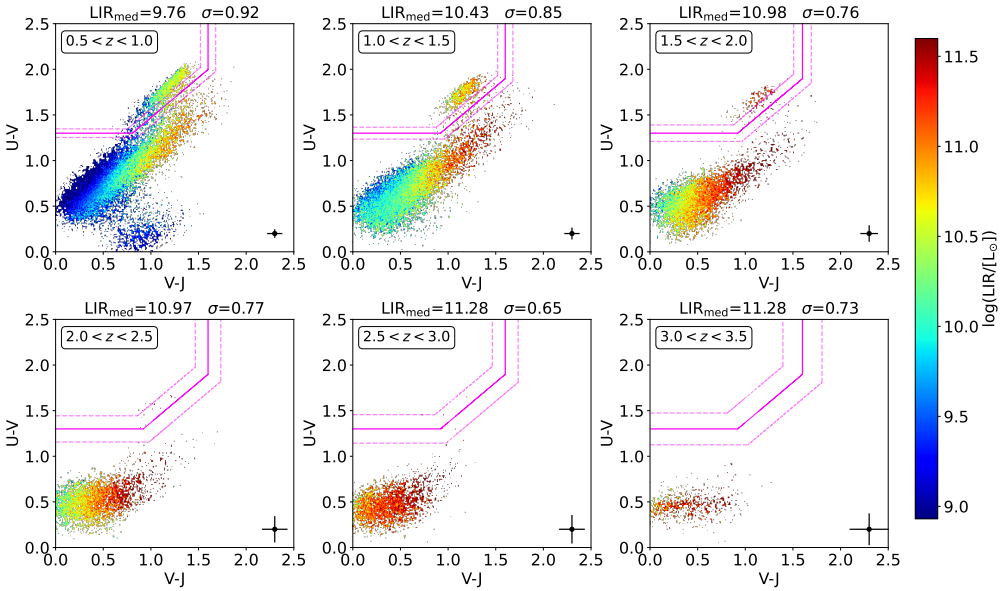

Figure 3.16: UVJ diagram divided into six 0.5 redshift bins and colored according to the LIR of the total sample, which is reported by the colorbar on the right side of the Figure. The pink continuous line is taken from Williams et al. [2009], and the dashed lines are plotted according to the typical photometric errors of the population in each redshift bin and shown as a cross on the lower right side of each panel.

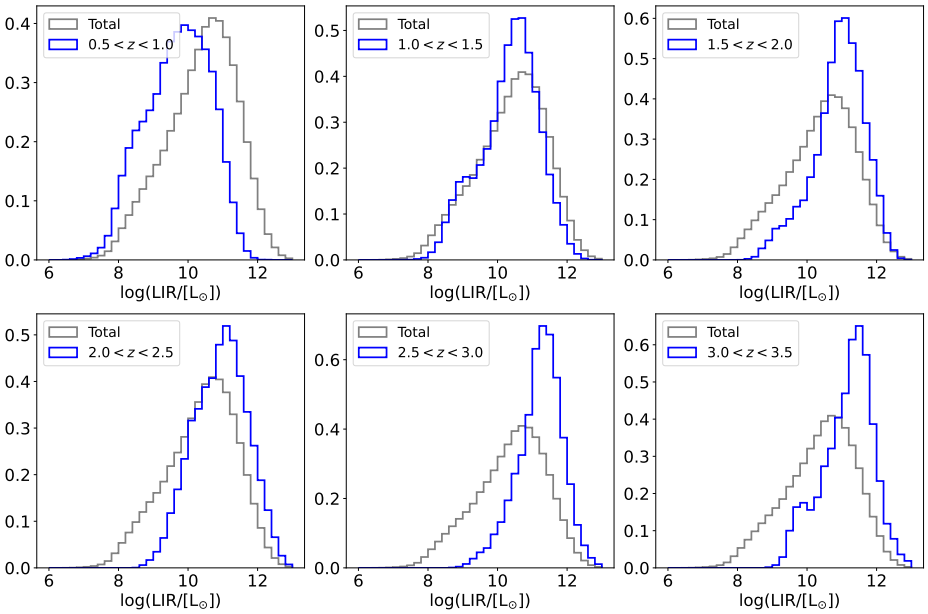

Figure 3.17: Histogram comparing the LIR of the total sample (grey) and the LIR in each redshift bin (blue).

It is also important to check the histograms of the infrared luminosity of the different types of galaxies. Figure 3.18 represents the infrared luminosity of the total sample (grey) like before, but now we have the infrared luminosity of the SFG (blue) and of the QSG (red) of each redshift bin. The LIR of the passive galaxies is more luminous, and not as spread out, when compared to the star-forming ones as they are, usually, more massive.

The peak of the infrared luminosity of the passive galaxies stays approximately between $10 <$

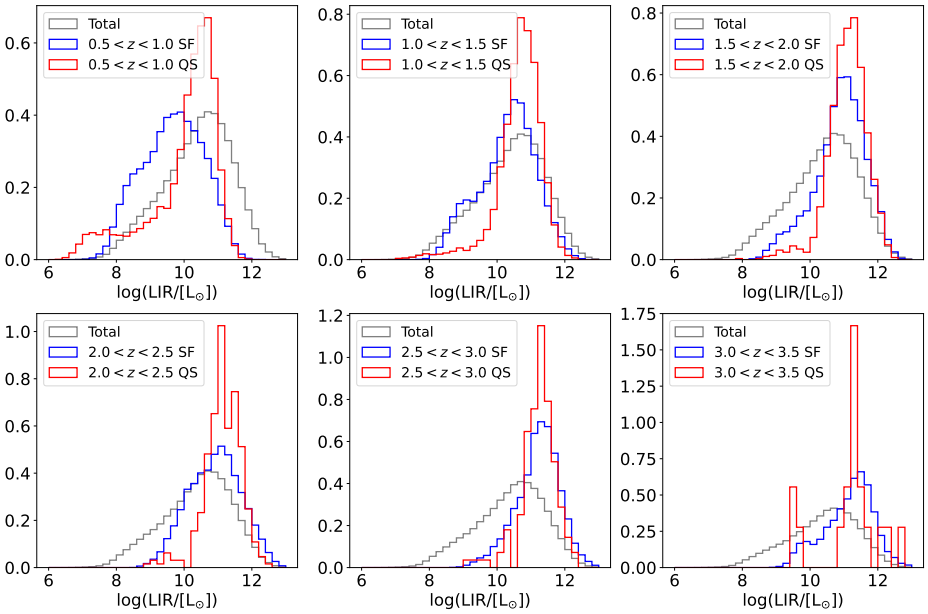

Figure 3.18: Histogram comparing the LIR of the total sample (grey) and the LIR in each redshift bin for QSG (red) and SFG (blue).

$\log(\mathrm{LIR}/[\mathrm{L}_\odot]) < 12$ while the LIR of the star-forming moves from low to high LIR. This happens because, while passive galaxies have a low or even absent dust content, they do not have the star formation to heat this dust and for it to emit at these wavelengths, which is in contrast with star-forming galaxies that can heat the dust. As confirmed also by Figure 3.15, galaxies at high redshift have higher extinction, which indicates they have more dust and a higher infrared luminosity.

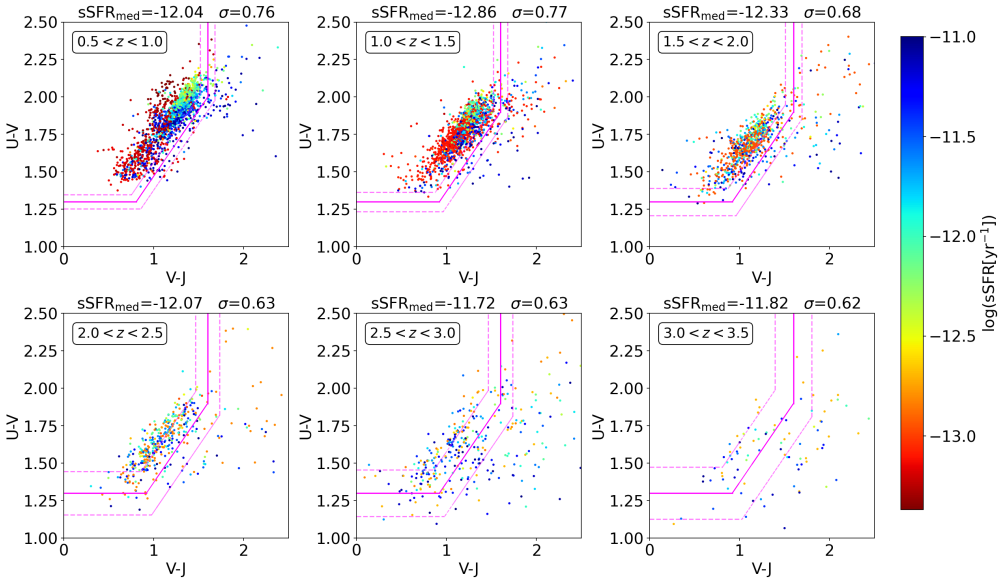

Figure 3.19: UVJ diagram divided into six 0.5 redshift bins and colored according to $\log(\mathrm{sSFR}\,/\,[\mathrm{yr}^{-1}]) < -11$ of the total sample, which is reported by the colorbar on the right side of the Figure. The pink continuous line is taken from Williams et al. [2009], and the dashed lines are plotted according to the typical photometric errors of the population in each redshift bin and shown as a cross on the lower right side of each panel.

Before moving forward to the sample analysis divided into different bins of 1 Gyr, instead of z-bins, let us see how the sample behaves if, instead of discriminating star-forming galaxies from passive galaxies

by color, we differentiate them by sSFR in different redshift bins. We defined three intervals based on the typical sSFR values these galaxies have: galaxies with $\log(\text{sSFR}/[\text{yr}^{-1}]) < -11$ are considered QSG, $\log(\text{sSFR}/[\text{yr}^{-1}]) > -9$ are SFG, and, in between, we have the AMG to make sure we have a clean sample of star-forming and quiescent galaxies. These plots are zoomed-in in the passive region to understand if there are any obvious patterns of the three types of galaxies regarding the sSFR.

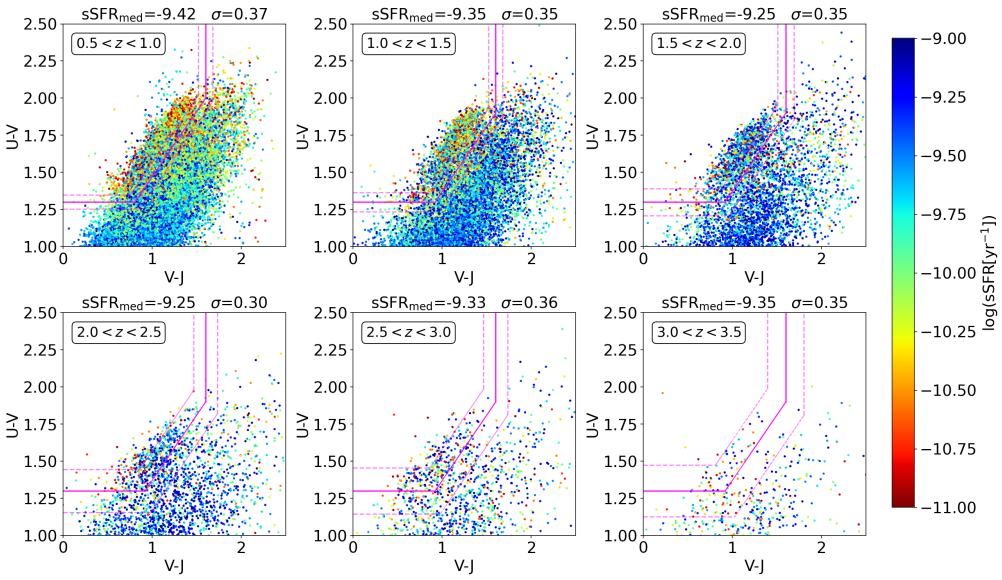

Figure 3.20: UVJ diagram divided into six 0.5 redshift bins and colored according to $-11 < \log(\text{sSFR}/[\text{yr}^{-1}]) < -9$ of the total sample, which is reported by the colorbar on the right side of the Figure. The pink continuous line is taken from Williams et al. [2009], and the dashed lines are plotted according to the typical photometric errors of the population in each redshift bin and shown as a cross on the lower right side of each panel.

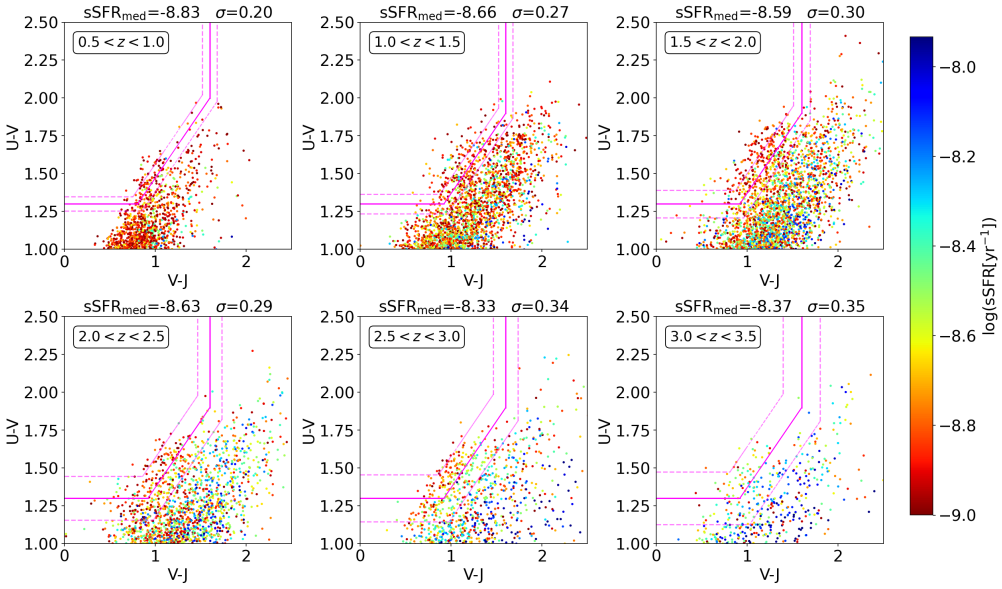

Figure 3.21: UVJ diagram divided into six 0.5 redshift bins and colored according to $\log(\text{sSFR}/[\text{yr}^{-1}]) > -9$ of the total sample, which is reported by the colorbar on the right side of the Figure. The pink continuous line is taken from Williams et al. [2009], and the dashed lines are plotted according to the typical photometric errors of the population in each redshift bin and shown as a cross on the lower right side of each panel.

Figure 3.19 shows the scatter plot of the sample distribution with $\log(\text{sSFR}/[\text{yr}^{-1}]) < -11$ in the UVJ diagram. This figure demonstrates that most galaxies with this sSFR are either inside the passive or inside the ambiguous region we defined previously. However, some galaxies are still found in the star-forming region. These sources are located in the top right corner at low redshifts, and, as the redshift increases, they move to the bottom.

Figure 3.20 shows the scatter plot of the sample distribution with $-11 < \log(\text{sSFR}/[\text{yr}^{-1}]) < -9$ in the UVJ diagram. The sources are located in the three regions; galaxies with lower sSFR are concentrated in the passive region (red) and galaxies with higher sSFR are concentrated in the star-forming region (blue). As the redshift decreases, galaxies start to appear more in the passive region.

Finally, Figure 3.21 has sources with $\log(\text{sSFR}/[\text{yr}^{-1}]) > -9$. These galaxies are mainly located in the star-forming region we previously defined.

3.2 Subsamples Divided into Gyr Bins

The accelerated expansion of the universe makes redshift a quantity that is not linear. This means that the time elapsed by two pairs of redshift is not the same. For instance, at redshift 0.5 and 1.0, the age of the universe is 8.42 and 5.75 Gyr, respectively, while at redshift 1.5 is 4.20 Gyr. Clearly, the difference between the pairs of redshift, $0.5 - 1.0$ and $1.0 - 1.5$, is not the same. Therefore, it is important to not only analyze the sample using subsamples of redshift bins but also using subsamples of time. In our case, we will be using subsamples of Gyr bins to be able to study the migration of galaxies between the two clouds more linearly.

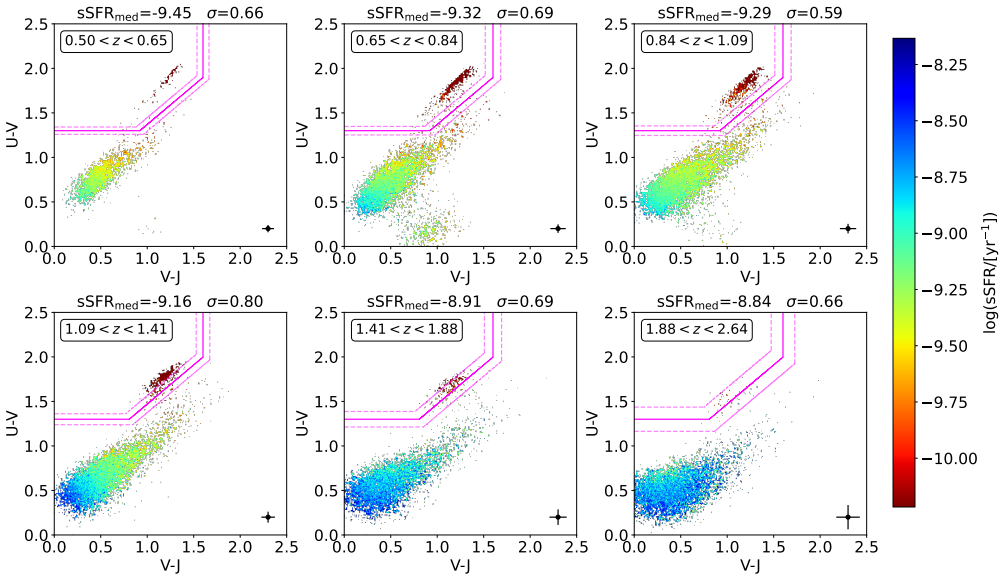

Figure 3.22: UVJ diagram divided into six 1 Gyr bins until $z < 2.64$. The plots are colored according to the sSFR of the total sample, which is reported by the colorbar on the right side of the Figure. The pink continuous line is taken from Williams et al. [2009], and the dashed lines are plotted according to the typical photometric errors of the population in each redshift bin and shown as a cross on the lower right side of each panel.

We started analyzing subsamples of 1 Gyr bins from redshift 0.50 to redshift 2.64. The redshift limit of 2.64 was chosen so that the next bin did not go beyond the maximum redshift of the sample which is 3.5. Let us jump to the sSFR distribution in the UVJ diagram, Figure 3.22. When compared to Figure 3.11, the Gyr subsample is distributed more linearly —the increase of passive galaxies in the red cloud

gradually increases over time. The decrease in sSFR when we travel back to the present is also smoother and not as accentuated as the subsamples in redshift bins. As we will see in Table 3.6, the first Gyr bin is not as densely populated as the others, this is mainly due to the fact that the COSMOS deep field is conceived for high redshift studies. If we had more galaxies at low redshifts than at high ones it would present a problem for this study. We would not be able to study the quenching timescale as many galaxies at low redshifts have already stopped their star formation and migrated to the passive region, which once again highlights that COSMOS is a good observational dataset for our study. Of course, the volume elapsed in each Gyr bin also plays a role in this density; for instance, the first bin has ~ 27 Gpc^3, ~ 47 Gpc^3 on the second and ~ 81 Gpc^3 on the third.

Table 3.6 represents the number of galaxies in each region using the same conditions as before. Both passive galaxies and star-forming galaxies gradually increase and decrease, respectively, when we travel to lower redshifts. Once again, the percentage of ambiguous galaxies stays more or less constant, between $\sim$3% and $\sim$4%. However, the standard deviation of these galaxies decreases from 0.56% in Table 3.1 to 0.36% in Table 3.6. A change in the standard deviation of the ambiguous galaxies might be indirectly correlated to the timescale they have in that stage —the timescale it takes for a galaxy to migrate from star-forming to red passive. This discussion is present at the end of Section 3.2 since other subsamples of Gyr bins need to be tested.

Table 3.6: Number and respective percentage of QSG, AMG, and SFG of COSMOS2020 per time interval in Gyr and of the total sample. The mean standard deviation is also shown in each column

z-Bin	QSG, σ = 2.18%	AMG, σ = 0.36%	SFG, σ = 2.00%	Total Galaxies
0.50 - 0.65	1304 (7.93%)	574 (3.49%)	14567 (88.58%)	16445
0.65 - 0.84	2590 (6.81%)	1412 (3.71%)	34034 (89.48%)	38036
0.84 - 1.09	2854 (6.40%)	1698 (3.81%)	40012 (89.79%)	44564
1.09- 1.41	2650 (6.34%)	1210 (2.90%)	37916 (90.76%)	41776
1.41 - 1.88	1655 (4.17%)	1490 (3.76%)	36519 (92.07%)	39664
1.88 - 2.64	567 (1.31%)	1754 (4.05%)	41033 (94.65%)	43354
0.50 - 2.64	11620 (5.19%)	8138 (3.64%)	204081 (91.17%)	223839

Table 3.7: Number and respective percentage, the 16th, 50th, and 84th percentile of log SFR, stellar mass and sSFR of COSMOS2020 QSG per time interval in Gyr and for the total sample until $z = 2.64$. The typical standard deviation of these galaxies is also shown in the second column.

z-Bin	QSG σ =2.18%	log (SFR/[M$_\odot$ yr^{-1}])			log (M$_*$/[M$_\odot$])			log (sSFR/[yr^{-1}])		
		16th	50th	84th	16th	50th	84th	16th	50th	84th
0.50 - 0.65	1304 (7.93%)	-1.81	-0.74	0.11	8.77	10.20	10.89	-12.18	-10.59	-9.86
0.65 - 0.84	2590 (6.81%)	-1.84	-0.58	0.43	9.17	10.42	10.99	-12.28	-10.70	-9.81
0.84 - 1.09	2854 (6.40%)	-1.24	0.25	0.91	9.71	10.58	11.08	-11.97	-10.22	-9.64
1.09 - 1.41	2650 (6.34%)	-2.18	-0.25	0.92	10.25	10.77	11.15	-13.10	-10.89	-9.72
1.41 - 1.88	1655 (4.17%)	-1.61	0.70	1.51	10.44	10.87	11.21	-12.84	-10.12	-9.26
1.88 - 2.64	567 (1.31%)	-1.73	-0.47	1.45	10.65	10.99	11.28	-12.82	-11.43	-9.49
0.50 - 2.64	11620 (5.19%)	-1.83	-0.17	0.90	9.70	10.66	11.11	-12.48	-10.54	-9.64

Table 3.8: Number and respective percentage, the 16th, 50th, and 84th percentile of log SFR, stellar mass and sSFR of COSMOS2020 AMG per time interval in Gyr and for the total sample until $z = 2.64$. The typical standard deviation of these galaxies is also shown in the second column.

z-Bin	AMG σ =0.36%	log (SFR/[$M_\odot$ yr^{-1}])			log (M_*/[$M_\odot$])			log (sSFR/[yr^{-1}])		
		16th	50th	84th	16th	50th	84th	16th	50th	84th
0.50 - 0.65	574 (3.49%)	-1.06	-0.31	0.45	8.72	9.53	10.63	-10.46	-9.93	-9.40
0.65 - 0.84	1412 (3.71%)	-0.91	0.07	0.66	9.09	10.05	10.83	-10.68	-10.03	-9.36
0.84 - 1.09	1698 (3.81%)	-0.50	0.45	0.99	9.43	10.26	10.90	-10.42	-9.85	-9.30
1.09 - 1.41	1210 (2.90%)	-0.41	0.60	1.33	9.85	10.49	11.03	-10.64	-9.89	-9.17
1.41 - 1.88	1490 (3.76%)	0.15	1.15	1.70	10.19	10.69	11.10	-10.41	-9.53	-8.92
1.88 - 2.64	1754 (4.05%)	-0.10	1.32	1.90	10.36	10.76	11.13	-10.77	-9.42	-8.80
0.50 - 2.64	8138 (3.64%)	-0.57	0.59	1.50	9.56	10.50	11.02	-10.56	-9.76	-9.08

Table 3.9: Number and respective percentage, the 16th, 50th, and 84th percentile of log SFR, stellar mass and sSFR of COSMOS2020 SFG per time interval in Gyr and for the total sample until z = 2.64. The typical standard deviation of these galaxies is also shown in the second column.

z-Bin	SFG σ =2.00%	log (SFR/[$M_\odot$ yr^{-1}])			log (M_*/[$M_\odot$])			log (sSFR/[yr^{-1}])		
		16th	50th	84th	16th	50th	84th	16th	50th	84th
0.50 - 0.65	14567 (88.58%)	-0.80	-0.29	0.39	8.52	9.02	9.90	-9.76	-9.41	-9.04
0.65 - 0.84	34034 (89.48%)	-0.74	-0.13	0.57	8.58	9.02	9.85	-9.69	-9.27	-8.87
0.84 - 1.09	40012 (89.79%)	-0.39	0.15	0.85	8.81	9.32	10.15	-9.57	-9.25	-8.90
1.09 - 1.41	37916 (90.76%)	-0.04	0.52	1.09	8.92	9.52	10.32	-9.50	-9.11	-8.53
1.41 - 1.88	36519 (92.07%)	0.36	0.92	1.51	9.09	9.71	10.48	-9.28	-8.86	-8.32
1.88 - 2.64	41033 (94.65%)	0.47	1.08	1.63	9.28	9.80	10.44	-9.27	-8.81	-8.22
0.50 - 2.64	204081 (91.17%)	-0.30	0.51	1.24	8.85	9.48	10.29	-9.52	-9.10	-8.55

Table 3.10: Number, the 16th, 50th, and 84th percentile of log SFR, stellar mass and sSFR of COSMOS2020 galaxies per time interval in Gyr and for the total sample until z = 2.64.

z-Bin	Total	log (SFR/[$M_\odot$ yr^{-1}])			log (M_*/[$M_\odot$])			log (sSFR/[yr^{-1}])		
		16th	50th	84th	16th	50th	84th	16th	50th	84th
0.50 - 0.65	16445	-0.85	-0.31	0.37	8.54	9.07	10.10	-9.91	-9.45	-9.07
0.65 - 0.84	38036	-0.79	-0.14	0.57	8.60	9.08	10.11	-9.84	-9.32	-8.90
0.84 - 1.09	44564	-0.41	0.17	0.87	8.84	9.39	10.36	-9.69	-9.29	-8.92
1.09 - 1.41	41776	-0.11	0.50	1.09	8.95	9.59	10.50	-9.64	-9.16	-8.57
1.41 - 1.88	39664	0.32	0.92	1.51	9.12	9.78	10.62	-9.37	-8.91	-8.35
1.88 - 2.64	43354	0.44	1.08	1.65	9.29	9.84	10.55	-9.33	-8.84	-8.23
0.50 - 2.64	223839	-0.36	0.49	1.23	8.87	9.54	10.45	-9.64	-9.15	-8.58

Tables 3.7, 3.8, 3.9 and 3.10 represent the SFR, stellar mass, and sSFR medians of the QS, AMG, and SFG as well as the total sample up to redshift 2.64, respectively. These quantities are plotted in Figure

3.23 for easier visualization.

Figure 3.23 illustrates the medians of the sSFR (left), SFR (middle), and stellar mass (right) for the 3 types of galaxies and the total sample till redshift 2.64. The mass of the sample, including all types of galaxies, decreases over time, starting slowly and then increasing the speed. Passive galaxies and ambiguous galaxies are more massive than star-forming galaxies since they have already evolved or are in the process of evolving —they are older. The total sample is weighted by the star-forming galaxies which have low mass and are the majority of the sample ($\sim 90\%$).

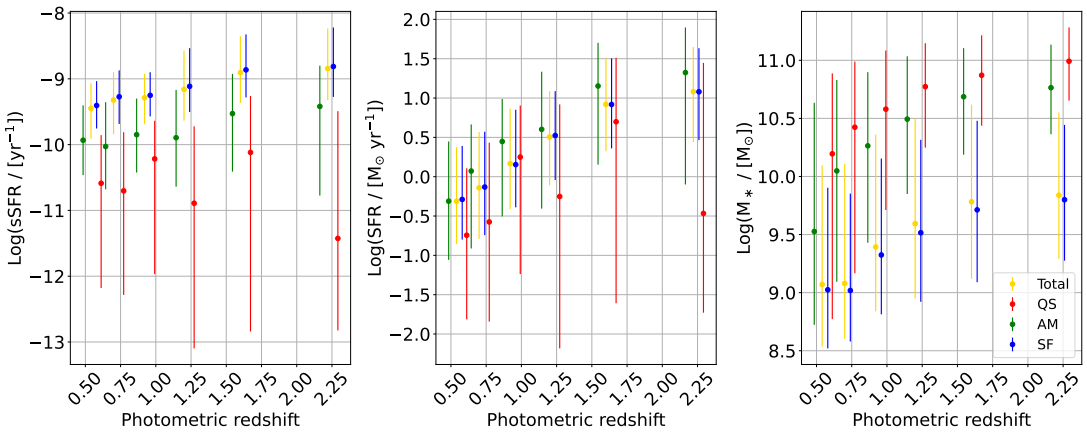

Figure 3.23: Mean log sSFR, SFR, and stellar mass for each type of galaxy per Gyr. The points were shifted for better visualization and the typical errors correspond to the 16th and 84th percentile of each group of galaxies, respectively.

Regarding the SFR, they gradually decrease for the ambiguous, star-forming galaxies and the total sample, similar to the stellar mass plot. However, the SFR of the quiescent galaxies goes up and down in the last three redshift bins, which may be caused by the lack of this type of galaxies at high redshift. The sSFR behaves similarly to the SFR, just not as accentuated since it was divided by the stellar mass.

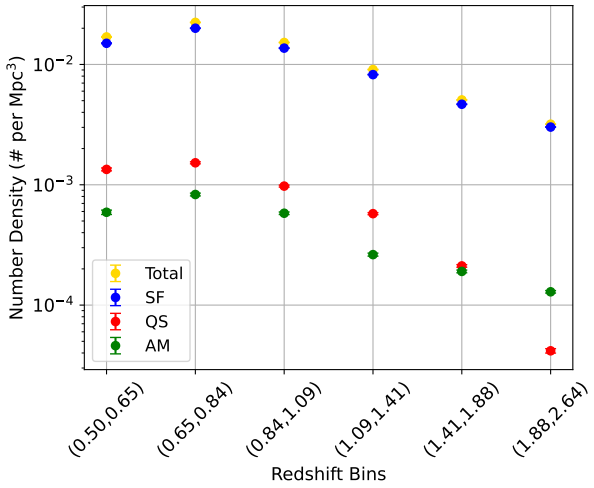

Figure 3.24: Number density for the different types of galaxies and for the total sample of COSMOS2020 per time interval in Gyr. The error bars are calculated by taking the square root of the number of galaxies in each bin.

The number density is represented in Figure 3.24. It is a smoother curve when compared to Figure 3.6, having a peak in the redshift bin (0.65, 0.84). At low redshifts, there is a higher number density of quiescent galaxies than of ambiguous galaxies. They are approximately equal at (1.41, 1.88) and swap

in the last bin. Once again, the passive curve is steeper than the ambiguous due to the survey being flux-limited.

Now that the 1 Gyr bin has been analyzed, it is also important to study how the sample changes if we increase or decrease this timescale. By changing the time interval, we want to look for physical traces that can lead us to a conclusion of the quenching timescale, for instance, how many galaxies go in and out of the ambiguous region.

Therefore, the sample was analyzed with other time intervals such as 1.5, 0.5, 0.4, 0.3, 0.2, and 0.1 Gyrs to observe the behavior of the standard deviation of the ambiguous galaxies. Figure 3.25 shows the standard deviation in percentage of the number of galaxies in each time bin for the three types of galaxies versus the time interval in Gyr. The shape of the curves of these galaxies resembles a parable with 1.0 Gyr bin being its minimum. The 0.1 Gyr bin is where it has the highest standard deviation.

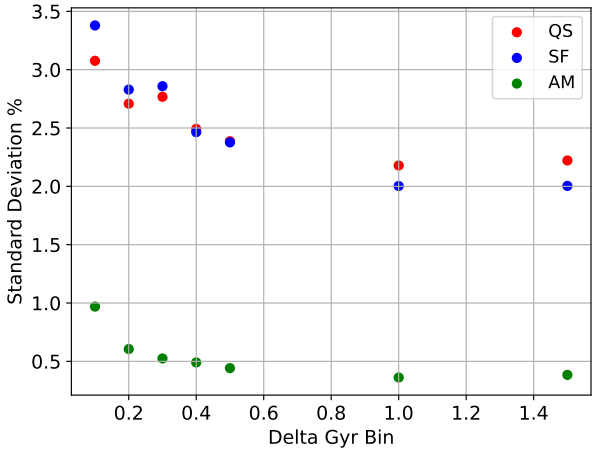

Figure 3.25: STD of the number of galaxies versus time intervals in Gyr of the three types of galaxies.

The timescale with the lowest standard deviation likely represents the typical migration timescale of these galaxies. A low standard deviation suggests that if a certain number of galaxies start migrating, a similar number will stop migrating within the same period. In our case, this period is around 1.0 Gyr. This balance — where galaxies enter and exit the migrating phase at similar rates — keeps the standard deviation low. If the timescale were longer or shorter, the standard deviation would increase because the number of galaxies in the migrating phase at any given time would fluctuate more.

However, just this simple plot is not enough to justify the typical timescale it takes a galaxy to go from star-forming to red passive nor information about PSB systems. From the analysis of the various quantities that describe the galaxies, we also saw that it is difficult to discriminate between the different types of galaxies —galaxies in the ambiguous region can also be quiescent or star-forming galaxies. So the analysis in Figure 3.25 can also be wrong. Since we do not have the SFH of the observations, we cannot predict how the timescale behaves from the data alone. We want to know if, statistically, galaxies have a typical timescale or if every galaxy has its timescale due to the many degrees of freedom —dust, SN, stellar winds, etc.— that cause a galaxy to migrate.

It is always important to compare our results to the state-of-the-art, therefore, the next approach is moving to theoretical models. We want to build a synthetic sample and analyze how parameters like SFH, metallicity, extinction, and so on, affect the distribution of the sample in the UVJ diagram. With this synthetic sample and diagrams, we will investigate if there are any physically driven criteria that we were not able to detect in the real data that are indicative of the timescale. We want to know when and where these galaxies migrate and have an insight into PSB galaxies, so after building and analyzing the

synthetic sample, we will compare it to the real data to achieve our goals.

Chapter 4

Models

A galaxy contains a large amount of information that can be derived from its multi-wavelength radiation, enabling us to study its properties with SEDs —energy emitted versus frequency or wavelength plot. These properties include the SFR of the galaxy, the age and abundance of stellar populations, the constitution of the ISM, both chemically and physically, and the distribution of atomic, molecular, and ionized gas; it can also give us insights into dust particles that extinct, i.e. absorb and scatter starlight, mainly at UV wavelengths, remitting them at IR wavelengths causing reddening, and even information related to the supermassive black hole located in the center of the galaxy.

The reddening not only depends on the quantity and geometry of the dust but also the age of the stellar populations; for example, young stellar populations emit more UV radiation than older ones and thus the interstellar reddening and extinction, and/or attenuation will be different. The color excess is a parameter that can quantify this reddening of starlight caused by interstellar dust and is denoted as $E(B-V)$ (for photometric filters B and V). It is defined as the difference between the observed color index of an object and its intrinsic color index, which is what the color would be if there were no presence of dust. The color index, in turn, is the difference in magnitude between two photometric bands, for example, B and V. Mathematically, color excess is expressed as:

$$E(B-V) = (B-V)_{\text{observed}} - (B-V)_{\text{intrinsic}} \tag{4.1}$$

The intrinsic color index is determined from theoretical models or observations of objects of the same type that are known to be unaffected by dust. A larger $E(B-V)$ value indicates more significant reddening and, therefore, a higher dust fraction.

Many galaxy properties can be determined from observations. By making a set of assumptions that incorporate our current understanding of physics, we can use synthetic SED models to generate data that closely resembles what we observe. This helps us interpret, from a more physical point of view, the observed data, increasing our knowledge about galaxies as individuals and as populations, including their SFH.

`CIGALE`, the Code Investigating GALaxy Emission, is a well-known code that was designed to study the evolution of galaxies by comparing modeled galaxy SEDs to observed ones from the X-rays and FUV to the FIR and radio. The code was written in `FORTRAN` by Burgarella et al. [2005] and Noll et al. [2009]. Now the current version available to date is in `python` and implemented by Boquien et al. [2019]. The main purpose of `CIGALE` is to generate synthetic SEDs and estimate the physical properties of galaxies from the data available from different filters. It can also generate plots of the best SED, the χ^2 distribution, the probability distribution function, and the physical properties estimations from mock catalogs (Boquien et al. [2019]).

For this work, we used CIGALE to build a synthetic sample that could reproduce, as much as the code allowed, our data from COSMOS. Once that sample was ready, we analyzed it and searched for correlations between the chosen parameters; the parameters are stated in Section 4.1 and analyzed in Section 4.3. In Section 4.2, we tested, with a simple example, how CIGALE computes fluxes from SEDs to have a better understanding of our analysis of the synthetic sample. Lastly and most importantly, we also used CIGALE in combination with COSMOS data to complete the main goals of this work which is to have a better understanding of the timescale of the quenching mechanism and search for PSB galaxies; these results can be found in Chapter 5.

4.1 Synthetic Sample Creation

We want to build a set of synthetic models that can reproduce our COSMOS observations, but before that, we want to study the impact of each parameter on the SEDs: how each input parameter affects the output, and how these are distributed along color-color plots. For that, we filled the configuration file provided by CIGALE with a list of physical modules necessary for our goals, which will be listed below.

CIGALE has 2 methods available for statistical analysis: `pdf_analysis` and `savefluxes` modules. The former fits observed SEDs of galaxies with a set of models and selects the one that fits best while the latter computes and saves spectra and properties of synthetic galaxies without relying on real data fitting (Boquien et al. [2019]). Since we want to look at the properties of simulated galaxies to have an insight into the typical timescale of the quenching comparing it to the COSMOS data, we used the `savefluxes` module as the analysis method.

There are several available modules to compute the theoretical models for the SFH, the SSP, the nebular and dust emission, the dust attenuation, the AGN, the X-ray and radio emission, the restframe parameters, and the redshift. The code also provides a wide range of filters from the X-rays and FUV to the FIR and radio to choose from; since our work encompasses the optical and NIR bands that make the UVJ, we choose the following filters, closest to the ones used in Weaver et al. [2022b]: `SUBARU_U`, `SUBARU_V`, `vista.vircam.J`, `vista.vircam.H` (information of these filters was taken from Rodrigo et al. [2012] and Rodrigo and Solano [2020]).

Regarding the SFH, CIGALE has 5 available modules, and some examples are summarized in Figure 4.1. We choose the `sfhdelayed` module which is defined as a delayed SFH with optional exponential burst and characterized by Eq. 4.2.

$$\mathrm{SFR}(t) \propto \frac{t}{\tau^2} \times \exp\left(-t/\tau\right) \text{ for } 0 \leq t \leq t_{\mathrm{max}}, \tag{4.2}$$

where t refers to the age of the oldest stellar populations, `age_main`; in other words, it tells us at what time, or at what redshift, we are observing the galaxy. t_{max} is the maximum value of `age_main` and τ, `tau_main`, is the time when the SFR peaks. Of course, when studying the whole scope of the universe, t_{max} will be equal to 13,800 Myrs.

We opted for a null second burst which makes Eq. 4.2 to be multiplied by a constant, `sfr_A`. It naturally increases the SFR, but it also sets an initial value for the stellar mass; the `tau_main` increases M_* but not by a large amount as we will in Figure 4.7. Therefore, we chose a `sfr_A` value of 1000 for our module, which reproduces values of M_* comparable to the minimum stellar mass of our COSMOS sample, $\log(\mathrm{M}_*/[\mathrm{M}_\odot]) = 8.19$.

We chose values of `tau_main` from 200 Myrs to 2800 Myrs with a step of 200 Myrs so that the galaxies would have time to enter the passive region over the range of `age_main` from 400 Myrs to 9000

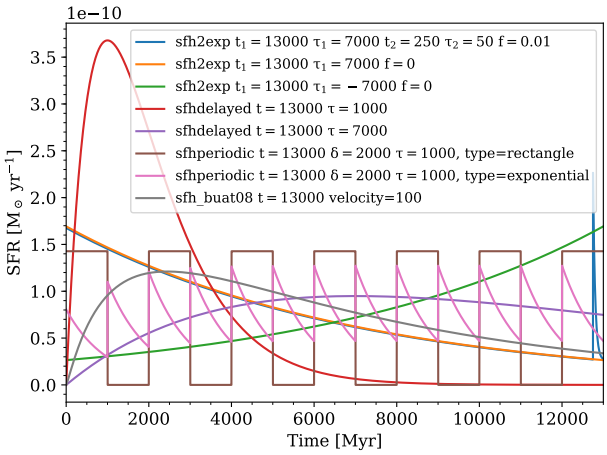

Figure 4.1: SFH generated with `sfh2exp`, `sfhdelayed`, and `sfhperiodic` modules, showing different cases of SFH. A double decreasing exponential in blue, a single decreasing exponential in orange, one increasing exponential in green, a delayed SFH with different timescales in red and purple, a periodic rectangular SFH in brown, a periodic exponential SFH in pink, and the rotation velocity-dependent SFH of Buat et al. [2008] in grey. All SFHs have been normalized to have formed 1 $M_\odot$ over 13 Gyr. Image and caption taken from Boquien et al. [2019].

Table 4.1: Parameters of the SFH module `sfhdelayed` of `CIGALE`.

SFH Modules Parameters	`sfhdelayed`
`tau_main` [Myr]	200 - 2800 $\Delta\tau = 200$
`age_main` [Myr]	400 - 9000 $\Delta t = 200$
`sfr_A`	1000
`normalise`	False

Myrs with a step of 200 Myrs. We also opted for the synthetic galaxies to not have just 1 $M_\odot$, given by `normalise`. The SFH module is then summarized in Table 4.1.

We opted for `bc03` module (Bruzual and Charlot [2003]) for the SSP with a Salpeter [1955] IMF, all the values of metallicity available in `CIGALE`, and the default age of separation between old and young stellar populations of 10 Myrs. The SSP module is then summarized in Table 4.2.

Table 4.2: Parameters of the SSP module `bc03` of `CIGALE`.

SSP Modules Parameters	`bc03`
`imf`	0 (Salpeter IMF)
`metallicity`	0.0001, 0.0004, 0.004, 0.008, 0.02, 0.05
`separation_age` [Myr]	10

For the attenuation law module, we chose a `dustatt_modified_starburst` (Calzetti et al. [2000]) where we only changed the color excess of the stellar continuum light for the young population and its factor for the old population. The other input parameters of this module stayed as default as they mostly change the output in MIR and FIR wavelengths which is outside the scope of this work. The attenuation law module is then described in Table 4.3.

Table 4.3: Parameters of the attenuation law module `dustatt_modified_starburst`.

Attenuation Law Module Parameters	`dustatt_modified_starburst`
`E_BVs_young`	0.01, 0.05, 0.1, 0.2, 0.3, 0.6, 1.0, 2.0, 3.0
`E_BVs_old_factor`	0.1, 0.2, 0.3, 0.4, 0.5, 0.6, 0.7, 0.8, 0.9, 1.0

The previous module regarded only dust absorption which attenuates the blue counterpart of the galaxies, however, since dust emits at longer wavelengths, we need to include a model for the dust to estimate the emission in the FIR. Therefore, we used `dale2014` module (Dale et al. [2014]) for dust emission, module leaving its parameters as default.

The last module we considered was the `redshifting`; it redshifts the spectrum and dims it, multiplying the wavelengths by $1 + z$ and dividing the spectrum by $1 + z$. Since the COSMOS data is already in the restframe of the galaxies, our synthetic sample should also be in the restframe. This means the redshift applied is zero.

4.2 Photometry by Means of CIGALE

Before heading to the synthetic sample analysis, we checked how `CIGALE` computes the photometry in each wave band starting from the SEDs. For this, we built a test sample where every parameter described before only had one value; in other words, the parameters were locked, only the redshift values were changed and `save_sed` is True. A SED fits file is created for each combination of values, which has several columns, but for our test, we simply need two: wavelength, λ in nm, and F_ν (flux per frequency of the model spectrum) in mJy. We transformed F_ν into F_λ (flux per wavelength of the model spectrum) in CGS units (erg s^{-1} cm^{-2} nm^{-1}) to simplify future calculus, according to the following equation:

$$F_\lambda = \frac{F_\nu}{\lambda^2}\, c. \tag{4.3}$$

Citing Boquien et al. [2019], in `CIGALE`, "the fluxes in bands are computed by integrating the model spectrum through the corresponding filter", which is given by,

$$f_\lambda = \frac{\int F_\lambda(\lambda) \times T_\lambda(\lambda)\, \mathrm{d}\lambda}{\int T_\lambda(\lambda)\, \mathrm{d}\lambda}, \tag{4.4}$$

where f_λ is the flux per wavelength through a transmission filter T. We used `Subaru / FOCAS.U`, `Subaru / FOCAS.V`, and `Subaru / IRCS.J` transmission filters for this test. The transmission curves of these filters and respective values were taken from Rodrigo et al. [2012] and Rodrigo and Solano [2020].

Following Boquien et al. [2019], we interpolated the transmission curve with the spectrum to monotonically increase sample points and not miss any features when we multiply the two. Figure 4.2 shows an example after multiplying the transmission curve with F_λ (black curves). The blue, orange, and green curves show the F_λ and the grey bands show the position of the filters on the spectrum.

Next, we integrated the area of each of the black curves and the area of the transmission curve, the numerator and denominator in Eq. 4.4, respectively. Their division gives a flux per wavelength that needs to be converted into flux per frequency by calculating the flux density in mJy for each band using λ_{pivot} in Eq. 4.5. λ_{pivot} is the wavelength in a transmission curve that makes Eq. 4.5 exact for observations made in each filter and is given by Eq. 4.6 (Rodrigo et al. [2012]; Rodrigo and Solano [2020]).

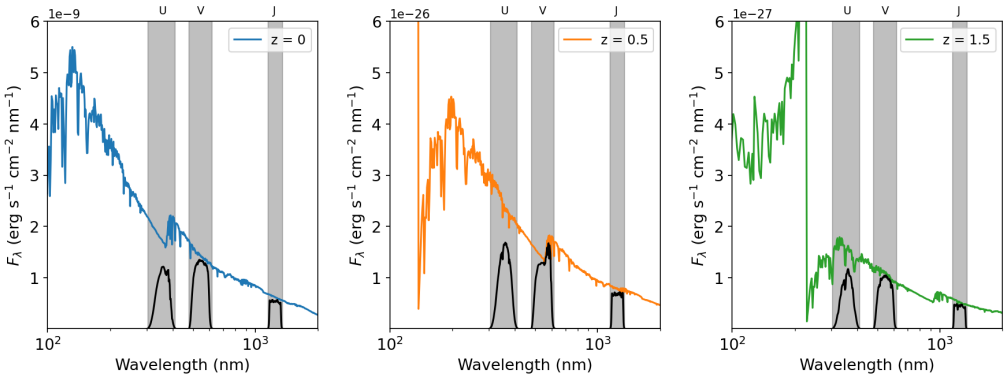

Figure 4.2: SEDs in $z = 0, 0.5$ and 1.5. The blue, orange, and green curves show the F_λ in CGS units, the black curve shows the transmission filter multiplied by the spectrum and the grey bands show the position of the filters.

$$f_\nu = \frac{\lambda^2_{\text{pivot}}}{c} f_\lambda, \tag{4.5}$$

where c is the speed of light in the vacuum and λ_{pivot} is

$$\lambda_{\text{pivot}} = \sqrt{\frac{\int T_\lambda(\lambda)\, \mathrm{d}\lambda}{\int T_\lambda(\lambda)/\lambda^2\, \mathrm{d}\lambda}}. \tag{4.6}$$

We have successfully tested how the `CIGALE` computes the photometry in each filter which will be used to analyze the synthetic sample in Section 4.3.

4.3 Synthetic Sample Analysis

After creating the configuration file of `CIGALE`, the code ran over all the possible combinations of input parameters described in Section 4.1, leading to a synthetic sample of **332,640 sources**. The distribution of these sources on the UVJ diagram is illustrated on the left side of Figure 4.3, and on the right side is the contour plot.

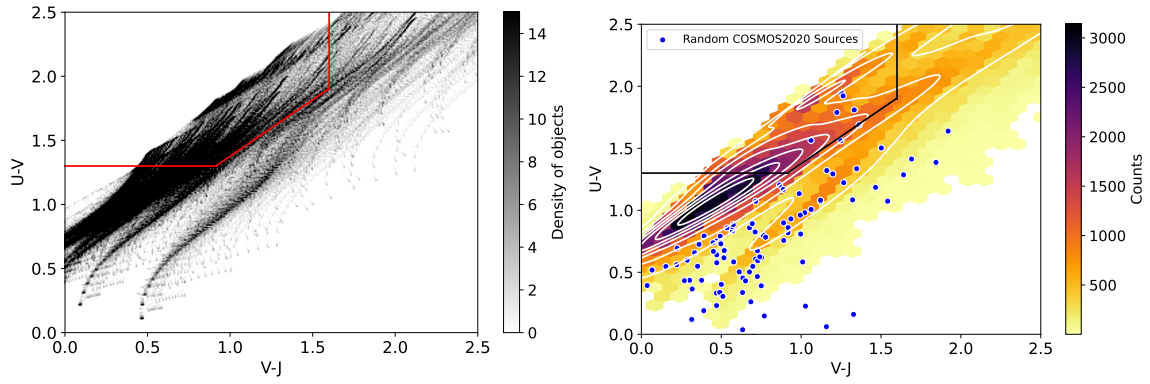

Figure 4.3: *Left:* UVJ density diagram of the synthetic sample. *Right:* UVJ contour diagram of the synthetic sample with 100 random blue points of the COSMOS sample. Red and black lines were taken from Williams et al. [2009] of 0 < z < 0.5.

We also plotted 100 random COSMOS sources (blue points) on the contour plot of Figure 4.3. The contour seems to be slightly upshifted if we would compare it with Figure 3.2. However, we still have a

large sample of galaxies inside the passive region described in Chapter 3 and a higher density of objects in the lower left corner of the star-forming region. The simulated distribution does not follow exactly the observations probably because of our choice of SFH. The SFH of real galaxies is more complex than what `CIGALE` provides; there are too many degrees of freedom that depend on each other, making it hard to do accurate simulations. We can only have a good approximation by enclosing these parameters as much as possible, as we did with `sfr_A`. However, our simulations successfully cover the parameter space of the COSMOS sample.

To better understand the position of the galaxies and how their colors change in the UVJ diagram, we plotted the SEDs of a random SF galaxy (blue) and a random QS galaxy (red) in Figure 4.4. They have approximately ($U - V \sim 0.83, V - J \sim 0.62$) and ($U - V \sim 1.42, V - J \sim 0.93$), respectively, and the gray bands correspond to the positions of the UVJ filters we used, whose values were taken from Rodrigo et al. [2012] and Rodrigo and Solano [2020]. The difference between the two SEDs is visually obvious; the QS galaxy has a very faint emission in the optical when compared to the SF galaxy. The latter also has a bluer spectrum slope and a Balmer jump, at 364.5 nm, more pronounced than the QS galaxy.

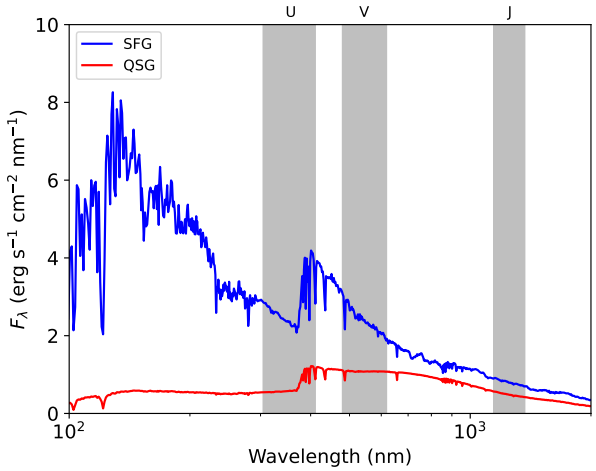

Figure 4.4: Example of SEDs models computed by CIGALE for a random SF galaxy (blue) and a random QS galaxy (red) with ($U - V \sim 0.83, V - J \sim 0.62$) and ($U - V \sim 1.42, V - J \sim 0.93$), respectively. F_λ is normalized by the average of each spectra. The gray bands show the position of `SUBARU_U`, `SUBARU_V` and `vista.vircam.J` filters.

Active galaxies, in terms of star formation, have a large difference between the fluxes of two different filters. These galaxies have high star formation rates, producing many young, luminous, and hot stars (OB-type). These stars significantly contribute to the blue part of the spectrum and can outshine older, cooler stars (K- and M-type, which appear red). As a consequence, the spectrum will have higher fluxes for short wavelengths than for longer ones, making its slope steeper and decreasing from the blue counterpart to the red one. Taking a look at Figure 4.4, if we calculated the integral of the SFG SED in the V filter, using the method described in Section 4.2, we would see it would be higher than the integral in the J filter. If we transformed the fluxes in magnitudes and color, using $V - J = -2.5 \log(f_V / f_J)$ (without considering constants), $V - J$ would be negative. Therefore, the more active a galaxy is, the higher the difference between two filters, the more negative the color, and the bluer the spectrum. The opposite also works for passive galaxies who ceased their star formation and are no longer active —their spectrum is flatter so the difference between filters is not as high.

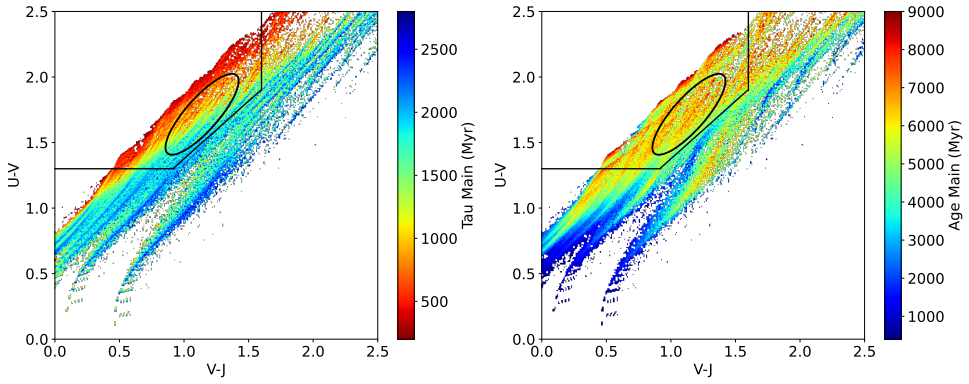

Figure 4.6: *Left:* UVJ diagram colored according to the distribution of `tau_main`, which is reported by the colorbar on the right side of the plot. *Left:* UVJ diagram colored according to the distribution of `age_main`, which is reported by the colorbar on the right side of the plot. Black straight lines were taken from Williams et al. [2009] of $0 < z < 0.5$. The ellipse represents the position of the highest density of the passive region in the COSMOS sample.

Figure 4.5 shows the SFHs with different peaks of SFR given by `tau_main`, τ in Myrs, the lines are plotted according to Eq. 4.2 and multiplied by `sfr_A`. The SFH chosen, `sfhdelayed` module, reproduces different evolution for galaxies: from a strong starburst for low values of τ to a more continuous and slow star formation for high values of τ. The former has a high SFR for the first Myrs and abruptly decreases after some time while the latter has a more smooth and continuous SFR throughout its age.

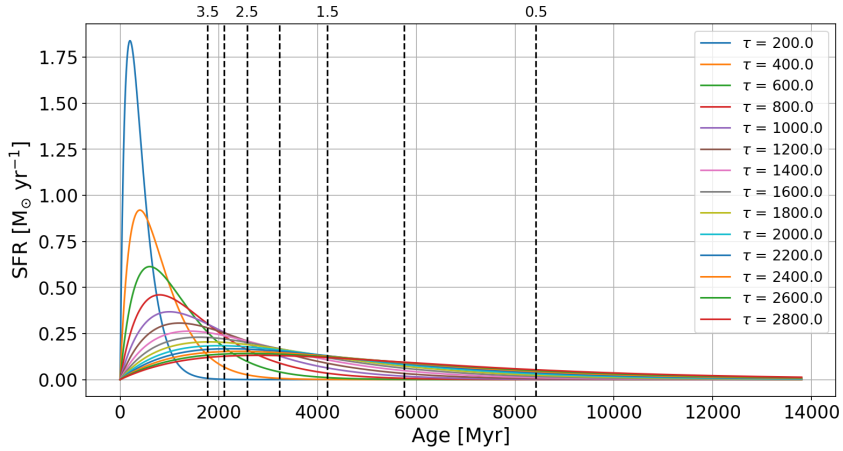

Figure 4.5: SFH of the different `tau_main`, in Myrs, described in Table 4.1. Dashed lines correspond to redshifts 0.5 to 3.5 with a step of 0.5.

Figure 4.6 illustrates, on the left, the distribution of `tau_main` —peak of star-formation—, and on the right, of `age_main` —age of the oldest stars or the time of the universe we see the galaxies (note that we are always in restframe)— in the UVJ diagram. Regarding `tau_main`, the passive region has a mix of galaxies with low and medium `tau_main` while the SF region has higher `tau_main`. On the other hand, regarding `age_main`, the passive region has a mix of old (red points) and medium-aged galaxies (green points) while the SF region has the addition of younger galaxies (blue points). The ellipse in black depicts the position of the highest density of the passive region in the COSMOS sample, which will be analyzed in detail in Chapter 5.

By comparing both Figure 4.5 and Figure 4.6, when the peak of the star formation activity occurs at

early times ($\tau < 1000$ Myr), 38.17% of the galaxies are located inside the passive region while when the peak occurs at late times ($\tau > 1000$ Myr), 84.79% are in the star-forming region. Galaxies at early times have a much higher SFR than those at late times, for example, compare $\tau = 200$ Myr or $\tau = 400$ Myrs with $\tau = 2000$ Myr. Since their star formation is so abrupt and lasts for a small period, it makes sense that no matter the age of the universe most early-time galaxies have already ceased their star formation and so they are present inside the passive region. On the other hand, late-time bursts are smoother, lasting for longer periods, occupying the star-forming region.

As expected the passive region contains galaxies with low SFR and high stellar mass, both in red in Figure 4.7. On the other hand, the star-forming region, mainly the lower left corner, has higher SFR and lower stellar mass, both in blue.

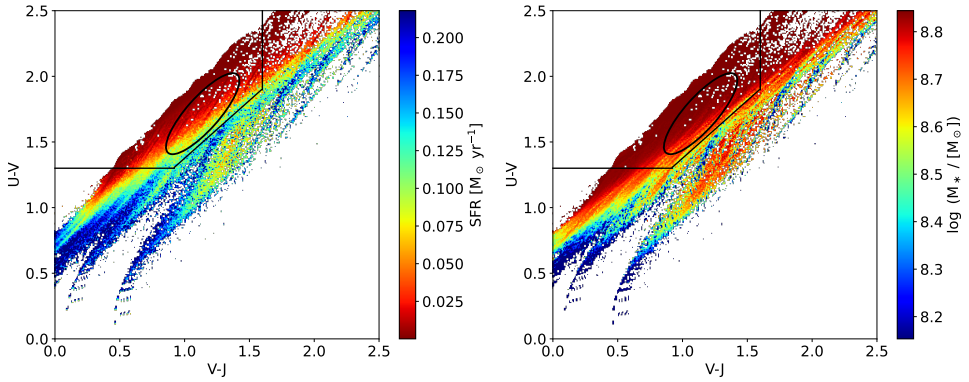

Figure 4.7: *Left:* UVJ diagram colored according to the distribution of SFR, which is reported by the colorbar on the right side of the plot. *Right:* UVJ diagram colored according to the distribution of stellar mass, which is reported by the colorbar on the right side of the plot. Black straight lines were taken from Williams et al. [2009] of $0 < z < 0.5$. The ellipse represents the position of the highest density of the passive region in the COSMOS sample.

As previously mentioned, the H-band magnitude acts as a proxy for stellar mass, having a linear correlation (see Dai et al. [2021]); this makes its distribution in the UVJ diagram similar to the stellar mass, left side of Figure 4.8. The passive region has brighter magnitudes (lower values) than the star-forming region (lower left corner). However, in these plots, we notice a region around ($U-V \sim 1.3, V-J \sim 1.4$) with higher stellar mass and `age_main`, and lower H magnitude and SFR, somewhat resembling the dust diagonal line in COSMOS UVJ plots from Chapter 3. However, as we will see on the right side of Figure 4.8 and in Figure 4.9, this is not triggered by the color excess of the stellar continuum light, but by the stellar metallicity.

On the right side of Figure 4.8 is the stellar metallicity distribution in the UVJ diagram. Only a few passive galaxies have metallicities of 0.05 (blue points), 2.39%, and 0.02 (yellow points), 17.16%. This seems to imply that, counterintuitively, stellar metallicity does not have an impact on the position of the galaxies in the diagram and that passive galaxies are not metal-rich. We investigated further and found out it was because of degeneracies (e.g. between metallicity and dust) in the stellar population synthesis models; it saturates the metallicity of the sequence. As metallicity increases, it introduces a curving effect that eventually plateaus, likely caused by the similarity of SEDs among these sources mainly the slope.

So while metallicity does not redden the galaxies in the passive region, it reddens the ones in the star-forming region mainly at ($U - V \sim 1.3, V - J \sim 1.4$). The passive galaxies are red because they are older and have stopped their star formation.

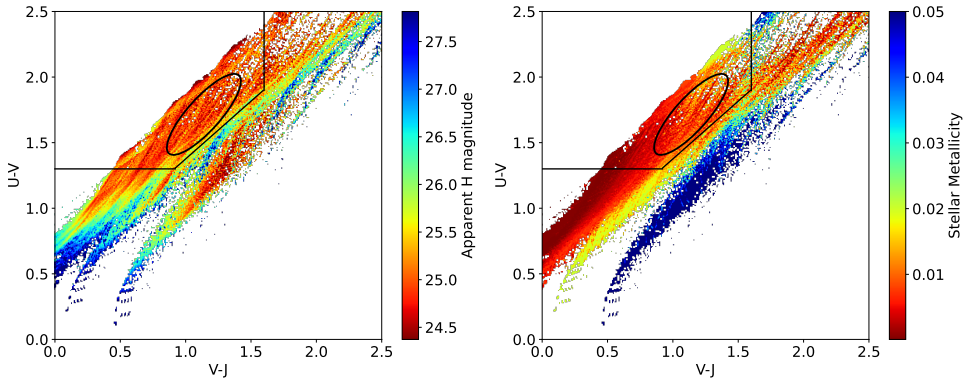

Figure 4.8: *Left:* UVJ diagram colored according to the distribution of H-band magnitude, which is reported by the colorbar on the right side of the plot. *Right:* UVJ diagram colored according to the distribution of `stellar.metallicity`, which is reported by the colorbar on the right side of the plot. Black straight lines were taken from Williams et al. [2009] of $0 < z < 0.5$. The ellipse represents the position of the highest density of the passive region in the COSMOS sample.

Figure 4.9 shows the distribution of the color excess for the young and the old stellar population, `E_BVs_young` and `E_BVs_old`, respectively. `E_BVs_old` is simply `E_BVs_young` multiplied by the `E_BVs_old_factor`. As expected both plots are very similar, star-forming galaxies seem to be more extinct than passive galaxies above all in the top-right corner of the diagram. The passive galaxies do not have the star formation to heat the dust and for this one to emit at IR bands. The dust line, diagonal from left to right and upwards in the UVJ plane, increases in extinction as both $U - V$ and $V - J$ increase. The objects that have a difference of 3.0 magnitudes (red) are highly extinct and are present outside the UVJ plane considered.

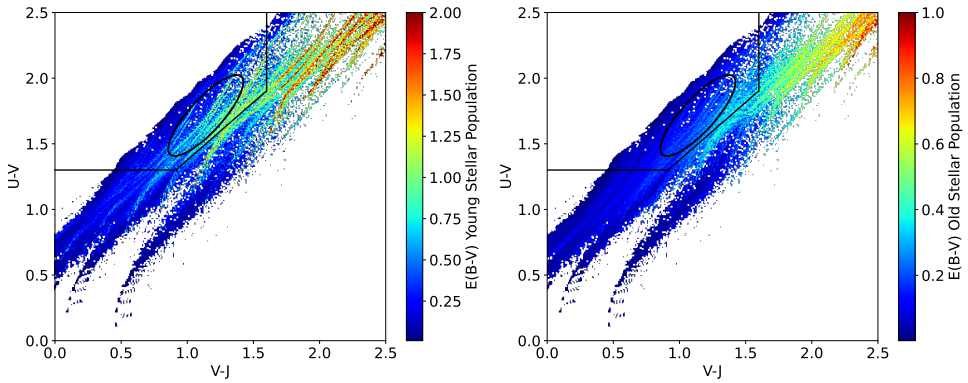

Figure 4.9: *Left:* UVJ diagram colored according to the distribution of `E_BVs_young`, which is reported by the colorbar on the right side of the plot. *Left:* UVJ diagram colored according to the distribution of `E_BVs_old`, which is reported by the colorbar on the right side of the plot. Black straight lines were taken from Williams et al. [2009] of $0 < z < 0.5$. The ellipse represents the position of the highest density of the passive region in the COSMOS sample.

Chapter 5

Results

One of the main goals of this work is to explore the significance of PSB galaxies in the evolutionary history of the universe. Are these systems dominant during specific cosmic epochs? Is there a connection between PSB galaxies and the early or late stages of the universe? To address these questions, it is essential to investigate the quenching timescale—the time it takes for a galaxy to transition from SF to QS.

To achieve this, we defined a region in the UVJ diagram that represents the densest cluster of points in the passive region of our COSMOS sample, both visually and mathematically. This allowed us to estimate the typical quenching timescale and determine the percentage of PSB systems across different redshift and cosmic time (Gyr) bins. As we will show later, the fraction of PSB galaxies varies significantly depending on the age of the universe.

5.1 Representative Sample of COSMOS Passive Galaxies

We used a PCA-based approach is a statistical technique used for dimensionality reduction, feature extraction, and identifying patterns in data. PCA helps visualize density more effectively, especially when the distribution isn't aligned with the original axes. This makes it a powerful tool for identifying and highlighting the core structure of the data. This approach identifies the directions of maximum variance in a certain region of our data, in our case, the densest region of the passive region. We end up with a shape that best fits inside an ellipse whose parameters are described in Table 5.1 and were previously illustrated in the UVJ diagrams from Chapter 4 Section 4.3.

Table 5.1: Parameters of the ellipse which represents the densest region of points in the passive region of the COSMOS sample.

Ellipse Parameters	
center (x, y)	(1.1395506, 1.7154297)
width	0.80
height	0.25
angle [°]	48

There are **12,084 COSMOS sources** within this region, representing approximately 74.25% of the passive galaxies in the sample. This percentage is slightly higher than the value reported in Table 3.1, as it includes the total passive population plus a portion of the ambiguous region. This overlap occurs because we use the passive limits defined by Williams et al. [2009] for $0 < z < 0.5$, which partially overlap

with the ambiguous region, thereby including some AMG. Since our simulated data does not have an ambiguous region (due to the absence of photometric errors), we opted to calculate the percentage in this manner for consistency. The densest region also constitutes 4.85% of the total COSMOS sample.

Figure 5.1 shows the distribution of photometric redshift (left panel) derived using `ez_z_phot` from `EAZY`, and the corresponding age distribution (right panel). The photometric redshift has a median value of 0.98, with the number of sources increasing as redshift decreases —passive galaxies are more easily detected at lower redshifts. When redshift is transformed into cosmic age, the region has a median age of 5.82 Gyr, with the number of sources increasing up to this point and decreasing thereafter.

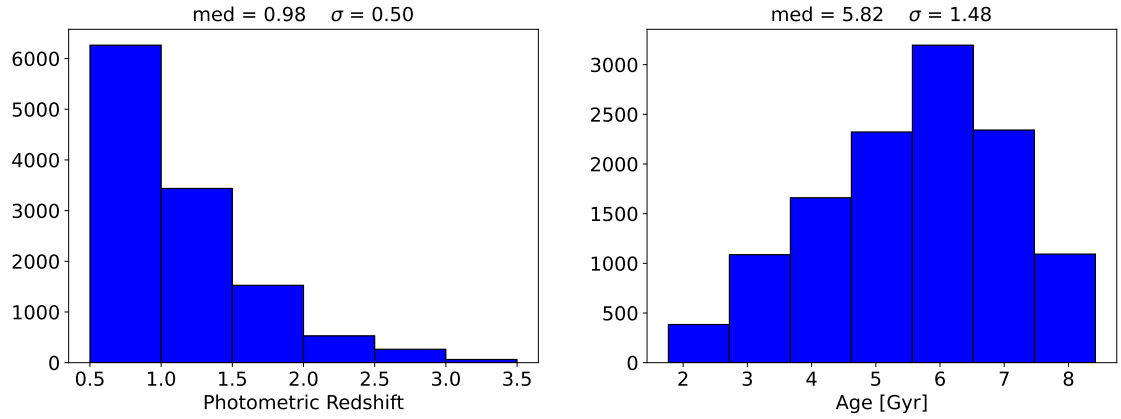

Figure 5.1: *Left:* Distribution of the photometric redshift of COSMOS galaxies inside the densest region of passive galaxies. *Right:* Distribution of the age of COSMOS galaxies inside the densest region of passive galaxies.

We selected models inside the same region and its parameters (as detailed in Table 5.1) in our `CIGALE` sample. As expected, the total number of sources in this region is higher for the simulated data, due to the larger size of the `CIGALE` models compared to COSMOS. It is important to note, however, that we are ”observing” the same galaxies at different epochs of the universe. This repetition occurs because `age_main` is an evolutionary parameter that represents the age of a galaxy at a given epoch (i.e., the age of the model). In the simulations, a model is: all parameters are fixed except `age_main` and since we have 43 values of it, a model will then have 43 entries, meaning galaxies with the same model parameters can appear multiple times in the quiescent region at different ages.

From the sources within the representative region of passive galaxies in `CIGALE`, we selected those with ages approximately matching the galaxies in COSMOS. For cases where multiple sources shared the same age but were derived from different models, we randomly selected one. This process produced a synthetic, reduced, and random sample of **12,084 sources** —hereafter referred to as the **main sample**— corresponding in age to the COSMOS galaxies (i.e., within the range $0.5 < z < 3.5$).

5.2 Main Sample Analysis

Figure 5.2 illustrates the distributions of `age_main` (left panel) and `tau_main` (right panel) for the main sample. In this random run, the sample has a median `age_main` of 5.8 Gyr, consistent with the COSMOS sample as expected. The distribution shifts toward older ages because only galaxies with intense SFRs and (usually) low `tau_main` values (e.g., 200–400 Myr) can transition into the passive region so early. Galaxies with higher `tau_main` values usually take longer to quench, thus shifting the distribution toward older ages. The main sample has a median `tau_main` of 1200 Myr, reflecting the galaxies with relatively

lower `tau_main` values, which are more likely to have extinguished their star formation earlier compared to those with higher `tau_main` values that sustain more constant SFRs (see Figure 4.5).

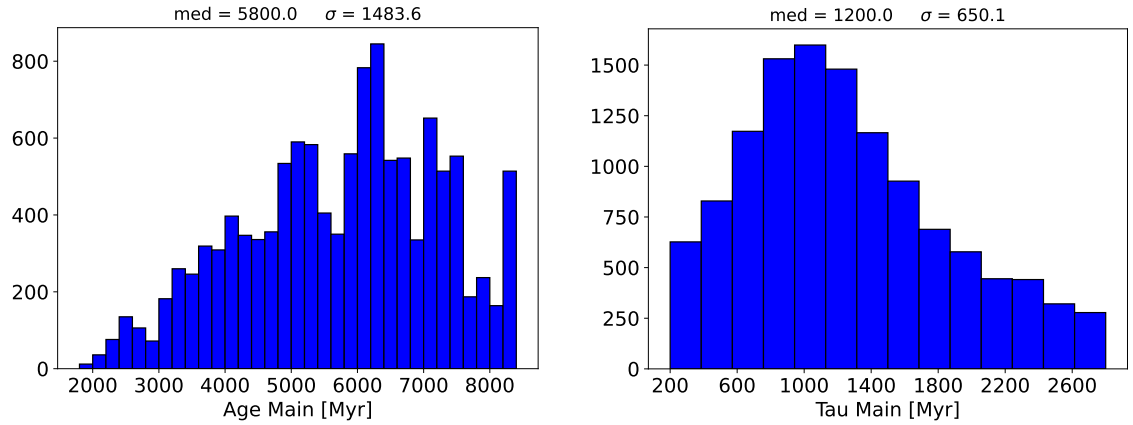

Figure 5.2: *Left:* Distribution of `age_main` of the main sample. *Right:* Distribution of `tau_main` of the main sample. Both for one random run.

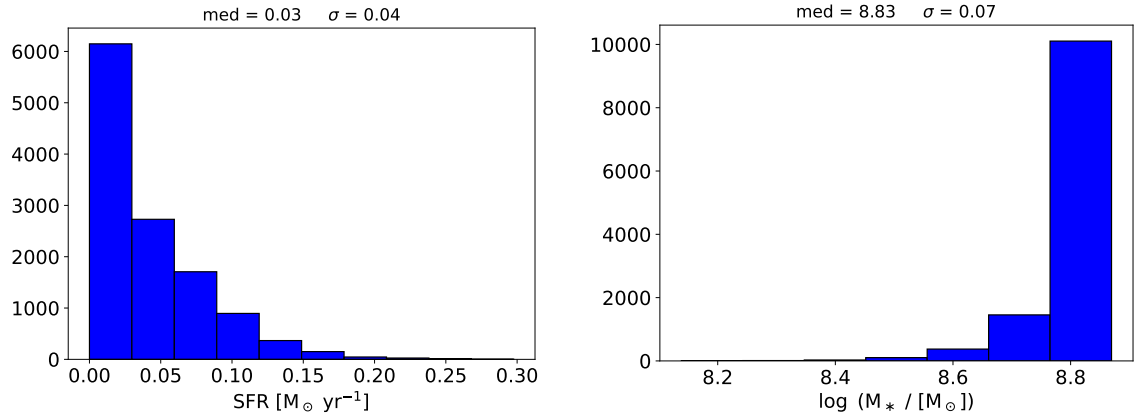

Figure 5.3: *Left:* Distribution of SFR of the main sample. *Right:* Distribution of stellar mass of the main sample. Both for one random run.

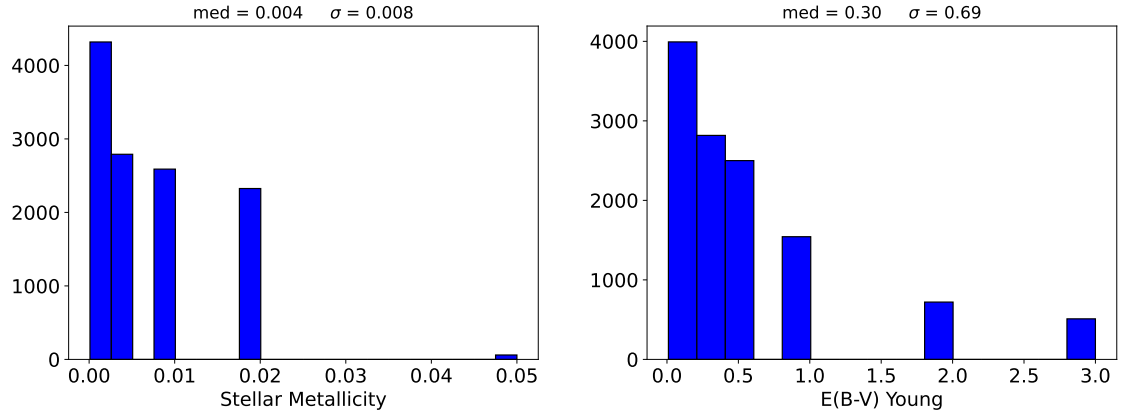

Figure 5.4: *Left:* Distribution of the stellar metallicity of the main sample. *Right:* Distribution of `E_BVs_young` of the main sample. Both are from one random run.

Figure 5.3 shows the distributions of SFR (left panel) and stellar mass (right panel) for the main

sample in this random run. As expected for passive galaxies, the sample exhibits very low SFRs, with a median value of 0.03 $M_\odot$ yr^{-1}, and a median stellar mass of $\log(M_*/[M_\odot]) = 8.83$, which aligns with the lowest values observed in the COSMOS sample.

Finally, Figure 5.4 presents the distributions of stellar metallicity (left panel) and the color excess $E(B-V)$ of the young population (right panel) for the main sample in this random run. As discussed in Chapter 4, the passive galaxies in this sample are neither metal-rich nor heavily extinct, which is confirmed once again by this figure. The main sample has a median stellar metallicity of 0.004 and a median $E(B-V)$ of 0.3 for the young population.

5.3 Quenching Timescale and Hunting for Post-Starburst Galaxies

This work aims to estimate the quenching timescale—whether it reflects a rapid process or a secular one that takes several billion years. PSB galaxies are characterized by recent intense bursts of star formation followed by an abrupt stop, resulting in short quenching timescales. Previous studies, such as those by Wild et al. [2009], Poggianti et al. [2009], Belli et al. [2019], and Wild et al. [2020], have concluded that for a galaxy to be classified as PSB, its quenching timescale must be less than 1 Gyr.

To calculate this timescale, it is essential to determine when the galaxies in the main sample transitioned into the passive region. This can be done by tracing the evolution of the `age_main` parameter for the 12,084 galaxies in the main sample. Notably, many of these galaxies share repeated models, as `age_main` is an evolutionary parameter. To clarify, a model is defined as a unique combination of all parameters except `age_main`. Our focus is on the first entry of `age_main` for a given model in the passive region, which we refer to as `t_quench`, representing the approximate time a galaxy became passive. Out of the 12,084 sources, 8,283 were found to have repeated models, leaving **3,801** unique models within the region.

The left panel of Figure 5.5 displays the distribution of `t_quench` for one random run. The distribution has a median of 3.0 Gyr and a standard deviation of approximately 1.2 Gyr. By definition, values of `t_quench` are always lower than `age_main`, which represents the "observation time" of the galaxies in the main sample. Consequently, the peak of `t_quench` is shifted to the left compared to the peak of `age_main`, as seen in the left panel of Figure 5.2.

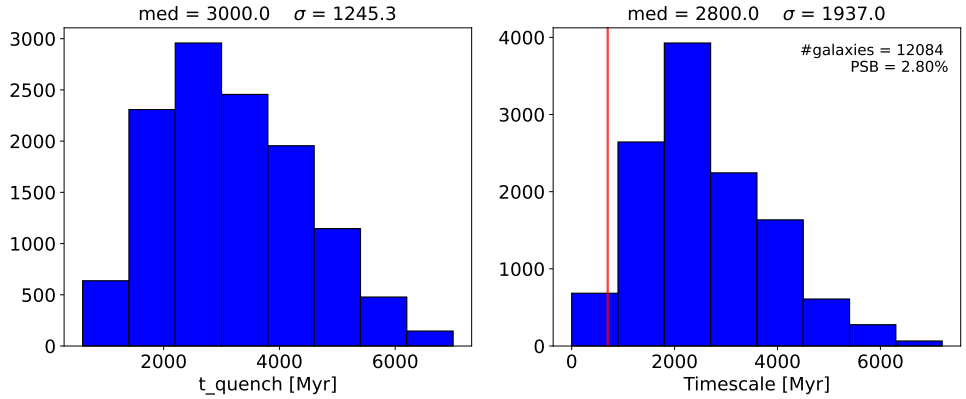

Figure 5.5: *Left:* Distribution of `t_quench` of the main sample. *Right:* Distribution of timescale (difference between `age_main` and `t_quench`) of the main sample with the percentage of PSB systems. The red vertical line illustrates the timescale where we consider galaxies to be PSB (timescale < 0.7 Gyrs). Both plots are from one random run.

The quenching timescale, defined as the difference between `age_main` and `t_quench`, indicates how long time ago the galaxies entered the passive region. This parameter is shown in the right panel of Figure 5.5 for the same random run. The distribution has a median timescale of 2.8 Gyr, a standard deviation of approximately 1.9 Gyr, and a peak that is slightly shifted to the left. Following the criteria established by Wild et al. [2009], Belli et al. [2019] and Wild et al. [2020], we classified PSB galaxies as those with quenching timescales shorter than 0.7 Gyr. In this particular run, 338 galaxies — 2.80% of the sample of 12,084 sources— meet this criterion and are classified as PSB systems.

If the majority of galaxies within the main sample were PSB systems, the distribution of quenching timescales in the right panel of Figure 5.5 would form a Gaussian centered around 1 Gyr or lower. However, this is not observed because the sample consists of a diverse mix of galaxies, including a large fraction of objects that are passive because of secular evolution. As a result, the sample is not dominated by PSB systems, which aligns with the broader characteristics of the main sample.

5.3.1 Main Sample Divided into 0.5 Redshift Bins

Similar to what was done in Chapter 3, Figure 5.6 shows the timescale distribution divided into redshift bins of 0.5 intervals between $0.5 < z < 3.5$ of a random run. Additionally, both the median and standard deviation of the timescale decrease as redshift increases, indicating that galaxies quench more quickly at higher redshifts.

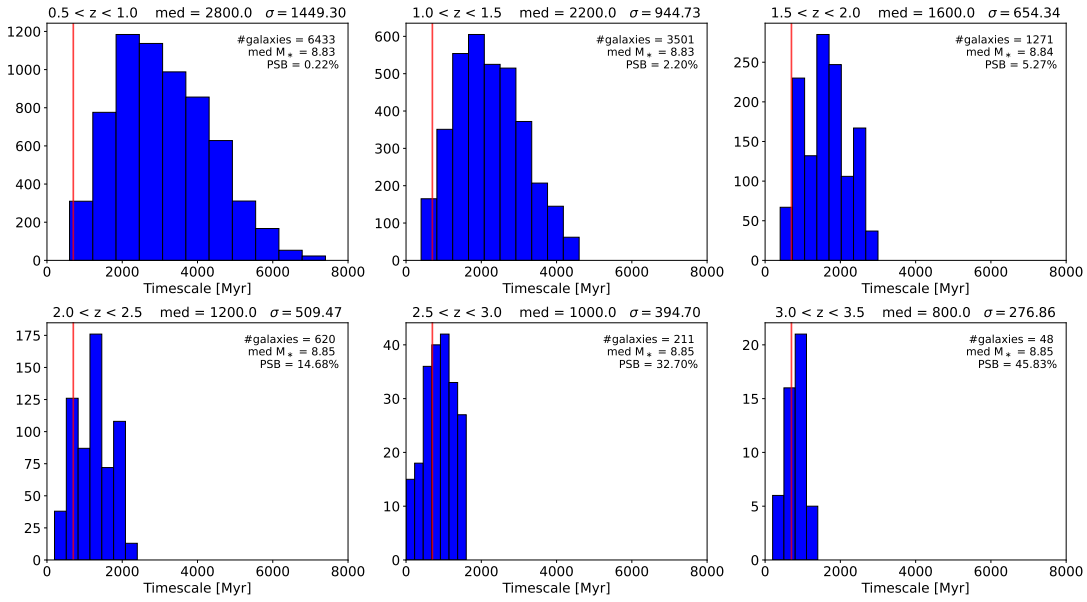

Figure 5.6: Distribution of timescale of the main sample of a random run divided in 0.5 redshift bins between $0.5 < z < 3.5$. On the right side of each plot is indicated the number of galaxies in that redshift bin, their stellar mass, and the percentage of those that are PSB, timescale < 0.7 Gyrs, represented by the red vertical line.

To better understand this behavior, let us consider the following example. Suppose we "observe" a passive galaxy at $z = 0.75$, corresponding to an age of the universe of 6.89 Gyr. If its quenching timescale is 3.00 Gyr (the median for this redshift bin), it would have entered the passive region at 3.89 Gyr of age, corresponding to $z = 1.64$ —a time just after the peak of cosmic star formation. Similarly, for a passive galaxy observed at $z = 1.25$ (age 4.88 Gyr) with a timescale of 2.20 Gyr, it would have quenched at 2.68 Gyr, corresponding to $z = 2.40$, which falls on the opposite side of the star formation decline shown in Figure 1.6. Repeating this analysis for the remaining redshift bins produces the data

Table 5.2: Example from Figure 5.6 explaining when the galaxies enter the passive region in each redshift bin.

z-Bin	z Observed	Age Observed [Gyr]	Timescale [Gyr]	Age QS Enter [Gyr]	z QS Enter
0.5 - 1.0	0.75	6.89	3.00	3.89	1.64
1.0 - 1.5	1.25	4.88	2.20	2.68	2.40
1.5 - 2.0	1.75	3.66	1.60	2.06	3.06
2.0 - 2.5	2.25	2.87	1.20	1.67	3.68
2.5 - 3.0	2.75	2.32	1.00	1.32	4.48
3.0 - 3.5	3.25	1.93	0.80	1.13	5.08

summarized in Table 5.2.

Using the previously established PSB definition, the proportion of PSB galaxies increases significantly with redshift. In the first redshift bin ($0.5 < z < 1.0$), only 0.22% of galaxies are classified as PSB, whereas in the last redshift bin ($3.0 < z < 3.5$), this fraction increases to 45.83%. This trend is visually supported by the vertical red line at 700 Myr in Figure 5.6, which shows the distributions shifting leftward, increasingly entering the PSB region as redshift increases. The median stellar mass of these galaxies increases from $\log(M_*/[M_\odot])$ = 8.83 to $\log(M_*/[M_\odot])$ = 8.85.

Until this point, our analysis of `t_quench` and quenching timescales has relied on a single random run. However, performing a different run would yield a slightly different sample of galaxies due to variations in the parameter combinations. To evaluate the effect of this "randomness", we conducted 100 random runs to calculate the median `t_quench` and quenching timescale for each redshift bin and the total sample, as shown in Table 5.3. Each run considers a random match of a synthetic galaxy for each of the COSMOS ones, so we do that 100 times.

From these tests, we found that randomness has little effect on the results. The highest standard deviation of the medians for both `t_quench` and the quenching timescale is 100 Myr, with some cases showing no variation at all (STD = 0). Additionally, the variation in distribution widths is even smaller, with a maximum STD of 24 Myr — an order of magnitude lower than the STD of the medians. This confirms that matching each COSMOS galaxy with a random counterpart from our models does not significantly impact the derived `t_quench` values or quenching timescales.

Table 5.3: Median values of `t_quench` and the quenching timescale of 100 random runs divided into 0.5 redshift bins and for the whole main sample, $0.5 < z < 3.5$.

z-Bin	Median t_quench [Myr]	Median Timescale [Myr]
0.5 - 1.0	3800	2800
1.0 - 1.5	2800	2200
1.5 - 2.0	2200	1600
2.0 - 2.5	1800	1200
2.5 - 3.0	1400	1000
3.0 - 3.5	1200	800
0.5 - 3.5	3000	2800

From Table 5.3, the median `t_quench` computed over 100 random runs is 3.0 Gyr. This indicates that galaxies in the main sample entered the passive region when they were approximately 3.0 Gyr old. The

typical quenching timescale —representing how long ago these galaxies became passive—is 2.8 Gyr. Of course, the sum of these two medians corresponds to the median `age_main` of the main sample and aligns with the median age of COSMOS galaxies. Both medians decrease with increasing redshift, reaching a minimum of 1.2 Gyr for `t_quench` and 0.8 Gyr for the quenching timescale, consistent with a faster quenching process at higher redshifts, also confirmed by, e.g, Belli et al. [2019], Forrest et al. [2018], Rowlands et al. [2018], Wild et al. [2016].

This trend is further supported by Table 5.4, which presents the median and STD of PSB galaxy percentages across 100 random runs for each redshift bin and the entire main sample. The fraction of PSB galaxies relative to "normal" passive galaxies increases significantly with redshift, rising from 0.23% in the first redshift bin ($0.5 < z < 1.0$) to a peak of 39.58% in the last bin ($3.0 < z < 3.5$). As the total number of galaxies (both PSB and "normal") decreases with redshift, the STD of PSB fractions also increases, reaching a significant value of 7.45% in the last bin. This indicates a greater change in the number of PSB galaxies across random runs at high redshift, where whether a galaxy is classified as PSB or not has a larger impact due to the smaller sample size. In contrast, this effect is negligible in the lower redshift bins, where the main sample contains many more galaxies.

Table 5.4: Median and STD values of the percentage of PSB galaxies of 100 random runs divided into 0.5 redshift bins and for the whole sample, $0.5 < z < 3.5$.

z-Bin	Median PSB %	STD PSB %
0.5 - 1.0	0.23	0.06
1.0 - 1.5	2.03	0.22
1.5 - 2.0	6.29	0.80
2.0 - 2.5	14.52	1.53
2.5 - 3.0	30.81	3.13
3.0 - 3.5	39.58	7.45
0.5 - 3.5	2.82	0.14

Our results align with the previous study done by Belli et al. [2019], who analyzed a sample of 5335 galaxies from the UltraVISTA survey (McCracken et al. [2012]). Belli et al. [2019] selected a population of quiescent galaxies with young stellar ages (see Figure 10 of Belli et al. [2019]) and defined PSB galaxies as those with stellar ages between 300 Myr and maximum age, which they tested at 600 Myr, 800 Myr, and 1 Gyr. With this selection, Belli et al. [2019] concluded that "the overall population of quiescent galaxies grows rapidly with cosmic time" while, at the same time, PSB galaxies become increasingly more significant with redshift, from 4% of the quiescent population at $z \sim 1$ to 34% at $z \sim 2.5$.

In our main sample, PSB galaxies account for 2.82% of the total population. This suggests that the majority of galaxies did not undergo a PSB phase but instead experienced more gradual, secular quenching, entering the passive region at later stages. These findings are consistent with those of Belli et al. [2019] and Wild et al. [2016], which similarly highlight the dominance of secular processes in galaxy quenching.

At first glance, the increase in PSB galaxies with redshift might appear to derive solely from the intense peaks of star formation (low `tau_main`) at early times (see Figures 4.5 and 4.6). Under this assumption, galaxies with lower `tau_main` would exhaust their gas supply more quickly, causing star formation to cease sooner than in galaxies with higher `tau_main`, leading to shorter quenching timescales and more cases of PSB systems. However, this explanation is challenging at high redshift without con-

sidering AGN feedback, galaxy mergers or accretion of pristine gas from the cosmic web, as neither of these processes were incorporated into our synthetic sample. In the early universe, where gas reservoirs were abundant, galaxies typically accreted gas, formed stars, then repeated this cycle. As such, rapid transitions to quiescence would be improbable without the presence of strong internal or external feedback mechanisms.

After doing some tests, we found little correlation between the quenching timescale and `tau_main`. A low `tau_main` does not necessarily correspond to shorter quenching timescales. Although galaxies with lower `tau_main` experience a more rapid decline in SFR, other parameters, such as metallicity or color excess, can delay their entry into the passive region in the /(UVJ/) diagram. Thus, it is possible for galaxies with low `tau_main` to quench at later times despite their initially steep SFH decline.

These findings highlight that the quenching timescale depends on a complex interplay of physical parameters beyond the SFH defined by `tau_main`. Factors like metallicity, extinction, and attenuation curves significantly influence the transition to the passive region, due to effects of degeneracy, underscoring that SFH alone does not determine how quickly a galaxy becomes quiescent. Consequently, our results for quenching timescales —and by extension, the prevalence of PSB galaxies— are not merely based on our chosen SFH model. Instead, they have a solid physical basis, shaped by the interaction of the diverse parameters used to construct our synthetic sample in Chapter 4.

However, the role of AGN feedback or mergers remains uncertain, as these mechanisms were not included in the models. Their exclusion might limit the interpretation of rapid quenching events in our sample.

We conclude that SFH alone can predict a small fraction of PSB galaxies, 2.82%, Table 5.4.

5.3.2 Main Sample Divided into 1 Gyr Bins

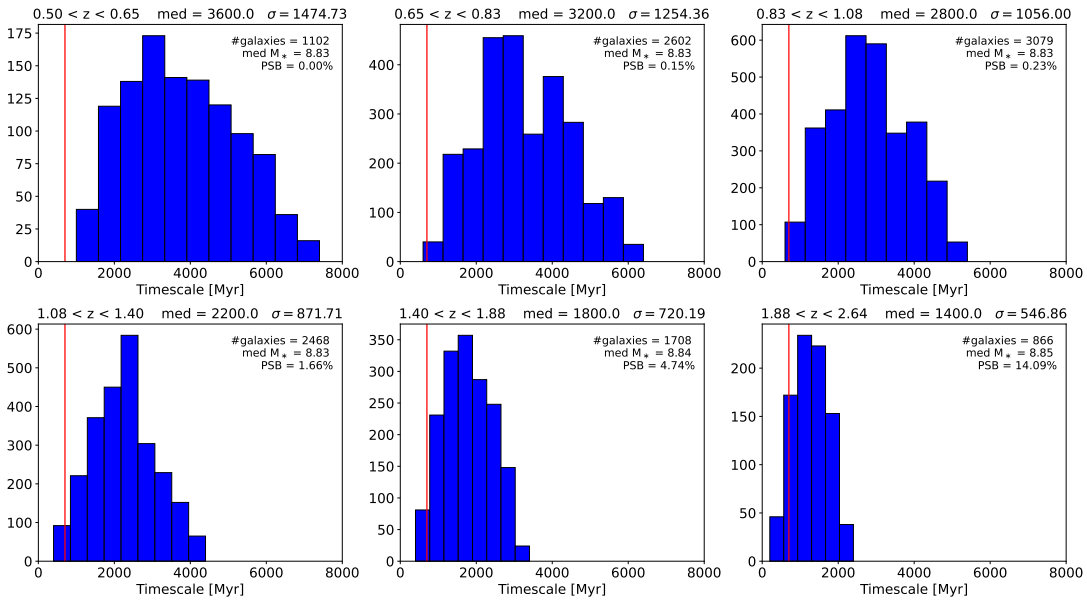

Figure 5.7: Distribution of timescale of the main sample of a random run divided in 1 Gyr bins between $0.5 < z < 2.64$. On the right side of each plot is indicated the number of galaxies in that redshift bin, their stellar mass, and the percentage of those that are PSB, timescale < 0.7 Gyrs which is represented by the red vertical line.

To further analyze the data, it is essential to examine how the sample behaves when divided into 1 Gyr bins, given that redshift is not a linear parameter. Following the same methodology as in Chapter 3 for

redshifts up to $z = 2.64$, Figure 5.7 illustrates the distribution of quenching timescales within these 1 Gyr bins for a single random run. Similar to the findings from 0.5 redshift bins, the median and STD of the timescale decrease with redshift, indicating that galaxies quench faster at higher redshifts. The fraction of PSB galaxies also increases with redshift, starting at 0% in the first redshift bin ($0.50 < z < 0.65$) and reaching a maximum of 14.09% in the highest redshift bin ($1.88 < z < 2.64$). Compared to Figure 5.6, the increase in PSB galaxies is less abrupt and follows a more linear trend when the data is divided into 1 Gyr bins. The median stellar mass of these galaxies also increases from $\log(M_*/[M_\odot]) = 8.83$ to $\log(M_*/[M_\odot]) = 8.85$.

Figure 5.7 also shows the number of galaxies within each bin that fall inside the main sample passive region. Notably, there is a peak in the number of galaxies within the redshift bin $0.83 < z < 1.08$, occurring shortly after the peak of cosmic star formation identified by Madau and Dickinson [2014] near $z = 2$ (see Figure 1.6). This peak in galaxy counts likely corresponds to star-forming galaxies that have transitioned into the passive region, reflecting the expected sequence where the peak of quenched galaxies follows the peak of star formation.

Using the same analysis as before, let's consider a galaxy observed at $z = 0.58$, which corresponds to an age of 7.89 Gyr. If this galaxy has a quenching timescale of 3.60 Gyr, it would have transitioned into the passive phase when the universe was 4.29 Gyr old, which corresponds to a redshift of $z = 1.46$. Similarly, a galaxy observed at $z = 0.74$ with an age of 6.94 Gyrs and a quenching timescale of 3.00 Gyrs would have quenched at 3.94 Gyrs, equivalent to $z = 1.61$. Extending this analysis across all bins delivers the results presented in Table 5.5.

Table 5.5: Example from Figure 5.7 explaining when the galaxies enter the passive region in each Gyr bin until $z = 2.64$.

z-Bin	z Observed	Age Observed [Gyr]	Timescale [Gyr]	Age QS Enter [Gyr]	z QS Enter
0.50 - 0.65	0.58	7.89	3.60	4.29	1.46
0.65 - 0.83	0.74	6.94	3.00	3.94	1.61
0.83 - 1.08	0.96	5.91	2.60	3.31	1.95
1.08 - 1.40	1.24	4.91	2.20	2.71	2.38
1.40 - 1.88	1.64	3.88	1.60	2.28	2.80
1.88 - 2.64	2.26	2.85	1.40	1.45	4.14

Before exploring other hypotheses, we evaluated how "randomness" influenced our results by conducting 100 random runs by considering a different match of galaxies for each of the COSMOS ones. Like before, we found that the distributions varied very little between runs. The maximum STD of `t_quench` and, consequently, the quenching timescale, was 100 Myrs, with some cases exhibiting no variation (STD = 0). The shape of the distributions showed even less variation, with a maximum STD of 26 Myrs. This confirms, once again, that choosing to match each COSMOS galaxy with a random counterpart within our models has a negligible impact on `t_quench` and the quenching timescales of galaxies.

Table 5.6 presents the median values of `t_quench` and the quenching timescale computed from 100 random runs, divided into 1 Gyr bins for $0.50 < z < 2.64$. Both medians decrease with increasing redshift, but the trend is more linear compared to the results in Table 5.3. The overall medians of the main sample for $z = 2.64$ are consistent with those in Table 5.3, with `t_quench` at 3.0 Gyrs and the quenching timescale at 2.8 Gyrs. This agreement is expected since the less populated high-redshift bins while having lower values for `t_quench` and quenching timescales, have little influence on the overall

Table 5.6: Median values of `t_quench` and the quenching timescale of 100 random runs divided into 1 Gyr bins between $0.50 < z < 2.64$.

z-Bin	Median t_quench [Myr]	Median Timescale [Myr]
0.50 - 0.65	4400	3600
0.65 - 0.83	4000	3200
0.83 - 1.08	3400	2600
1.08 - 1.40	2800	2200
1.40 - 1.88	2300	1600
1.88 - 2.64	1800	1400
0.50 - 2.64	3000	2800

medians.

Table 5.7 displays the median percentage of PSB galaxies from 100 random runs within each Gyr bin and across the main sample for $0.50 < z < 2.64$. The PSB fraction increases more gradually when divided into 1 Gyr bins, starting at 0% and peaking at a median of 13.63% in the highest redshift bin. The STD of the PSB fraction also increases but remains relatively small, with a maximum variation of 1.01%. This indicates that the number of PSB galaxies changes less significantly relative to the total number of galaxies in each bin compared to the variations observed in the 0.5 redshift bins. Once again, we conclude that SFH alone can predict 2.17% of PSB galaxies.

Having confirmed that ”randomness” does not substantially affect the results for `t_quench`, the quenching timescale, or the fraction of PSB galaxies, we can proceed with further analysis.

Table 5.7: Median and STD values of the percentage of PSB galaxies of 100 random runs divided into 1 Gyr bins between $0.50 < z < 2.64$.

z-Bin	Median PSB %	STD PSB %
0.50 - 0.65	0.0	0.0
0.65 - 0.83	0.23	0.10
0.83 - 1.08	0.36	0.11
1.08 - 1.40	1.62	0.29
1.40 - 1.88	4.77	0.47
1.88 - 2.64	13.63	1.01
0.50 - 2.64	2.17	0.13

5.3.3 Fast and Slow Quenching

Our results and analyses in Subsections 5.3.1 and 5.3.2 demonstrated that not all quiescent galaxies undergo a PSB phase; in fact, the majority of galaxies in the main sample exhibit a secular quenching process. This suggests the existence of two distinct quenching timescales: a fast quenching timescale and a slow, secular one. Moreover, we showed that fast quenching is predominantly associated with high redshifts, while slow quenching characterizes low redshifts.

Building on the analysis by Belli et al. [2019], we illustrate these two quenching pathways on the UVJ diagram in Figure 5.8. Both models use the same parameters — `stellar.metallicity` = 0.02,

`attenuation.E_BVs.stellar.young` = 0.2, `attenuation.ebvs_old_factor` = 0.5 — and cover the same area in the color-color diagram occupied by the observations. In these examples age_main was kept as a free parameter. The fast quenching track (blue) has a `tau_main` of 200 Myrs, while the slow quenching track (red) has a `tau_main` of 2000 Myrs. The age at which these models enter the passive region — `t_quench` — is indicated and highlighted with a circle: 1.2 Gyr ($z = 4.84$) for fast quenching and 7.2 Gyr ($z = 0.69$) for slow quenching. As expected, the blue track shows rapid changes in UVJ colors just within 200 Myrs, while the red track exhibits much slower color evolution.

As Belli et al. [2019] noted, "the exact position of the crossing point" into the passive region depends on the quenching timescale. Younger galaxies, including PSB systems, appear to cross this "barrier" at the horizontal line $U - V = 1.3$, while older galaxies with more gradual, secular quenching mechanisms tend to enter along the diagonal edge of the passive region.

These results emphasize that the preferred quenching pathway — fast or slow — shifts with redshift. Contrary to what Figure 5.8 might suggest, it is important to note that while a low `tau_main` is often associated with fast quenching, it does not guarantee it. The models used here simply meet the conditions necessary for fast quenching to occur.

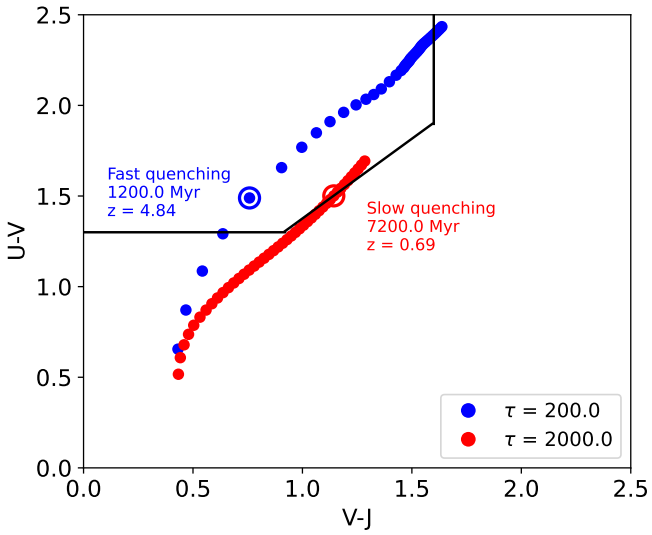

Figure 5.8: UVJ diagram showing fast- and slow-quenching paths of two models with `tau_main` of 200.0 (blue) and 2000.0 (red) Myrs, respectively. The age a model enters the passive region and its redshift is also shown and highlighted with a circle. Both models have a stellar metallicity of 0.02, $E(B - V)$ for the young population of 0.2 and a factor for the old population of 0.5.

Comparing Figures 5.8 and 5.7 with Tables 5.5 and 5.7, we observe an intriguing pattern: galaxies entering the passive region after the peak of cosmic star formation ($z < 2$; see Figure 1.6) exhibit timescales on the order of ∼3 Gyr, while those entering before the peak ($z > 2$) show timescales closer to ∼2 Gyr. These timescales remain consistent within the standard deviation obtained from 100 random runs. Galaxies transitioning below $z = 2$ predominantly exhibit secular quenching, as supported by the low fraction of "observed" PSB galaxies. Conversely, galaxies transitioning above $z = 2$ experience a more rapid quenching process, supported by a higher fraction of "observed" PSB systems.

We propose that the speed at which star-forming galaxies transition to quiescence depends on their position relative to the peak of the cosmic star formation history as presented by Madau and Dickinson [2014] (Figure 1.6). After the peak of star formation, quenching mechanisms tend to be more gradual, leading to slower timescales and a lower fraction of PSB galaxies. In contrast, before this peak, quenching

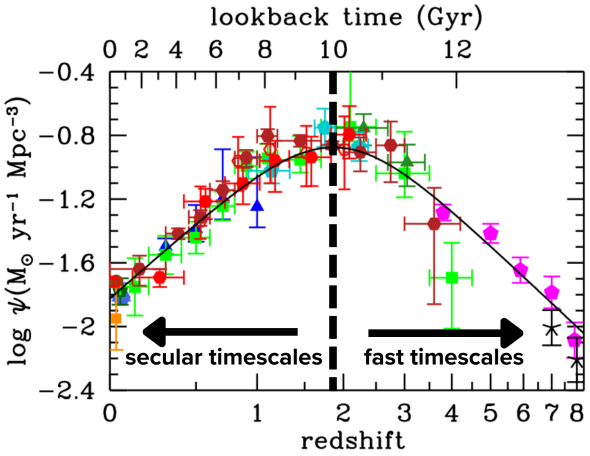

Figure 5.9: The history of cosmic star formation from FUV+IR rest-frame measurements as a function of redshift and lookback time, and its best-fitting function. The black arrows visually represent the difference in speed of the quenching process before and after the peak, which is presented by the dashed black line. Image adapted from Madau and Dickinson [2014].

mechanisms are more rapid, resulting in shorter timescales and a higher fraction of PSB galaxies. Figure 5.9 offers a physical representation of this phenomenon on the cosmic SFH plot by Madau and Dickinson [2014].

Determining the exact physical processes driving this behavior —whether SFH, AGN feedback, mergers, SN explosions, downsizing, or other mechanisms — is beyond the scope of this work. However, it is crucial to acknowledge the interplay of these processes in shaping galaxy evolution. The actual SFHs of galaxies are highly stochastic, influenced by environmental factors, internal feedback mechanisms, and interactions with nearby structures, making it challenging to replicate real galaxy evolution using simplified or idealized models.

If our synthetic models incorporated more complex and irregular SFHs, characterized by episodic bursts of star formation interspersed with quiescent phases, we might observe temporary cases of PSB galaxies. Additionally, the fraction of PSB galaxies could decrease if these bursts occur at very short intervals, allowing galaxies to quickly replenish their gas and resume star formation without a quiescent phase.

Furthermore, including other quenching mechanisms —such as AGN feedback, which can expel or heat gas, preventing further star formation, or galaxy mergers, which can trigger starburst activity followed by rapid quenching— would likely add new layers of complexity. Supernova explosions, particularly in starbursting galaxies, could also play a dual role by both triggering additional star formation through shockwave compression of surrounding gas and stopping it by expelling material from the galaxy. These processes, acting in together or independently, could significantly alter the timescale distributions and PSB fractions observed in our analysis.

Lastly, while our current models provide valuable results, they represent a simplified view of galaxy evolution. Expanding these models to include more sophisticated and dynamic SFHs, as well incorporating high resolution spectroscopic data or study these results with other simulators, could offer a better understanding of the processes shaping PSB systems and their prevalence across cosmic time.

Chapter 6

Conclusion

Throughout this study, we have examined in detail the various evolutionary phases of galaxies — active star-forming, quiescent, and green valley— with a particular focus on post-starburst galaxies. These systems, which have experienced a recent burst of star formation followed by a rapid quenching on the timescale of tens of Myrs, hold significant importance in understanding the cosmic star-formation history. As shown by Madau and Dickinson [2014], the cosmic star-formation rate density of the universe increased during early times, reaching a peak around $z \sim 2$, before entering a prolonged decline. The increasing fraction of PSB galaxies within the red sequence as a function of redshift may be a crucial clue to understanding what mechanisms triggered this change in the star-forming activity universe.

We based our work on the latest multi-wavelength catalog from the COSMOS survey, COSMOS2020 (Weaver et al. [2022b]), which spans an area of approximately 2 square degrees and is centered at (J2000) RA +150.11916667 (10:00:28.600) and DEC +2.20583333 (+02:12:21.00). In Chapter 2, we carefully cleaned this catalog, removing outliers and applying χ^2 analyses to ensure the reliability of our sample. This process resulted in a robust dataset comprising 248,307 sources within the redshift range $0.5 < z < 3.5$. The sources were selected based on criteria, such as an H-band magnitude limit of 27, a SNR greater than 3 giving a mass completeness above 75%.

We also analyzed some of its properties in Chapter 2 where important parameters were the median photometric redshift of 1.27, the median raw χ^2_{red} of 0.84, the median stellar mass of $\log(\mathrm{M}_*/[\mathrm{M}_\odot]) = 9.60$ and the median sSFR of $\log(\mathrm{sSFR}/[\mathrm{yr}^{-1}]) = -9.12$.

In Chapter 3, we used UVJ color-color diagrams to perform a detailed analysis of our sample, dividing it into six redshift bins ranging from $0.5 < z < 3.5$ with a step of 0.5. This approach allowed us to explore the distribution of galaxy populations across redshift. We found that, at high redshifts, the sample is limited by the lack of sources and the presence of large photometric errors, but as redshift decreases, the number of sources increases and the errors decrease.

Based on the classification criteria established by Williams et al. [2009], we defined three distinct regions in the UVJ diagrams:

- The QS region for red galaxies that have ceased star formation.
- The SF region for galaxies with ongoing star formation.
- An ambiguous region, with a thickness defined by the photometric color errors in each redshift bin. This region contains a mix of quiescent, star-forming, and galaxies in the phase of transition.

Our findings revealed that the sample is predominantly composed of SFG, which constitute 91.67% of the population, with 4.72% classified as QSG and 3.61% as AMG. The computed number density of galaxies was consistent with results from Weaver et al. [2022a].

Further analysis of the UVJ diagrams in Section 3.1.1 provided additional insights into the properties of these galaxies. Massive galaxies are primarily located in the redder regions of $V - J$, indicative of dusty starbursts (confirmed by the extinction in the V-band and LIR plots) or genuine passive galaxies. Younger systems, characterized by lower stellar masses, populate the blue regions of the diagram. The sSFR plots clearly illustrated the bimodal distribution, with QS galaxies showing low sSFR and SF galaxies exhibiting high sSFR. Moreover, the sSFR increases with redshift, reflecting the more vigorous star formation in earlier cosmic epochs.

Since redshift is not a linear measure of time due to the expansion of the universe, we repeated the analysis in Section 3.2 by dividing the sample into bins of 1 Gyr intervals from $0.5 < z < 2.64$. This complementary approach revealed a gradual increase in the fraction of passive galaxies within the red cloud over time. The observed decline in sSFR as we approach the present epoch was smoother and less pronounced compared to the redshift-bin-based analysis, offering a more nuanced view of the evolutionary trends.

We also explored other time intervals —1.5, 0.5, 0.4, 0.3, 0.2, and 0.1 Gyrs —to investigate the behavior of the STD of the number of galaxies in each bin across the three regions (SF, QS, and ambiguous). Our analysis showed that the 1.0 Gyr bin had the minimum STD, while the 0.1 Gyr bin had the maximum STD. However, this alone was insufficient to determine the typical timescale for galaxy transitions or to gain deeper insights into PSB systems.

In Chapter 4 we used simulations with `CIGALE` to build a synthetic sample designed to mimic the observed COSMOS data. The parameters used for these simulations are stated in Section 4.1, leading to a sample of 332,640 sources. In Section 4.2, we examined how `CIGALE` calculates the photometry, and in Section 4.3, we analyzed the synthetic sample, and concluded that our simulations successfully covered the parameter space of the COSMOS sample.

Using UVJ diagrams based on the criteria from Williams et al. [2009], we found that the star formation activity peak plays a significant role in galaxy classification. When the peak occurs at earlier times, approximately 40% of galaxies occupy the passive region. Conversely, when the peak occurs at later times, approximately 80% of galaxies reside in the star-forming region. Additionally, galaxies at earlier epochs exhibit higher SFR compared to those at later times, aligning with the expected evolutionary trends.

We noticed some sources in the passive region with higher stellar mass and lower H magnitude and SFR, somewhat resembling the dust diagonal line of COSMOS. However, while this feature in COSMOS is linked to dust extinction, in the synthetic sample, it stems from stellar metallicity effects. A closer investigation revealed that only a small fraction of passive galaxies in the synthetic sample had high metallicities of 0.05 ($\sim 2\%$) and 0.02 ($\sim 17\%$). This behavior suggested that metallicity is not a linear trend but rather influenced by degeneracies in the stellar population synthesis models. As metallicity increases, it introduces a curving effect that eventually plateaus, likely caused by the similarity of SEDs among these sources.

In Chapter 5, Section 5.1, we focused on obtaining a representative sample of COSMOS passive galaxies, defined as the densest part of the passive region in the UVJ diagram. This subset included 12,084 COSMOS sources, representing approximately 74% of the passive galaxies and about 5% of the total COSMOS sample, with a median age of 5.82 Gyrs. Using this region, we selected corresponding sources from our `CIGALE` synthetic sample based on matching ages. While multiple synthetic sources had the same age but derived from different parameter combinations, we randomly selected one per match, yielding a synthetic "main sample" of 12,084 sources that mirrored the COSMOS age distribution. In Section 5.2, we analyzed its properties, concluding that these galaxies had a median star formation peak

of 1.2 Gyrs, with low metallicity and low color excess for the young stellar population.

In Section 5.3, we investigated the time at which galaxies in the main sample entered the passive region and their corresponding quenching timescales, finding medians of 3.0 Gyrs and 2.8 Gyrs, respectively.

Similarly to before, we divided the main sample into 0.5 redshift bins and into 1 Gyr time bins. Based on previous studies, we classified PSB as galaxies that had a timescale lower than 0.7 Gyr. Our results indicated that while the absolute number of passive galaxies decreases with redshift, the percentage of PSB systems increases, reaching $\sim 31\%$ at $z \sim 2.5$ and $\sim 2\%$ at $z \sim 1.0$. These results align well with those of Belli et al. [2019]. Moreover, we observed that the median and standard deviation of quenching timescales decrease with redshift, indicating that galaxies quench more rapidly at higher redshifts —a trend consistent with the increased fraction of PSB galaxies. The median stellar mass of these galaxies increases from $\log(\mathrm{M}_*/[\mathrm{M}_\odot]) = 8.83$ to $\log(\mathrm{M}_*/[\mathrm{M}_\odot]) = 8.85$.

We concluded that SFH alone — without galaxy mergers, AGNs, or other mechanisms — can predict a small fraction of PSB galaxies, 2.82% of the main sample, i.e. galaxies with a quenching timescale lower than 0.7 Gyr. Lastly, we also noticed that the speed of transition from star-forming to passive galaxies depends on redshift: a fast quenching at higher redshifts and a slow quenching at lower redshifts. After the peak of star formation and quiescence, quenching mechanisms tend to become more secular, leading to slower quenching timescales and a lower fraction of PSB galaxies. Before the peak, quenching mechanisms are dominated by faster processes, resulting in shorter timescales and a higher fraction of PSB systems. These findings are consistent with previous studies, e.g, Belli et al. [2019], Wild et al. [2009], Wild et al. [2016], Rowlands et al. [2018], Forrest et al. [2018].

Overall, we have successfully achieved the primary objectives of our study:

- Exploring the importance of PSB galaxies in the evolutionary history of the universe.
- Investigating PSB patterns across different cosmic times and ages.
- Quantifying the fraction of PSB systems and their redshift-dependent trends.

Our results provide valuable insights into the role of PSB galaxies as key markers of rapid quenching processes and their implications for the cosmic star formation history. Future work could expand on this analysis by incorporating higher-resolution spectroscopy, more sophisticated and dynamic SFHs, testing with other simulators, and exploring additional mechanisms driving the transitions from star-forming to quiescent galaxies, which we did not take into account in this work. These aspects could provide a higher understanding of the processes that shape PSB systems including their fast quenching timescale and their prevalence across cosmic time.

My personal final conclusion is that observing the vast cosmos is indeed a mesmerizing experience.

References

Almeida, A., Anderson, S. F., Argudo-Fernández, M., Badenes, C., Barger, K., Barrera-Ballesteros, J. K., Bender, C. F., Benitez, E., Besser, F., Bird, J. C., et al. (2023). The eighteenth data release of the sloan digital sky surveys: Targeting and first spectra from sdss-v. *The Astrophysical Journal Supplement Series*, 267(2):44. 13

Arnouts, S., Moscardini, L., Vanzella, E., Colombi, S., Cristiani, S., Fontana, A., Giallongo, E., Matarrese, S., and Saracco, P. (2002). Measuring the redshift evolution of clustering: the hubble deep field south. *Monthly Notices of the Royal Astronomical Society*, 329(2):355–366. 15

Bambi, C. (2019). Astrophysical black holes: a review. *arXiv preprint arXiv:1906.03871*. 2

Belli, S., Newman, A. B., and Ellis, R. S. (2019). Mosfire spectroscopy of quiescent galaxies at 1.5< z< 2.5. ii. star formation histories and galaxy quenching. *The Astrophysical Journal*, 874(1):17. VII, 10, 58, 59, 61, 64, 65, 69

Boquien, M., Burgarella, D., Roehlly, Y., Buat, V., Ciesla, L., Corre, D., Inoue, A., and Salas, H. (2019). Cigale: a python code investigating galaxy emission. *Astronomy & Astrophysics*, 622:A103. VI, XIV, 11, 45, 46, 47, 48

Brammer, G. B., van Dokkum, P. G., and Coppi, P. (2008). Eazy: a fast, public photometric redshift code. *The Astrophysical Journal*, 686(2):1503. 15

Bruzual, G. and Charlot, S. (2003). Stellar population synthesis at the resolution of 2003. *Monthly Notices of the Royal Astronomical Society*, 344(4):1000–1028. 47

Buat, V., Boissier, S., Burgarella, D., Takeuchi, T., Le Floc'h, E., Marcillac, D., Huang, J., Nagashima, M., and Enoki, M. (2008). Star formation history of galaxies from z= 0 to z= 0.7-a backward approach to the evolution of star-forming galaxies. *Astronomy & Astrophysics*, 483(1):107–119. XIV, 47

Burgarella, D., Buat, V., and Iglesias-Paramo, J. (2005). Star formation and dust attenuation properties in galaxies from a statistical ultraviolet-to-far-infrared analysis. *Monthly Notices of the Royal Astronomical Society*, 360(4):1413–1425. VI, 11, 45

Calzetti, D., Armus, L., Bohlin, R. C., Kinney, A. L., Koornneef, J., and Storchi-Bergmann, T. (2000). The dust content and opacity of actively star-forming galaxies. *The Astrophysical Journal*, 533(2):682. 47

Chambers, K. C., Magnier, E., Metcalfe, N., Flewelling, H., Huber, M., Waters, C., Denneau, L., Draper, P., Farrow, D., Finkbeiner, D., et al. (2016). The pan-starrs1 surveys. *arXiv preprint arXiv:1612.05560*. 13

Colvin, A. Z. (2018). Local group. CC BY-SA 4.0, via Wikimedia Commons. XI, 2

Cosmogoblin (2022). Hubble tuning fork diagram. CC0, via Wikimedia Commons. XI, 4

Dai, Y. S., Malkan, M. M., Teplitz, H. I., Scarlata, C., Alavi, A., Atek, H., Bagley, M., Baronchelli, I., Battisti, A., Bunker, A. J., et al. (2021). Spectroscopically identified emission line galaxy pairs in the wisp survey. *The Astrophysical Journal*, 923(2):156. 17, 52

Dale, D. A., Helou, G., Magdis, G. E., Armus, L., Díaz-Santos, T., and Shi, Y. (2014). A two-parameter model for the infrared/submillimeter/radio spectral energy distributions of galaxies and active galactic nuclei. *The Astrophysical Journal*, 784(1):83. 48

Forrest, B., Tran, K.-V. H., Broussard, A., Cohn, J. H., Kennicutt Jr, R. C., Papovich, C., Allen, R., Cowley, M., Glazebrook, K., Kacprzak, G. G., et al. (2018). Zfourge: Using composite spectral energy distributions to characterize galaxy populations at 1< z< 4□. *The Astrophysical Journal*, 863(2):131. 10, 61, 69

Fraknoi, A., Morrison, D., and Wolff, S. C. (2016). *Astronomy (OpenStax)*. OpenStax. 2, 3, 4, 5, 7, 15, 20

Froome, K., Essen, L., and Rhodes, R. A. (1971). The velocity of light and radio waves. *Physics Today*, 24(5):49–49. 1

Gavazzi, G., Fumagalli, M., Cucciati, O., and Boselli, A. (2010). A snapshot on galaxy evolution occurring in the great wall: the role of nurture at z= 0. *Astronomy & Astrophysics*, 517:A73. XI, 8

Goto, T., Nichol, R. C., Okamura, S., Sekiguchi, M., Miller, C. J., Bernardi, M., Hopkins, A., Tremonti, C., Connolly, A., Castander, F. J., et al. (2003). Hδ-strong galaxies in the sloan digital sky survey: I. the catalog. *Publications of the Astronomical Society of Japan*, 55(4):771–787. 10

Hubble, E. (1926). No. 324. extra-galactic nebulae. *Contributions from the Mount Wilson Observatory/Carnegie Institution of Washington, vol. 324, pp. 1-49*, 324:1–49. XI, 4, 5

Koekemoer, A. M., Aussel, H., Calzetti, D., Capak, P., Giavalisco, M., Kneib, J.-P., Leauthaud, A., Le Fevre, O., McCracken, H., Massey, R., et al. (2007). The cosmos survey: Hubble space telescope advanced camera for surveys observations and data processing. *The Astrophysical Journal Supplement Series*, 172(1):196. 14

Kormendy, J. and Ho, L. C. (2013). Coevolution (or not) of supermassive black holes and host galaxies. *Annual Review of Astronomy and Astrophysics*, 51(1):511–653. 3

Kron, R. G. (1980). Photometry of a complete sample of faint galaxies. *Astrophysical Journal Supplement Series, vol. 43, June 1980, p. 305-325. Research supported by the University of California*, 43:305–325. 16

Lampton, M., Margon, B., and Bowyer, S. (1976). Parameter estimation in x-ray astronomy. *Astrophysical Journal, vol. 208, Aug. 15, 1976, pt. 1, p. 177-190.*, 208:177–190. XII, 17, 18

Leja, J., Tacchella, S., and Conroy, C. (2019). Beyond uvj: More efficient selection of quiescent galaxies with ultraviolet/mid-infrared fluxes. *The Astrophysical Journal Letters*, 880(1):L9. XII, 24

Madau, P. and Dickinson, M. (2014). Cosmic star-formation history. *Annual Review of Astronomy and Astrophysics*, 52(1):415–486. VI, XI, XVI, 9, 25, 26, 35, 63, 65, 66, 67

Maltby, D. T., Almaini, O., Wild, V., Hatch, N. A., Hartley, W. G., Simpson, C., McLure, R. J., Dunlop, J., Rowlands, K., and Cirasuolo, M. (2016). The identification of post-starburst galaxies at z 1 using multiwavelength photometry: a spectroscopic verification. *Monthly Notices of the Royal Astronomical Society: Letters*, 459(1):L114–L118. 10

Maltby, D. T., Almaini, O., Wild, V., Hatch, N. A., Hartley, W. G., Simpson, C., Rowlands, K., and Socolovsky, M. (2018). The structure of post-starburst galaxies at 0.5< z< 2: evidence for two distinct quenching routes at different epochs. *Monthly Notices of the Royal Astronomical Society*, 480(1):381–401. III, VI, 10, 11

Maoz, D. (2016). *Astrophysics in a Nutshell*, volume 16. Princeton university press. 3

McCracken, H., Milvang-Jensen, B., Dunlop, J., Franx, M., Fynbo, J., Le Fèvre, O., Holt, J., Caputi, K., Goranova, Y., Buitrago, F., et al. (2012). Ultravista: a new ultra-deep near-infrared survey in cosmos. *Astronomy & Astrophysics*, 544:A156. 61

Mo, H., Van den Bosch, F., and White, S. (2010). *Galaxy formation and evolution*. Cambridge University Press. XI, 1, 3, 4, 5, 6, 7, 9

Moutard, T., Sawicki, M., Arnouts, S., Golob, A., Malavasi, N., Adami, C., Coupon, J., and Ilbert, O. (2018). On the fast quenching of young low-mass galaxies up to z 0.6: new spotlight on the lead role of environment. *Monthly Notices of the Royal Astronomical Society*, 479(2):2147–2160. 10

Murdin, P. (2001). *Encyclopedia of astronomy & astrophysics*. CRC Press. 2, 5, 6, 7

Noll, S., Burgarella, D., Giovannoli, E., Buat, V., Marcillac, D., and Munoz-Mateos, J. (2009). Analysis of galaxy spectral energy distributions from far-uv to far-ir with cigale: studying a sings test sample. *Astronomy & Astrophysics*, 507(3):1793–1813. VI, 11, 45

Oke, J. and Gunn, J. (1983). Secondary standard stars for absolute spectrophotometry. *Astrophysical Journal, Part 1, vol. 266, Mar. 15, 1983, p. 713-717.*, 266:713–717. 11, 18

Poggianti, B. M., Aragón-Salamanca, A., Zaritsky, D., De Lucia, G., Milvang-Jensen, B., Desai, V., Jablonka, P., Halliday, C., Rudnick, G., Varela, J., et al. (2009). The environments of starburst and post-starburst galaxies at z= 0.4–0.8. *The Astrophysical Journal*, 693(1):112. VII, 10, 58

Pozzetti, L., Bolzonella, M., Zucca, E., Zamorani, G., Lilly, S., Renzini, A., Moresco, M., Mignoli, M., Cassata, P., Tasca, L., et al. (2010). zcosmos–10k-bright spectroscopic sample-the bimodality in the galaxy stellar mass function: exploring its evolution with redshift. *Astronomy & Astrophysics*, 523:A13. 16

Prusti, T., De Bruijne, J., Brown, A. G., Vallenari, A., Babusiaux, C., Bailer-Jones, C., Bastian, U., Biermann, M., Evans, D. W., Eyer, L., et al. (2016). The gaia mission. *Astronomy & astrophysics*, 595:A1. 13

Redd, N. T. (2018). Astronomers track dwarf galaxies to better understand the milky way's make-up and evolution. *Proceedings of the National Academy of Sciences*, 115(51):12836–12838. 1

Renzini, A. and Peng, Y.-j. (2015). An objective definition for the main sequence of star-forming galaxies. *The Astrophysical Journal Letters*, 801(2):L29. XI, 8

Rodrigo, C. and Solano, E. (2020). The svo filter profile service. In *XIV. 0 Scientific Meeting (virtual) of the Spanish Astronomical Society*, page 182. 46, 48, 50

Rodrigo, C., Solano, E., Bayo, A., and Rodrigo, C. (2012). Svo filter profile service version 1.0. *IVOA Working Draft*, 15. 46, 48, 50

Rowlands, K., Wild, V., Bourne, N., Bremer, M., Brough, S., Driver, S. P., Hopkins, A. M., Owers, M., Phillipps, S., Pimbblet, K., et al. (2018). Galaxy and mass assembly (gama): The mechanisms for quiescent galaxy formation at z< 1. *Monthly Notices of the Royal Astronomical Society*, 473(1):1168–1185. 10, 61, 69

Salim, S. (2015). Green valley galaxies. *arXiv preprint arXiv:1501.01963*. 9

Salpeter, E. E. (1955). The luminosity function and stellar evolution. *Astrophysical Journal, vol. 121, p. 161*, 121:161. 47

Scoville, N., Abraham, R., Aussel, H., Barnes, J., Benson, A., Blain, A., Calzetti, D., Comastri, A., Capak, P., Carilli, C., et al. (2007a). Cosmos: Hubble space telescope observations. *The Astrophysical Journal Supplement Series*, 172(1):38. 14

Scoville, N., Aussel, H., Brusa, M., Capak, P., Carollo, C. M., Elvis, M., Giavalisco, M., Guzzo, L., Hasinger, G., Impey, C., et al. (2007b). The cosmic evolution survey (cosmos): overview. *The Astrophysical Journal Supplement Series*, 172(1):1. 14

Tully, R. B., Courtois, H., Hoffman, Y., and Pomarède, D. (2014). The laniakea supercluster of galaxies. *Nature*, 513(7516):71–73. 1

Weaver, J., Davidzon, I., Toft, S., Ilbert, O., McCracken, H., Gould, K., Jespersen, C., Steinhardt, C., Lagos, C., Capak, P., et al. (2022a). Cosmos2020: The galaxy stellar mass function: the assembly and star formation cessation of galaxies at 0.2<z<7.5. *arXiv preprint arXiv:2212.02512*. 29, 67

Weaver, J. R., Kauffmann, O., Ilbert, O., McCracken, H. J., Moneti, A., Toft, S., Brammer, G., Shuntov, M., Davidzon, I., Hsieh, B.-C., et al. (2022b). Cosmos2020: a panchromatic view of the universe to z 10 from two complementary catalogs. *The Astrophysical Journal Supplement Series*, 258(1):11. VI, XI, XII, 11, 14, 15, 16, 17, 23, 46, 67

Whitaker, K. E., Kriek, M., van Dokkum, P. G., Bezanson, R., Brammer, G., Franx, M., and Labbé, I. (2012). A large population of massive compact post-starburst galaxies at z> 1: Implications for the size evolution and quenching mechanism of quiescent galaxies. *The Astrophysical Journal*, 745(2):179. 10, 11

Wild, V., Almaini, O., Cirasuolo, M., Dunlop, J., McLure, R., Bowler, R., Ferreira, J., Bradshaw, E., Chuter, R., and Hartley, W. (2014). A new method for classifying galaxy seds from multiwavelength photometry. *Monthly Notices of the Royal Astronomical Society*, 440(2):1880–1898. 10

Wild, V., Almaini, O., Dunlop, J., Simpson, C., Rowlands, K., Bowler, R., Maltby, D., and McLure, R. (2016). The evolution of post-starburst galaxies from z= 2 to 0.5. *Monthly Notices of the Royal Astronomical Society*, 463(1):832–844. 10, 61, 69

Wild, V., Asari, N. V., Rowlands, K., Ellison, S. L., Leung, H.-H., and Tremonti, C. (2024). The infrared luminosity of retired and post-starburst galaxies: A cautionary tale for star formation rate measurements. *arXiv preprint arXiv:2409.08672*. 10

Wild, V., Kauffmann, G., Heckman, T., Charlot, S., Lemson, G., Brinchmann, J., Reichard, T., and Pasquali, A. (2007). Bursty stellar populations and obscured active galactic nuclei in galaxy bulges. *Monthly Notices of the Royal Astronomical Society*, 381(2):543–572. 10

Wild, V., Taj Aldeen, L., Carnall, A., Maltby, D., Almaini, O., Werle, A., Wilkinson, A., Rowlands, K., Bolzonella, M., Castellano, M., et al. (2020). The star formation histories of z 1 post-starburst galaxies. *Monthly Notices of the Royal Astronomical Society*, 494(1):529–548. VII, 10, 58, 59

Wild, V., Walcher, C. J., Johansson, P. H., Tresse, L., Charlot, S., Pollo, A., Le Fèvre, O., and De Ravel, L. (2009). Post-starburst galaxies: more than just an interesting curiosity. *Monthly Notices of the Royal Astronomical Society*, 395(1):144–159. VII, 10, 58, 59, 69

Williams, R. J., Quadri, R. F., Franx, M., Van Dokkum, P., and Labbé, I. (2009). Detection of quiescent galaxies in a bicolor sequence from z= 0–2. *The Astrophysical Journal*, 691(2):1879. VI, XII, XIII, XIV, XV, 23, 25, 26, 30, 32, 33, 34, 35, 36, 37, 38, 39, 49, 51, 52, 53, 55, 67, 68

York, D. G., Adelman, J., Anderson Jr, J. E., Anderson, S. F., Annis, J., Bahcall, N. A., Bakken, J., Barkhouser, R., Bastian, S., Berman, E., et al. (2000). The sloan digital sky survey: Technical summary. *The Astronomical Journal*, 120(3):1579. 13